Università degli Studi di Napoli “Federico II”

Scuola Politecnica e delle Scienze di Base

Ph. D. School in Chemical Sciences

Modeling artificial leaf

Ph.D. Student:
Umberto Raucci

Supervisor:
Prof. Nadia Rega

2013-2016

Contents

Introduction

Rational exploitation of sunlight can improve the everyday quality of life. At first blush, this sentence looks like certain ecologist slogan but it is simply founded on the astounding effects induced by light on matter.

If you explain to a child the principles of the ground state chemistry and later the transformations occurring in some molecules upon light irradiation, most probably he will think that there is something magic in it. Indeed, when molecules absorb a photon reach an electronically excited state, characterized by a strongly perturbed electronic structure. The clear result, in many cases, is a reactive behavior that ground state chemistry cannot achieve: photoexcited molecules can turn itself into strong oxidizing or reducing species, and also their acidity can drastically change.

Taking advantage of these light induced transformations to storage sunlight energy into chemical bonds represents, undoubtedly, the last frontier to face the global energy problem. The main idea is the development of artificial photosynthetic systems in which the production of chemical fuels proceeds through water oxidation to oxygen and protons or carbon dioxide reduction to hydrogen or organic molecule (methane, methanol, formaldehyde, etc), respectively. [1–7]

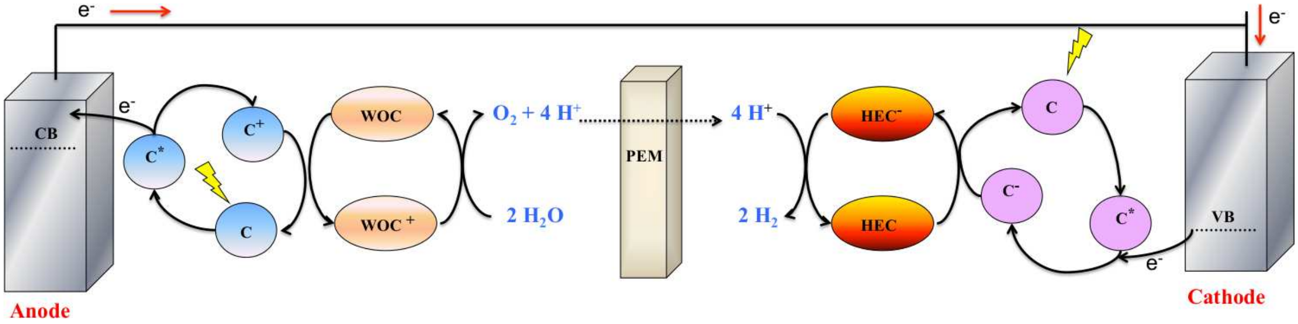

Fig. 1: Schematic representation of a dye-sensitized photoelectrochemical cell (DSPEC) performing the overall light induced water splitting.CB and VB represent the conduction and valence band of the semiconductor, respectively. Chromophore (C), water oxydation catalyst (WOC) and hydrogen evolving catalyst (HEC) are also represented.

Thus, simply starting from water, a very inexpensive and abundant material on the planet, and sunlight, a virtual inexhaustible energy source, the production of chemicals with a higher energetic content and all the properties of fuels could be amazingly achieved. A great potential is behind the artificial photosynthetic technology: the content of a small water pool (3 x 4 x 1 m, about 12000 l of water) would be enough to fulfil the yearly energy needs of a single person. [7] From the pioneering works of Honda and Fujishima on light-driven water splitting by direct TiO_2 excitation, [8] many steps were done for the improvement of photoelectrochemical cells (PECs). At the state of the art, last generation PEC are the so called dye-sensitized photoelectrochemical cells (DSPEC), functioning as an artificial leaf utilizing molecular assemblies that both absorb light and catalyze water oxidation at the photoanode and proton reduction at the cathode. [2,6] A schematic representation of a generic DSPEC is provided as Figure 1.

A chromophore directly anchored on the surface of a wide band gap semiconductor absorbs the light radiation leading to an electron transfer from its excited state to the conduction band of the semiconductor. The injected electrons are transferred into an external circuit to the cathode where the protons reduction is carried out, while the electronic hole on the chromophore activates the water oxidation catalyst (WOC). These steps are repeated four times to store the four oxidizing equivalents required to split two water molecules into oxygen. The development of such kind electrochemical devices is, of course, anything but simple since several entangled processes have to be finely combined and controlled (i.e light harvesting, electron transfer, water oxidation).

A good inspiration for the design of such devices is definitely provided by Nature that, through eons and eons of evolution, developed a miraculous charge transfer molecular machine called photosystem II (PSII) to convert sunlight into chemically accessible energy. [9] Although this system is an optimum starting point for the construction of artificial photosynthetic machines, at the state of the art the four electron water oxidation reaction and the combination with the excited state (ES) features of the dye represent the weak points toward the development of competitive cells. [7] The fine tuning of future DSPEC goes through the rational handling of the WOC and dye electronic structure. This cornerstone is laid on the most advanced developments of theoretical chemistry. Indeed, the theoretical-computational approach can offer many food for thought and numerous atomistic insights to optimize the performances and the reaction mechanisms of such molecular assays.

Unquestionably the theoretical simulation of the Charge Transfer (CT) reactivity for this kind of systems its far from straightforward due to the fine interplay of electronic, nuclear and solute solvent interactions. On the one hand the solution of the electronic problem is intrinsically delicate because the involved molecules are, in many cases, open shell systems with a great number of unpaired electrons or excited state with a strong charge transfer character. In spite of recent advances in electronic theory, the right representation of these CT species is still a challenge for methods rooted in Density Functional Theory (DFT) [10] and its Time Dependent version (TD-DFT). [11–14] On the other hand the nuclear motion along the reaction coordinate can be very complex involving many internal modes of the systems and most important it is followed by a significant electronic rearrangement. Moreover the solvent can drastically influence the electron/nuclear coupling. The proper representation of the solvent is, thus, mandatory in order to have a clear definition of the reaction space, including micro and bulk solvation effects. Ab initio molecular dynamics (AIMD) [15–17] represents a pivotal and essential tool to unveil complex reaction pathway in both the ground and excited states. However, especially for excited state reaction, prompted by the light irradiation, the reliability of TD-DFT based AIMD approaches needs to undergo an assessment step before being routinely employed as robust and efficient tools to describe photo triggered processes.

This scenario laid the foundations for this Ph.D. project, focalized on the set up of a computationally stable protocol to enable the description of light induced charge transfer (CT) reactivity on both static and dynamical grounds. Moreover the main purpose has been to provide new points of view and insights to support the future design strategies of molecular assemblies suitable for the application in DSPEC devices, by disentangling their complex electronic structures.

Keeping in mind a stairway of growing complexity (ideally shown in Figure 2), the project started with the study of the elementary steps of phototriggered charge transfer reactivity, namely photoinduced electron transfer (PET), excited state proton transfer (ESPT) and finally proton coupled electron transfer (PCET).

As starting point, the intramolecular PET in rhodamine dyes was investigated as non radiative decay pathway affecting their photophysic in solvent. [18] This CT mechanism was simulated as an internal conversion between two different excited states of bright and charge transfer character, triggered by a structural deformation arising from the subtle balance of coulombic and non-classical interactions between the principal molecular moieties. To assess and quantify the nature of the excited states involved in the process, the use of an electronic density based index, the so called D_{CT} index, [19] was employed as tool for the description of the charge transfer metrics.

As further step, excited state proton transfer reactions were taken into consideration investigating mechanism and driving forces by means of excited state AIMD simulation adopting different solvation models to represent the environmental effects. On the one hand we analysed the ESPT occurring between a coumarine and

Fig. 2: A stairway to heaven of charge transfer system.

an imidazole molecule in toluene solution adopting a fully implicit model for the solvation, i.e. the Polarizable Continuum Model. [20] On the other hand we studied the ESPT from a dipicolinium cyanine dye towards water solvent molecules, considering the solvent coordinate in an explicitly way through a discrete/continuum solvation model, enforcing non-periodic boundary conditions. These results suggest that the combination of AIMD simulation with time dependent density functional theory is a reliable and feasible tool to represent light induced processes.

On the same line, the effects of the surrounding medium on the energetics of a PCET reaction, involving well characterized oligo-peptide, [21, 22] were investigated providing an explanation for the experimental evidences about reactivity. By means of ab-initio molecular dynamics and a solute/solvent cluster approach we showed how the microsolvation structure of the involved species can affect the energy of the electronic states involved in the process, as well as the electronic coupling among them.

Tuned the method on the elementary step of CT reactivity, many efforts have been devoted to the theoretical characterization from a structural, energetic and reactive point of view of very promising recently synthetized molecules, suitable for the application in DSPEC devices. [23, 24] In summary, the whole excited state cascade of a molecular triad, [23] intriguing as artificial reaction center, has been completely simulated, integrating also its photophysical characterization (i.e. absorption and fluorescence features). Moreover we provide clear evidences on the formation of a crucial final charge separated state never achieved up to now from an experimental point of view, individuating also the promoting modes of the various charge transfer steps. Finally the characterization of the catalytic water splitting cycle of a new proposed water oxidation catalyst, [24] strongly mimic the native oxygen evolving complex of PSII, was taken under study. More closely we integrated the few experimental insights available about its reactivity, simulating the overall catalytic cycle and showing its great potentiality and efficiency in the oxygen-oxygen bond formation.

Each case of study is amply discussed in the following chapters, after a brief recall of the phototriggered Charge Transfer elementary steps and how they combine in the photosynthetic natural process. Final remarks and perspectives are given as conclusion. An overview of methods used and implemented during this work are provided as Appendix.

Chapter 1

Discovering the instruments of the photosynthetic orchestra: an overview of the light induced Charge Transfer elementary steps

Phototriggered charge transfer reactions occur with charge redistribution, upon light excitation, between an initially reactant state and a well defined product state. Electrons and protons are the principal actors involved, playing a full part in photoinduced electron transfer, excited state proton transfer and proton coupled electron transfer reactions. In this chapter the elementary steps of light induced charge transfer reactivity are briefly discussed focusing, also on the theoretical challenges for their description. How these elementary steps combine in photosynthesis is finally illustrated.

1.1 Photoinduced Electron Transfer: general insights

Photoinduced electron transfer can be regarded as an efficient process where absorbed light energy is transformed into chemical energy. The absorption event and the population of an excited state are followed by charge redistribution between a molecular portion acting as electron donor (D) and another one acting as electron acceptor (A). In the framework of frontier molecular orbital theory [25], PET can be, thus, simply schematized as the the result of the transition of a single electron from an initial molecular orbital (MO) (donor state) to the MO of the final state (acceptor state). More closely, after the excitation of the electron donor, an electron is transferred from its Highest Occupied Molecular Orbital(HOMO) to its Lowest Occupied Molecular Orbital(LUMO). Photoinduced electron transfer takes place involving the transfer of an electron from the LUMO of the donor to the LUMO of the acceptor group (see Figure 1.1.)

These reactions proceed in such a manner that the transferred electron remains in a bound state with respect to the particular molecule or molecular system. In other words, the electron is not activated above the ionization threshold and in this way is transferred to a different region of the molecular complex.

The key point for the theoretical simulation of PET reactions is the description of electronic states with a net charge transfer character. Post Hartree Fock methods would be the election technique in this sense, unfortunately they cannot be those

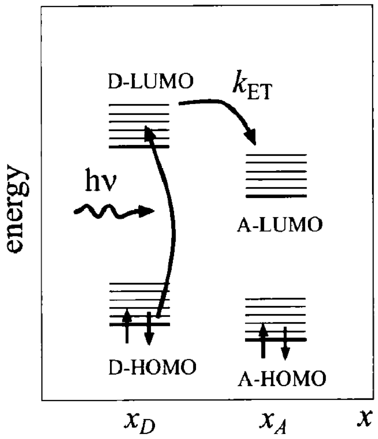

Fig. 1.1: Photoinduced ET reaction in a DA complex with spatial donor position X_D and acceptor position X_A (thick lines - electronic levels, thin lines - vibrational levels). The reactant state electron configuration is shown. The electron spin is represented by an upward or downward arrow, and the curved arrow indicates the pathway the transferred electron takes toward the product state.

of choice considering the large sized system under investigation and the need to include surrounding medium effects to reproduce the right behavior of charge transfer species. TD-DFT, on the other hand, scales favorably with the number of electrons, resulting very appealing for the study of such systems. Although TD-DFT is a formally exact method, one introduces errors by using approximate exchange correlation (xc) functionals. [14, 26] In general, valence excitations that do not involve substantial CT character are described reasonably well using conventional xc functionals. TD-DFT fails principally to yield reasonable excitation energies for CT states as well as to give the correct 1/R asymptotic behavior of CT excited states with respect to a distance coordinate R between the separated charges, when standard xc functionals are employed. [14] The first failure is due to the self-interaction error present in the orbital energies of the ground state DFT calculation, which leads to an underestimation of the HOMO-LUMO gap. The incorrect asymptotic behavior of the CT excited states is still due to a self-interaction problem, arising from the fact that the orbital energy of the electron accepting orbital contains the Coulomb repulsion between the accepting and the donating orbital, which is not present in the CT state but which is not correctly cancelled in the TD-DFT calculation unless exact exchange is present. [14] Of course Range Separated Hybrid functionals, providing the correct asymptotic behavior of the exchange potential, have a tendency to improve the CT state description. However an accurate calibration of the electronical potential is mandatory as starting point for the correct simulation of such kind of CT reactivity. This was an important aim of this thesis, representing the initial step of each investigated case of study.

1.2 Excited State Proton Transfer: inside the phenomenon

The classification of organic molecules according to their acidity is a fundamental topic of every introductive chemistry course. Nevertheless, it can be completely overturned at the excited electronic state. In few words, the irradiation of the sample produces the population of molecules in an excited state, characterized by an electronic distribution that changes the acidity of the protonated site, which in turn dissociates transferring a proton to a nearby solvent molecule or to a strong base present in solution. In general, photoacids are aromatic organic molecules that perform like weak acids in their ground electronic state and increase the acidity by many orders of magnitude in their first electronic state.

Excitation of a photoacid solution of pH lower than its ground state pK_a, generates a vibrationally relaxed, electronically excited ROH molecule, denoted by ROH^*, that initiates the photoprotolytic cycle reported in Figure 1.2.

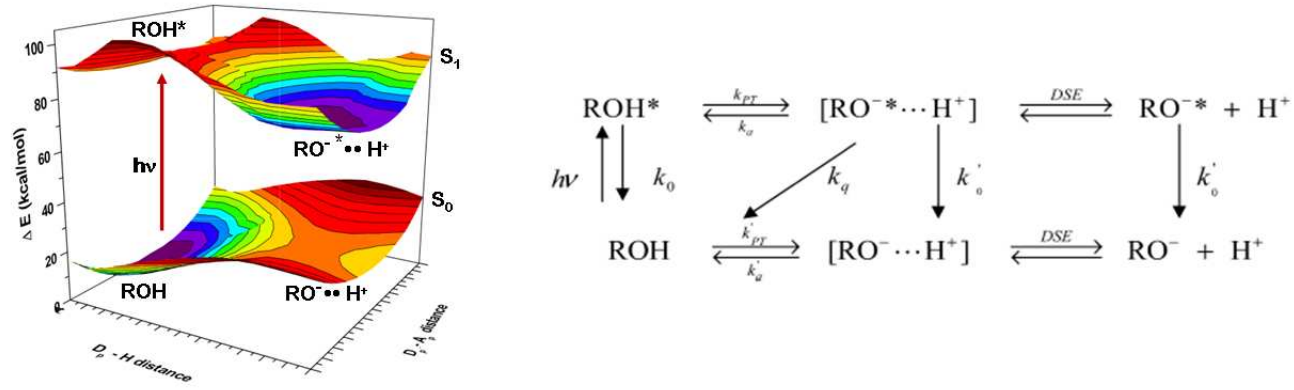

Fig. 1.2: The photoprotolytic cycle of a photoacid.

Proton dissociation, with an intrinsic rate constant k_{PT}, leads the formation of an ion-pair that subsequently forms an unpaired RO^{-*} and a solvated proton, which diffuse into the bulk of the solvent. These species may recombine to reform the excited acid, ROH^*, or back-protonation may proceed by an irreversible pathway, involving fluorescence quenching of the RO^{-*} by a proton, with a rate constant k_q, forming the ground state ROH.

The understanding of ESPT reactions requires the investigation of several elementary steps composing the overall process. The ultrafast electronic redistribution upon the photoexcitation, the nuclear relaxation, the hydrogen bonds rearrangement and the solvation dynamics, finely control the kinetics and thermodynamics of the ESPT event. [27] As matter of fact, the kinetics of the ESPT toward a solvent molecule covers a wide range of time scales, going from femto to nanoseconds. Beneath different kinetics there are, of course, different ESPT mechanisms.

A recent classification of Huppert and co-workers divides photoacid molecules into four regimes, according to their pK_a* values and the ESPT rate. [28] When going from regime I to regime IV the strength of the photoacid and the ESPT rate increase, while the pK_a* value diminishes. At the same time, the photoacid capability to transfer the proton to protic solvents other than water, such as methanol and ethanol, grows from regime I to IV. In the case of regimes I and II ($pK_a^* \sim 0$ and $-4 < pK_a^* < 0$, respectively) the ESPT reaction is relatively slow (k_{ESPT} in the order of 10^{10} s^{-1}). It is assumed that in this case the PT rate is controlled by covalent interactions within the proton-transferring complex. In the regime III ($-6 < pK_a^* < -4$), the ESPT rate is more rapid, and it is limited by the solvent dynamics responding to the solute excitation, mostly the solvent orientational motion. This regime is the so-called solvent control limit. [29] Finally, in the case of ultrafast ESPT (regime IV, $pK_a^* < -7$), it is hypothesized that only an inner coordinate of the proton-transferring complex limits the process, namely the distance between the acceptor and the donor atoms of the hydrogen bonded complex. [28] One of the aim of the present thesis is to check this hypothesis.

Theoretical investigations of these phenomena are really exciting and challenging.

The main challenge for theoretical approaches regards the study of excited state reaction pathways far from the vertical excitation in the Franck Condon region. As matter of fact the choice of an effective ESPT reaction coordinate is not a trivial problem since the electronic excitation and the subsequent relaxation on the ES Potential Energy Surface (PES) may induce significant changes in both the electronic and nuclear structure of the reactants. The ESPT reaction coordinate can be indeed very complex, involving many internal modes of the system under study, which can be also of collective nature. This problem is even more exasperated when the proton transfer is coupled to the solvation dynamics, as it happens for ultrafast ESPT, namely regime III and IV.

In these cases the solvent may be not fully equilibrated, and the transfer rate depends on the solvent motions. This, in turn, requests the explicit consideration of the solvent nuclear degrees of freedom, notably increasing the size of reaction phase space.

In this scenario the complete mechanics and kinetics characterization of ESPT reactions would greatly benefit from the use of computational methods well-established for the study in the ground state, such as the integration of the Intrinsic Reaction Coordinate (IRC) [30–34] and the ab-initio molecular dynamics (AIMD). [15–17]

The accuracy of ab initio molecular dynamics based on the calculation of energy and energy derivatives by TD-DFT [35,36] has been already demonstrated. [37,38] However, many standard functionals (like the global hybrid B3LYP [39]) fail to reproduce the relative spacing among the energies of excited states with different charge transfer character, possibly leading to unphysical crossings between different PESs during an AIMD simulation far from the Franck Condon region. The underestimation of PT barriers at the DFT level, well-known from studies of reactivity at the ground state, [40–43] can also affect the quality of the AIMD. Therefore, the reliability of TD-DFT based AIMD approaches (in conjunction with solvent models) needs to undergo an assessment step before these approaches can be routinely used as robust and efficient tools to describe ESPT reactions.

This thesis aims to satisfy this question characterizing the intrinsic and dynamical pathways of two pilot ESPT reactions by means of both fully implicit and discrete/continuum solvation models.

1.3 A further level of complication: proton coupled electron transfer

Finally, the coupling between electron and proton transfer reactions gives rise to the so called Proton Coupled Electron Transfer (PCET) processes which plays a vital role in many biological processes such as photosynthesis and enzymatic reactions, as well as in electrochemical devices.

In general the electron transfer (ET) may or may not stimulate the proton transfer (PT). Indeed, upon electron transfer, the proton may be thermodynamically and/or kinetically prompted to transfer because the electronic energy and solvation energetics that the proton experiences will be typically different after the ET reaction. That is, the potential energy surface governing the PT may become favourable for proton transfer after the electron transfer. Thermodynamically, the proton may exhibit a lower pK_a after ET. [44] This feature is analogous to excited state proton transfer reactions where, upon electronic excitation, a proton may become much more labile. Here, it is the electron transfer that may act like an electronic excitation in the sense of inducing a proton transfer reaction.

The transfer of an electron and proton may be sequential, where either the electron or the proton transfers first, or concerted, where the electron and proton transfer simultaneously.

This general definition of PCET includes hydrogen atom transfer (HAT), in which the electron and proton transfer simultaneously between the same donor and acceptor. Instead PCET is often reserved for reactions in which the electron and proton transfer between different donor and acceptors. [45, 46]

However these distinctions are not rigorously defined because the electron and proton behave quantum mechanically and hence are not localized to a single point at any given time. Thus, to maintain generality, all of these types of mechanisms can be viewed within the unified framework of PCET reactions.

Understanding such type of processes, in which both electrons and protons are transferred, is a very challenging task, especially in the cases where the electron/proton donor and acceptor are bound through molecular bridges. Indeed, in these cases, extremely important are both the properties of the donor and acceptor, (such as redox potential E and pK_a [47]) then the conformation of the bridge binding them. [48] A fine interplay of electronic, nuclear and solute solvent interactions controls the kinetics and thermodynamics features of the PCET event.

The rate constants can be recovered by Marcus like models, in which free energy surfaces of proton/electron donors and acceptors depend on reorganization energies with respect the two processes. Different Marcus-like expressions for the ET rate have been presented, according to the relative timescales and coupling of the transferring electron and proton, solute and solvent, as well as the coupling among them. [49–51]

It's clear that the degree of adiabaticity between electronic and nuclear configurations is a key parameter involved in the process, strongly correlated to the physicochemical features of the reaction (donor and acceptor nature, spacing, molecular environment, etc.).

Moreover, local rearrangements of water molecules in the cybotactic region, can influence the reaction procedure by affecting the electronic coupling between the electronic states involved in the reaction.

Several examples of the water effects on the electron transfer have appeared in recent years in literature, [52] and the theoretical investigation presented in this thesis aims to provide significant insights into the surrounding medium effects on the energetics of the PCET reaction.

1.4 Photosystem II: a spectacular charge transfer molecular machine

All these elementary steps play a crucial role in the photosynthetic process. Literally, photosynthesis means 'synthesis with light' and it is a biological process whereby the Sun energy is captured and stored by a series of events that convert the pure energy of light into the free energy needed to power life. Oxygen-evolving photosynthetic organisms have two photochemical reaction center complexes, named Photosystems I and II that work together in a noncyclic electron transfer chain. Electrons are removed from water by Photosystem II (PSII), oxidizing it to molecular oxygen, which is released as a waste product. The electrons extracted from water are transported via a quinone and the cytochrome b_6f complex to Photosystem I (PSI) and, after a second light-driven electron transfer step, eventually reduce an intermediate electron acceptor, $NADP^+$ to form NADPH. [9,53] The water oxidation reaction is, thus, carried out by PSII (Fig.1.3), a multisubunit enzyme embedded in the lipid environment of the thylakoid membranes of plants, algae, and cyanobacteria.

The PSII core consists of two homologous proteins known as D1 and D2 and two further closely related chlorophyll (Chl)-binding proteins (CP), called CP43 and CP47. [54] Chlorophyll molecules and other pigments (e.g. β-carotene) absorb visible light and transfer the excitations to a reaction center where charge separation occurs. All the redox active cofactors involved in the energy conversion process are bound to the D1 and D2 proteins and the following sequence of reactions occurs

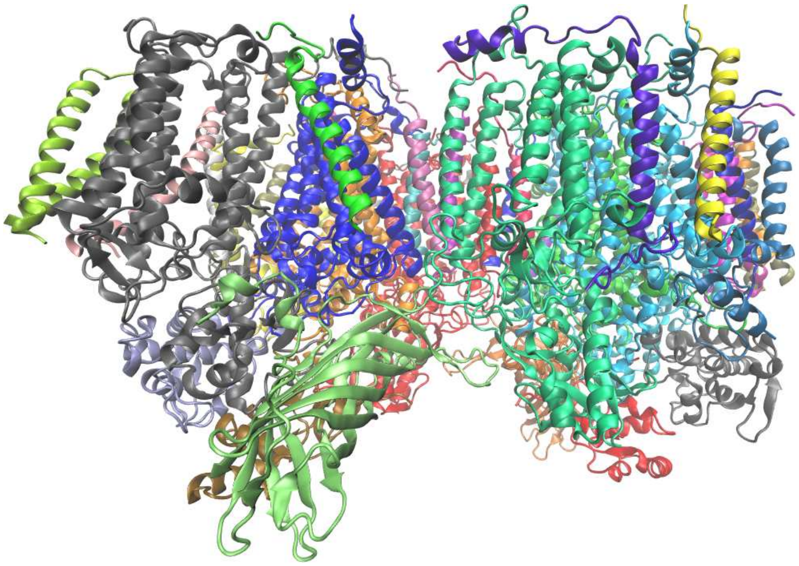

Fig. 1.3: Overall structure of PSII dimer from Thermosynechococcus vulcanus at a resolution of 1.9 Å(pdb code 3ARC). [54]

(see Fig.1.4 to follow the process): a special form of Chl *a* (P680) acts as an exciton trap and is converted to a strong reducing agent after excitation to P680*. P680* reduces a pheophytin *a* molecule (Pheo$_{D1}$) in a few picoseconds to form the radical pair state P680$^{\bullet+}$Pheo$_{D1}^{\bullet-}$.

Within a few hundred picoseconds, Pheo$_{D1}^{\bullet-}$ reduces a firmly bound plastoquinone molecule Q$_A$ to produce P680$^{\bullet+}$Pheo$_{D1}$Q$_A^-$. P680$^{\bullet+}$, with its very high redox potential ($>$ 1 V), oxidizes a tyrosine residue (Y$_Z$) to form Y$_Z^{\bullet+}$P680Pheo$_{D1}$Q$_A^-$ on a nanosecond time scale. This is followed by the deprotonation of Y$_Z^{\bullet+}$, by an histidine base (His190), to form a neutral radical Y$_Z^{\bullet}$. This Histidine residue play a crucial role; indeed, its removal by mutagenesis shuts down photosynthesis. Loss of a single base is sufficient to disrupt an enormously complex apparatus with multiple linked functional elements and hundreds of thousands of atoms. In the millisecond time

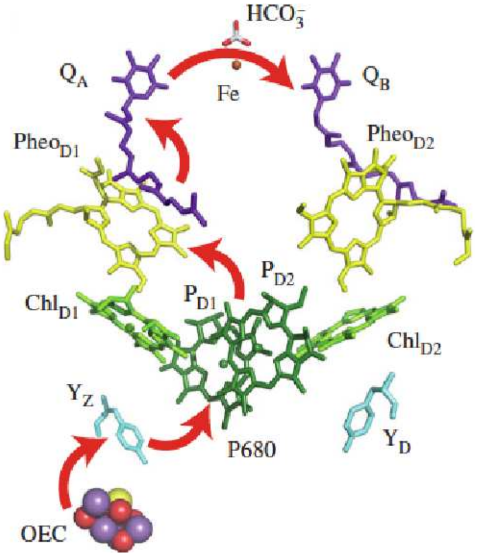

Fig. 1.4: Electron transport chain of PSII. Image taken from ref. [7].

domain Q_A^- reduces a second plastoquinone Q_B to form $Y_Z^\bullet P680Pheo_{D1}Q_AQ_B^-$ and at about the same time $Y_Z^\bullet$ extracts an electron from the water splitting site called oxygen evolving complex (OEC). [9, 53] This is a cluster of four Mn ions and a Ca ion surrounded by amino acid side chains, of which seven provide ligands to the metals (Fig. 1.5).

The metal cluster is organized as a cubane-like structure composed of three Mn ions and the Ca^{2+} linked by oxo-bonds with the fourth Mn attached to the cubane via one of its bridging oxygens together with another oxo bridge to a Mn ion of the cubane. Four water molecules were found to be associated with the Mn_4Ca cluster: two of which were coordinated to a manganese ion and the other two to the Ca^{2+}. A second photochemical turnover reduces Q_B^- to Q_B^{2-} which is then protonated to plastoquinol and released from the Q_B binding site of PSII into the lipid bilayer

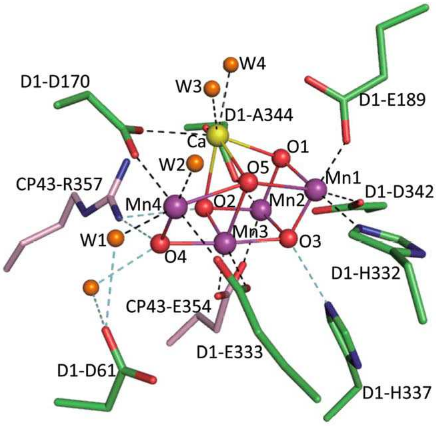

Fig. 1.5: Structure of the Mn4CaO5 cluster and its ligand environment. Manganese, purple; calcium, yellow; oxygen, red; D1, green; CP43, pink.Image taken from ref. [54].

where it is subsequently oxidized by PSI via the cytochrome b_6f complex. Two further photochemical turnovers provide a cluster of four manganese ions and a calcium ion (Mn_4, Ca^{2+}) with a total of four oxidizing equivalents, which are used to oxidize two water molecules to form dioxygen. [9, 53]

The increasing improvement in resolution of the PSII structure in conjunction with reliable theoretical models allows for a gradual understanding of the natural water splitting mechanism.

Of course, this paves the way for the development of new molecular assemblies suitable to mimic the overall water splitting process in an artificial photoelectrochemical system to generate solar fuels.

The present thesis aims to give an important contribution in this line providing new theoretical insights to support the future design strategies of such molecular assays.

Chapter 2

Photoinduced Electron Transfer in Rhodamine dyes

Rhodamine dyes, are founding an increasing number of applications as molecular fluorescence probes in different fields ranging from material science, to chemistry and biology, mainly thanks to their peculiar photophysical properties, such as high photostability, sensitivity and selectivity [55–64]. Nevertheless, in spite of the large amount of experimental and theoretical studies published along the decades, [65–74] a clear and complete picture of the photophysical behavior of rhodamines is far to be fully and unambiguously established. All the experimental observations claim for a higher degree of comprehension of the excited state decay pathway(s) taking place in such class of molecules, if one aims at obtaining a full control of their photophysical behavior, so to achieve a rational design of modern optical sensors.

Several models have been proposed to rationalize the different quantum yield in molecules belonging to the rhodamine series. Nonetheless, there is not a general consensus on which quenching mechanisms affect the fluorescence emission.

Historically, one of the most corroborated theory indicates a structural rearrangement corresponding to a decrease of the C-N bond order upon the $S_0 \rightarrow S_1$ excitation, as the responsible for non-radiative paths opened through the amino groups torsional motions. [70–74] For this reason, rhodamine dyes are usually given as a prototypical examples of the so called Twisted Intramolecular Charge Transfer (TICT) mechanism. [75] Nevertheless, several arguments against the TICT hypothesis exist, [76, 77] and other mechanisms have been debated in literature.

More recently, photoinduced electron transfer was proposed as a quenching mechanism to control the fluorescence properties of Si-Rhodamine-Based NIR fluorescence probes. [60, 78] In these Si-Rhodamines a PET takes place from the phenyl group (acting as the electron donor moiety) to the xanthene ring (behaving as the electron widthdrawing group). [60, 78] On the same line, Liu and coworkers discussed the possibility of an intra-molecular PET occuring in Rhodamine B and its derivatives involving the dialkylated amino groups as electron donors [79], while Yan-qiang and coworkers characterized an ultrafast intermolecular PET between Rhodamine 101 dye and N,N-diethilanyline from a spectroscopic point of view. [80]

More in detail, the main idea is that a dark state (with a strong charge transfer character) can interconvert with the bright fluorescent state in the specific cases where a low quantum yield of fluorescence is detected. [81, 82] Remarkably, this non radiative decay can be formally interpreted as an intramolecular PET.

The theoretical modeling of such type of process is far to be trivial from a theoretical point of view, especially at TD-DFT level. The main problem in this case, along with those previously defined in section 1.1, stems from the correct description of the excited states Potential Energy Surface in regions close to the crossing points between different electronic states or even in regions where they become very close in energy (near degenerate). As a matter of fact, the Born Oppenheimer approximation breaks down in these regions, the non adiabatic coupling terms becoming infinite at the degenerate points.

In this context, qualitative and quantitative tools enabling the characterization of excited state potential energy surfaces are becoming appealing and promising to help for the in-silico design of new fluorescent probes. Recently, a new density based index, the D_{CT} index (see Appendix A for other details), was developed to quantify (i.e. give a measure) the 'degree' of the charge transfer character associated to a given electronic transition [19]. Shortly, the D_{CT} index gives a measure of the electronic reorganization upon the vertical excitation, representing the distance between centroids of charges associated to the density increase and decrease upon the excitation, respectively. [19]

This index, originally devised as a diagnostic tool to identify the erratic behavior of standard DFT approaches in the description of through space CT excitations, has found other applications, such as a measure of the charge separation efficiency of dyes belonging to different push-pull dyes families [19,83–86] or, more recently, as a simple way to characterize stationary points on excited state PES associated to an

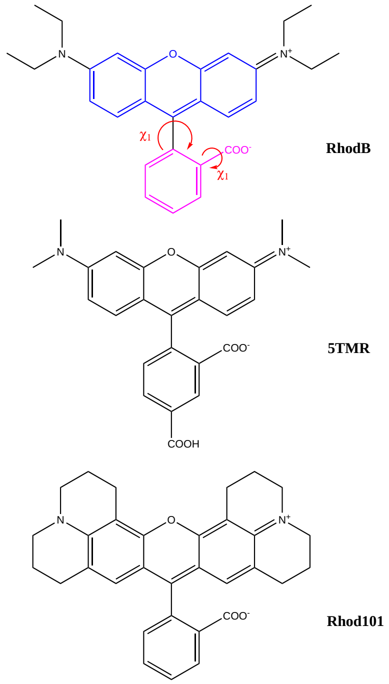

Fig. 2.1: Schematic structure and labeling of the rhodamines analyzed in this work together with the relevant torsional angles discussed (χ_1 and χ_2)

Excited State Proton Transfer event. [87]

In this chapter, this index will be used to assess and quantify the nature of excited states involved in the PET process near the region of their intersection, and, in particular, to get insights on the interconvertion process to the dark state responsible for the quencing. We focused on three Rhodamine derivatives namely the Rhodamine B (RhodB), the 5-carboxytetramethyl-rhodamine (5TMR) and the Rhodamine 101 (Rhod101) (see Fig. 2.1 for their structural formula).

2.1 Ground and Excited State structural and photophysical features

The structural formula of the three rhodamine dyes investigated are reported in Fig. 2.1 together with their labelling.

In this context it is worth recalling that all rhodamine dyes present a common skeleton constituted by a diamino-xanthene ring with a pendent carboxyphenyl substituent (refer to Fig. 2.1).

Two out of the three molecules (namely RhodB and 5TMR) display very low quantum yield as commonly observed for dialkyl- and tetraalkyl- amino and, at variance with other derivatives, the quantum yield of these compounds is also strongly dependent on pH, temperature and viscosity. [68, 69, 88] On the other hand, the Rhod101 molecule displays a significantly high quantum yield. Quite interestingly, this classification based on low and high quantum yield rhodamines coincides with rhodamines characterized by symmetric and asymmetric S_1 minimum structures, respectively. Starting from this observation, we considered the hypothesis that, in symmetrical rhodamines, a quenching internal conversion mechanism could be activated by rotation around the χ_1 and χ_2 torsion angles (refer to Fig. 2.1 for labeling) leading to a more stable, but dark, excited state. Indeed, both RhodB and 5TMR molecules in the Frank Condon region are characterized by the presence of two closely lying state: a bright Locally Excited (LE) state, centered on the xanthene moiety, and a dark Charge Transfer (CT) state corresponding to a transition from

	$\lvert\chi_1\rvert$		$\lvert\chi_2\rvert$	
	S_0	S_1	S_0	S_1
RhodB	94.84	92.26	0.01	0.05
RhodB$_{asym}$	–	62.55	–	19.15
5TMR	94.57	92.37	0.01	4.70
5 TMR$_{asym}$	–	62.77	–	19.19
Rhod101	117.17	123.87	33.82	39.39

Table 2.1: χ_1 and χ_2 dihedral angles (in degrees, refer to Fig. 2.1) computed for rhodamine dyes optimized in the ground (S_0) and first excited singlet (S_1) state at the B3LYP-D/6-31+G(d,p)/CPCM and TD-B3LYP-D/6-31+G(d,p)/CPCM levels of theory, respectively

the carboxyphenyl to the xanthene group (see below). Both relative energy of these two states and their intensity are expected to depend on the relative orientation of the two subgroups present in the molecule actually ruled by the χ_1 and χ_2 torsion. Indeed, since χ_1 represents the relative orientation of the phenyl and the xanthene rings, and χ_2 describes the rotation of the carboxy group with respect to the phenyl ring, any change from the $\chi_1 = 90°$ and $\chi_2 = 0°$ arrangement will account for the overall distortion of the two main moieties in rhodamine from the ideal C_s symmetry.

In Tab. 2.1 values of χ_1 and χ_2 dihedral angles computed for rhodamine optimized in the ground (S_0) and first singlet (S_1) excited states are reported. From these values it is possible to notice that, both at the ground and the first excited state RhodB and 5TMR possess a symmetric structure, with the xanthene and phenyl planes almost perpendicular and the carboxyl group lying in the phenyl plane. On the other hand, the Rhod101 dye is rather unsymmetrical, the carboxyl group being tilted of about 30-40 degrees with respect to the phenyl ring, this latter being far from orthogonality with respect to the xanthene plane.

This type of minimal energy structures, as already noticed for the ground state in a previous work [89], results from the subtle balance between coulombic and non classical interactions involving the two rings which are also modulated by the presence of solvent of different polarity. Indeed, Coulombic attraction and steric repulsion between the polar negatively charged carboxy group and the positively charged xanthene one favor the full symmetrical structure as in the case of RhodB and 5TMR. On the other hand, stabilizing dispersion interactions between the carboxy substituent and the xanthenes may favor an asymmetrical arrangement, as in the case of Rhod101. Furthermore, the overall structure can be modulated by the presence of the polar solvent which may favor conformations displaying a higher exposure of the carboxylic group to the solvent, leading to stabilizing solute-solvent interactions.

Analyzing the vertical transition energies reported in Table 2.2 it can be noticed that in all cases the first absorption corresponds to a $\pi - \pi^*$ excitation (LE state) centred on the xanthene moiety characterized by a high oscillator strength (intensity). On the other hand, the second electronic transition presents a different character depending on the nature of the amino group carried by the xanthene moiety. In the case of RhodB and 5TMR, this state is of intramolecular CT character, corresponding to a transition from the carboxyphenyl group to the xanthene unit, while in the case of Rhod101 this state is still of LE nature, and it is centred on the xanthene.

	S_1			S_2		
	Absorption	Oscillator str.	Character	Absorption	Oscillator str.	Character
RhodB^a	2.66	f=0.9745	LE	2.96	f=0.1323	CT
5TMR ^{a}	2.66	f=0.9111	LE	2.98	f=0.1321	CT
Rhod101	2.35	f=1.2563	LE	2.86	f=0.0203	LE

a) Ref. [89]

Table 2.2: Absorption energies (eV) and oscillator strength (a.u.) of rhodamine dyes calculated at the TD-B3LYP-D/6-31+G(d,p)/CPCM level of theory

	Relaxed S_1			Vertical S_2 at Relaxed S_1 geometry			
	Energy	Oscil. str.	D_{CT}	Energy	Oscil. str.	D_{CT}	Exp.
RhodB	2.41^a	1.2200	1.201	2.76	0.1504	2.474	2.18^b
RhodB$_{asym}$	1.45	0.0300	2.599	2.34	1.0862	1.200	
5TMR	2.40^a	1.1706	1.375	2.77	0.1554	2.477	2.18^b
5 TMR$_{asym}$	1.51	0.0432	2.546	2.29	0.9722	1.443	
Rhod101	2.25	1.1904	1.672	2.71	0.0006	2.631	2.06^c

a) [89] b) Ref. [90]; c) Ref. [79]

Table 2.3: Relaxed S_1 and vertical S_2 excited state energies (in eV) of rhodamine dyes calculated at the TD-B3LYP-D/6-31+G(d,p)/CPCM level of theory. Available experimental values are reported for comparison

Relaxation of the first excited state in the Franck Condon region led to the structures and emission energies reported in Tab. 2.1 and Tab. 2.3, respectively. Generally, and in agreement to what previously reported in litterature [89], the level of theory used allows to obtain a good agreement between observed and computed emission energies, with an average error of about 0.15 eV. The nature of the emitting state is further confirmed by the analysis of the associated D_{CT} index. Indeed, in the case of RhodB it results that the distance between the two barycenters of density distribution in the Franck-Condon region is of 1.306 Å and 2.474 Å for the first -relaxed- and second -vertically computed- excited state, respectively (Table 2.3). These data clearly show the larger electronic density reorganization involved in the case of the second excited state and it allows to confirm its intramolecular charge transfer character, in agreement with the orbital picture discussed for vertical excitation. Therefore, both in the case of RhodB and 5TMR basically in the Franck-Condon region, corresponding to symmetric structure with orthogonal rings, the first relaxed excited state correponds to a bright Locally Excited state (LE) which is found to lye roughly 0.3 eV below a dark CT state. On the other hand, in the case of the asymmetric Rhod101, while the lowest lying state is also of LE character, no closely lying CT states are found.

In order to verify the hypothesis concerning the possibility of a conversion of the bright LE state to a dark CT state by internal rearrangement around $|\chi_1|$ and $|\chi_2|$ in the case of symmetric rhodamines the S_1 structures of RhodB and 5TMR was also optimized starting from an initial distorted guess geometry ($|\chi_1|$=110°, $|\chi_2|$=20°). Starting from this distorted structure, both RhodB and 5TMR relaxed on asymmetrical singlet excited states (here referred to as RhodB$_{asym}$ and 5 TMR$_{asym}$, respectively) showing clearly asymmetrical structures with $|\chi_1|$ of 118° and 123° for RhodB and 5TMR, respectively, as reported in Tab. 2.1. From an energetic point of view, these singlet states are characterized by a significantly lower energy with respect to those of the corresponding symmetric structures and by a very low oscillator strength (f=0.04 a.u., Tab. 2.3), in contrast with the high value of oscillator strenght computed for symmetric excited singlet state minimum discussed above (f=1.22 and f=1.17, Tab. 2.3).

The analysis of the D_{CT} index computed for these asymmetric singlet states allows to clearly define them as intramolecular CT ones with of D_{CT} 2.599 and 2.546 Å , respectively for RhodB and 5TMR. On the other hand, the -vertically computed- second excited state shows a clear π-π^* locally excited state character with D_{CT} of 1.200 and 1.443 Å , respectively. Therefore, both for RhodB and 5TMR not only the two excited states computed in the Franck-Condon region have interconverted upon torsion along the dihedral angles but also, the LE/CT state shows a sizable (about 0.1 Å) decrement/increment of the electronic density reorganization upon transition. Furthermore, due to the strong stabilization of the dark CT state, the energy difference between the first and the second excited state increases up to roughly 0.9 eV for both RhodB and 5TMR in their asymmetric geometry. In the case of Rhod101 on the other hand starting from a symmetric or asymmetric guess structure for the optimization of the first excited state has no impact on the final results, always corresponding to the same LE distorted structure as reported in Tab. 2.1 and Tab. 2.3. This is due to the absence of a closely lying CT state which maybe sufficiently stabilized by a structural distorsion.

2.2 Modeling the PET process

In order to further investigate the possibility of conversion of the bright LE into the dark CT state upon rotation around the χ_1 and χ_2, in the case of rhodamines presenting a symmetric ground state structure, a linear synchronous path (LSP) consisting of 20 points linking the symmetrical and asymmetrical excited state minima for RhodB was constructed. For each of these structures the second excited state was vertically computed. Basically, this linear synchronous coordinate (c_{LSP}) represents the structural evolution from the symmetrical Franck Condon region (c_{LSP}=0), where the emitting state is a bright LE one to the asymmetrical minimum (c_{LSP}=1) corresponding to a dark CT state. In order to define the nature of the excited states, the D_{CT} index was computed for both first and second excited state for all points along the path. The computed energy profiles associated to the first and second excited states are reported in Fig. 2.2 while the associated D_{CT} are reported in Fig. 2.3.

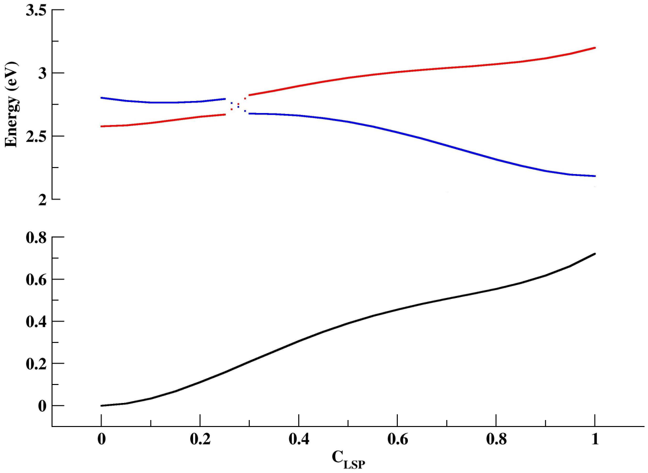

Fig. 2.2: Evolution the energy associated to the LE and CT excited states (in eV) of RhodB along the LSP connecting the symmetrical (c_{LSP}=0) to the asymmetrical c_{LSP}=1 excited state minima

From the analysis of these figures it is clear that the two excited states cross in the region around c_{LSP}=0.25, the detailed study of the crossing being clearly

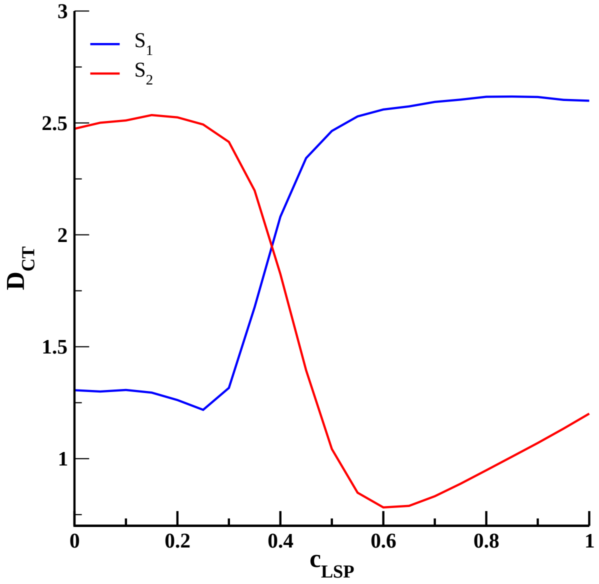

Fig. 2.3: Evolution of the D_{ct} (in Å) associated to the first S_1 and second S_2 excited states computed along the LSP connecting the symmetrical (c_{LSP}=0) to the asymmetrical (c_{LSP}=1) excited state minima of RhodB

impossible at the level of theory here applied. Indeed, from the combined analysis of the D_{CT} it is possible to point out that in the crossing region also the character of the transitions is inverted. The first excited state showing a more local character, translating into a lower D_{CT} value, in the case of symmetric structures becomes of a more marked CT character moving towards the asymmetric minimum (c_{LSP}=1). The inversion of the two states thus allows for the conversion of the emissive bright LE state present in the Franck Condon region to the dark CT and more stable distorted minimum thus justifying a low yield for this compound.

Nonetheless the question still unanswered is related to the electronic reason that causes the inversion of the excited states. Analysis of the molecular orbitals mainly involved in the one-electron excitations describing at TD-DFT level the excited states for RhodB, allows clarifying for this point. Actually, at any point of the LSP, the first (or second) excited state corresponds essentially to a one electron excitation from the HOMO (or HOMO-1) to LUMO. While the LUMO (reported in Fig. 2.4) is completely insensitive to the structural rearrangement occurring along the LSP and keeps always the same nature (localized on the xanthene unit) and energy, this is not the case for the HOMO and HOMO-1 as shown in Fig. 2.4. For the symmetric structure, the HOMO is essential a π xanthenic orbital with associated orbital energy (ϵ) of -0.211 a.u., while the HOMO-1 is mainly localized on the carboxylate group on the phenyl substituent lying roughly 0.018 a.u. below the HOMO. As a consequence the HOMO→LUMO excitation leads to the LE first excited state responsible for the radiative decay providing fluorescence. The HOMO-1→LUMO excitation, on the other hand, leads to a dark CT excited state.

Considering the asymmetrical minimum (c_{LSP}=1), we notice that the HOMO and HOMO-1 actually corresponds to carboxylate and xanthene centered orbitals, respectively with corresponding ϵ values of -0.195 a.u. and -0.218 a.u. That means that the HOMO and HOMO-1 have inverted with respect to the symmetrical minima. This inversion is related mainly to the strong destabilization of the doubly occupied carboxylate centered orbital while the xanthene centered one is actually almost unaffected. The destabilization of the carboxylate orbital is related to the increasing repulsion with the xanthene π systems which is also responsible for the increase in the total energy of the ground state of the molecule. Therefore molecu-

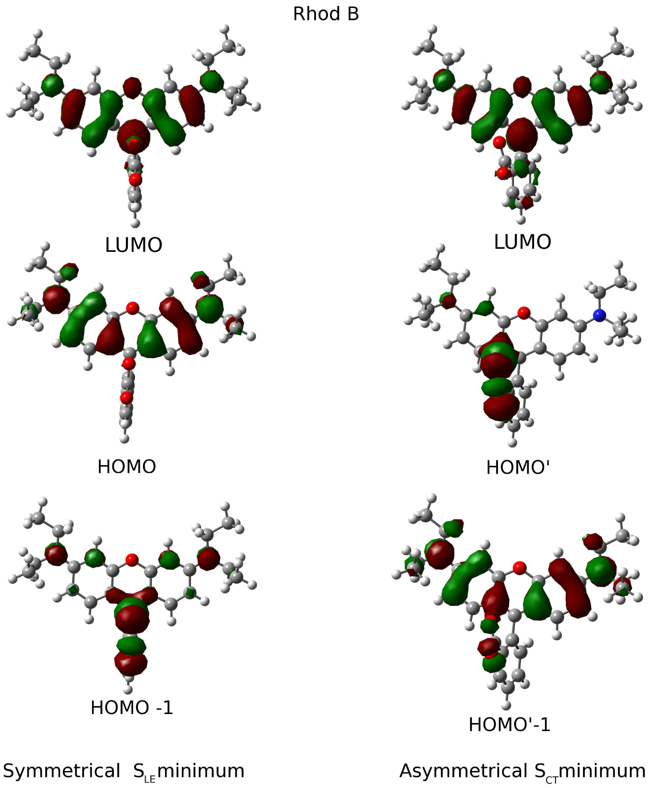

Fig. 2.4: LUMO, HOMO and HOMO-1 computed for symmetrical and asymmetrical RhodB structures corresponding to the optimized first singlet excited state

lar vibrations, in particular those involving the relative orientation of the xanthene and phenyl rings, promote the PET quenching mechanism, affecting the energy gap between the LE and CT electronic states and creating the non adiabatic coupling between them. This connection has been recently proven by non-adiabatic molecular dynamics to describe a PET from PbS Quantum Dots to RhodB molecules. [91]

Noteworthy, the frontier orbitals inversion when going from a symmetrical to an asymmetrical arrangement can be schematized as an hole transfer from the xanthene to the carboxylate moiety at the excited state as shown in Fig. 2.5.

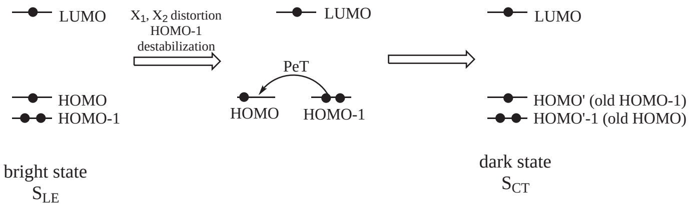

Fig. 2.5: Scheme of the photo induced electron transfer mechanism active in RhodB

In this simplified orbital picture, the starting first excited state is the bright state LE state populated in the Franck Condon region, schematically represented by singly occupied HOMO and LUMO and a doubly occupied HOMO-1. Upon relaxation, corresponding to the distortion of xanthene and phenyl rings, the HOMO-1 undergoes a destabilization and eventually switches with the HOMO. This orbital interchange actually allows an electron transfer from new HOMO (previously HOMO-1) to HOMO-1 (previously HOMO), leading to the final dark state.

The quenching mechanism described above is triggered by the destabilization of carboxylate group orbital so that this mechanism should be active in principle for all rhodamines. Indeed, for rhodamines that show no contribution stemming from the carboxylate group to the lowest lying excited state, this quenching mechanism is completely negligible. This is actually the case of all asymmetric rhodamines since in such case the carboxy group always contributes to more internal orbitals. As an example, in Fig. 2.6 the HOMO-1 computed for the symmetric structure of RhodB, 5TMR can be compared to that computed for the Rhod101.

For the latter system (Rhod101), at variance with dialkyl-and tetraalkyl- amino rhodamines, the HOMO-1 in mainly localized on the xanthene ring. It is reasonably

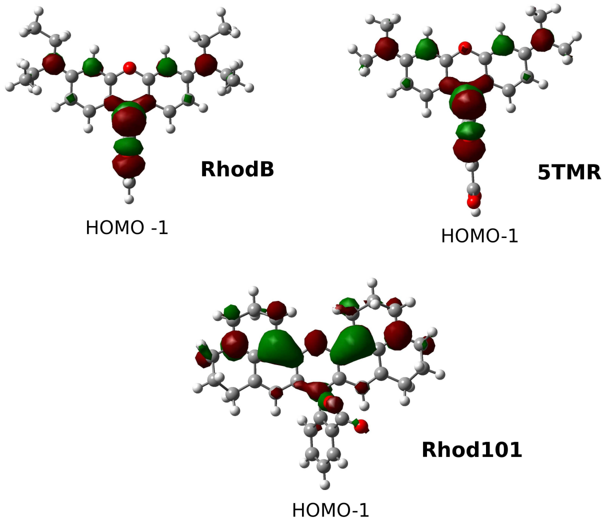

Fig. 2.6: HOMO-1 orbitals computed for RhodB, 5TMR and Rhod101 their Franck Condon first excited state minimum energy structure (symmetric structure for RhodB and 5TMR; asymmetric structure for Rhod101

to assume that in this case the above discussed quenching mechanism is precluded and this is also the reason why a single minima on the first excited state potential energy surface of LE character is found, always corresponding to a distorted structure.

In conclusion this modeled photoinduced electron transfer process can be a possible non radiative decay pathway able to explain the different quantum yield observed for different type of rhodamine dyes

Most of all this mechanism, is active only for rhodamines where two different excited state of bright (LE) and dark (CT) character are sufficiently close in energy in the Franck-Condon region. We hope that the elucidation of this non-radiative decay path may help the design and synthesis of new systems and, in particular, of rhodamines with enhanced emission properties obtained by the suppression of this de-activation pathway by chemical modification (such as inclusion of bulky, but electronically inhert substituent or by ridigification of the molecular skeleton).

Moreover, our findings encourage the use of density based indices to study processes affecting excited state reactions characterized by a drastical change in the excitation nature in order to rationalize the photophysical behavior of complex molecular systems.

Chapter 3

Ab-initio molecular dynamics combined with different solvation models for simulating Excited State Proton Transfer

The detailed knowledge of excited state proton transfer mechanisms in complex environments is of paramount importance in chemistry. As pointed out in section 1.2, the exploration of different time scales in a very complex reaction space represent the main challenge for theoretical approaches in simulating ESPT processes.

In this chapter we taked up the challenge, investigating the mechanism and driving forces of ESPT reactions by means of excited state AIMD simulation adopting different solvation models to represent the environmental effects (see Figure 3.1).

On the one hand we analysed the ESPT occurring between a coumarine and an imidazole molecule in toluene solution adopting a fully implicit model for the solvation, i.e. the Polarizable Continuum Model. [20] On the other hand we studied the ESPT from a dipicolinium cyanine dye towards water solvent molecules, considering

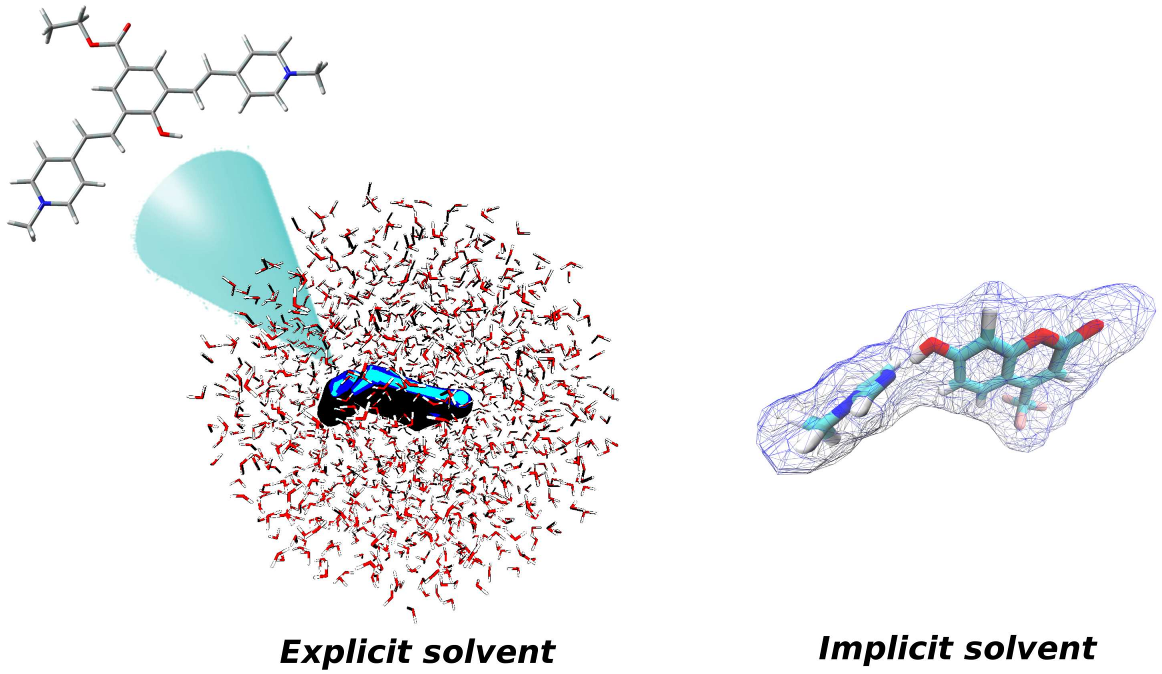

Explicit solvent

Implicit solvent

Fig. 3.1: Explcit versus implicit representation of the solvent.

the solvent coordinate in an explicitly way through a discrete/continuum solvation model, enforcing non-periodic boundary conditions. [92–94]

3.1 Modeling ESPT with implicit solvation model: the coumarine case

As first pilot application, we choose the ESPT reaction occurring between the 7-hydroxy-4-(trifluoromethyl)coumarin photoacid and the 1-methylimidazole base molecules in toluene solution (see Fig. 3.2), analysing its mechanism and driving forces.

This system was recently deeply characterized by Papanikolas and co-workers from a spectroscopic point of view using ultrafast pump probe and time-resolved

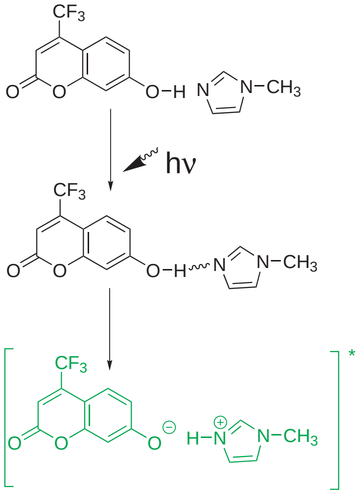

Fig. 3.2: Schematic representation of the ESPT reaction analyzed in this work.

methods. [95, 96] As matter of fact, the photoexcitation induces changes in the electronic structure of this chromophore, regarding in particular the oxygen atoms electronic density. [87] When a sufficient amount of a base like 1-MeId is present in the solution, the new arrangement of the electronic density eventually leads to the coumarin tautomer as the dominant form in the excited state, formed by ESPT reactions. Moreover the pK_a decreases from about 7 in the ground state [95] to a value on the order of $-7.4/-8.9$, as calculated at the first singlet excited state. [87]

The photo-triggered reactivity between CouOH and 1-MeId was recently theoretically investigated examinating the photophysical features and the reaction mechanisms essentially *via* a statical approach. [87,97] More in details, the characterization of minima on the ES PES and a bidimensional energy scan in terms of the principal structural parameters composing the reaction coordinate were carried out, showing that methods rooted in Time-Dependent Density Functional Theory are sufficiently accurate to give a physically sound description of the process. Following this line we compared the intrinsic and the dynamical reaction pathways, obtained by integrating the intrinsic reaction coordinate (IRC), and by performing ab-initio simulations of molecular dynamics, respectively. Time-dependent density functional theory and polarizable solvation continuum models [98, 99] were adopted to define the excited state potential energy surface.

3.1.1 Structural and energetic features of the excited state IRC

The excited state reaction path was constructed by integrating the intrinsic reaction coordinate starting from the the transition state (TS) of the proton transfer reaction on the ES PES. The nature of the excited state TS was confirmed by frequencies calculation, performed by using numerically calculated TD-DFT energy second derivatives with respect to nuclear coordinates. In particular, an imaginary frequency at ≈ -649 cm^{-1} has been found (see Figure 3.3 for the displacement vectors of the TS structure).

The scheme of integration over the excited potential energy surface was obtained by combining the first-order Euler predictor approach with a modified Bulrisch-Stoer integrator for the corrector algorithm. [30–34]

Before analysing in more detail the ESPT driving force, the energetic and structural features of the various structures obtained by the ES IRC will be shortly summarized here. The IRC energetic profile in Fig. 3.4 clearly illustrates the possi-

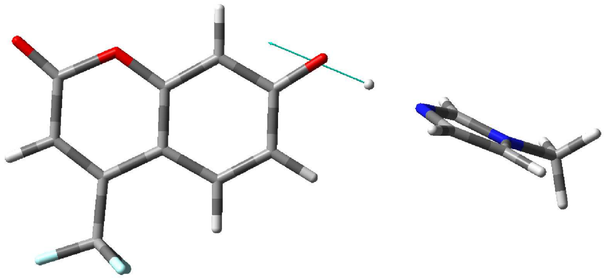

Fig. 3.3: Displacement vectors for the excited state transition state immaginary frequency calculated at the TD-B3LYP/6-31G+(d,p)/CPCM level of theory.

	CouOH+1-MeId	TS	CouO$^-$+1-MeIdH$^+$
CO	1.316	1.307	1.296
OH	1.081	1.202	1.417
NH	1.462	1.284	1.123
NO	2.541	2.483	2.539
CONH	-10.13	-8.73	-17.53

Table 3.1: Main structural parameters (Å and deg) computed for CouOH+1MeId, TS and CouO$^-$+1-MeIdH$^+$ in the excited state.

bility of getting a PT reaction in the excited state. More closely the ESPT product (CouO$^-$+1-MeIdH$^+$) is found to lie roughly 0.2 kcal/mol lower in energy compared to the reactant (CouOH+1-MeId) with a barrier of about 0.3 kcal/mol, providing evidence for a spontaneous PT at the excited state. The emission energy for CouO$^-$+1-MeIdH$^+$ is computed at 451 nm in strict agreement with the value of 460 nm assigned by Papanikolas and co-workers [95] to the emission from a configuration in which the proton is transferred to the base but remains hydrogen bonded to the hydroxycoumarin anion.

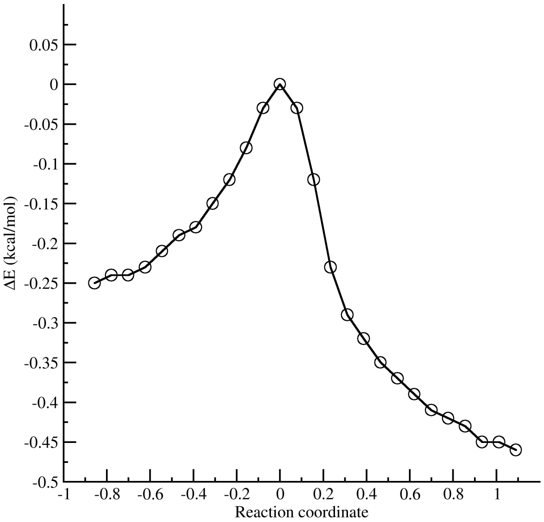

Fig. 3.4: Energy profile along the excited state IRC for the ESPT in the CouOH+1-MeId system calculated at the TD-B3LYP/6-31+G(d,p)/CPCM level of theory

The main structural parameters predicted for CouOH+1MeId (reactants), CouO$^-$+1-MeIdH$^+$ (products) and the transition state are listed in Table 3.1, while variation of significant distances (OH, ON, NH, and CO) along the reaction path is reported in Fig. 3.5. As expected, the OH and NH distances are the principal degrees of freedom involved in the reaction. In the transition state region both coordinates significantly change. The NH distance has a steeper variation compared to the OH one in the reactant zone (the NH and OH vary with slopes of 0.11 and 0.04 respectively), whereas the OH distance varies more rapidly than NH in the product zone (0.07 and 0.02 are the slopes for the variation of OH and NH respectively). The proton movement involves also other degrees of freedom as the NO and CO distances and the CONH dihedral angle, showing that the coumarine and the base move in a concerted way to facilitate the transfer event. In particular, starting from CouOH+1MeId, the

NO distance gradually decreases until reaching its minimum value (2.48 Å) in the transition state region. From here this distance gradually increases reaching its maximum value of 2.54 Å in the CouO$^-$+1-MeIdH$^+$ structure. The coumarine-base approach is also coupled to the reorientation of the 1-MeId molecule with respect to the coumarine plane, as shown from the variation of the CONH dihedral angle, which changes of about 8° when going from CouOH+1-MeId to CouO$^-$+1-MeIdH$^+$. During the transfer the CO distance undergoes a contraction of about 0.02 Å, in agreement with the change of the CO bond nature along the reaction path. The planarity of the two molecules is retained along the reaction path as a consequence of the extended π conjugated system.

3.1.2 IRC analysis by D$_{CT}$ electron density based index

The electron density redistribution upon the excitation along the IRC path can be analysed and described through density based indexes such as the D$_{CT}$ one, as also demonstrated in previous chapter. In Fig. 3.6 D$_{CT}$ values calculated along the IRC path are reported. The transition state region of the ESPT reaction represents the maximal charge separation developed during the reaction. The D$_{CT}$ index clearly describes this evidence assuming its maximum value (2.292 Å) exactly in the transition state zone. As matter of fact, starting from a value of about 2.285 Å in the reactant region the D$_{CT}$ increases reaching its maximum value at the TS, until quickly decreasing in the product zone, where it fluctuates around the 2.22 Å value. By the comparison of 3.4 and 3.6, it is clear that the highest energy arrangement of

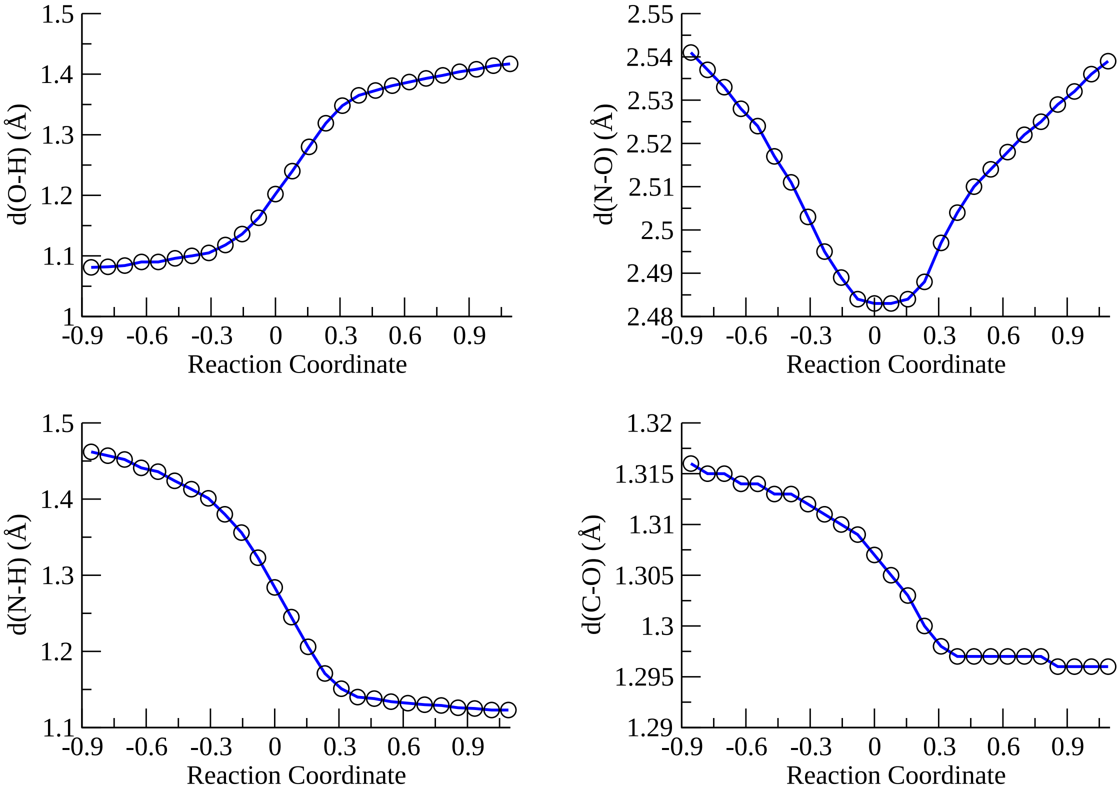

Fig. 3.5: Variation along the reaction path of the CouOH+1-MeId system structural parameters: OH (upper panel, left), ON (upper panel, right), NH (lower panel, left), and CO (lower panel, right)

the reaction (namely the TS) corresponds to the configurational space characterized by the maximum D_{CT}, and therefore by the highest charge transfer degree. The energy increase when going from the reactant to the transition state zone is coupled and driven by the growth of the charge separation. In the same way the reduction of the energy after the transition state is controlled by the depletion of the charge transfer degree. These features are nicely represented by the D_{CT} index along the IRC.

To investigate further the nature of the ESPT driving force we compared the

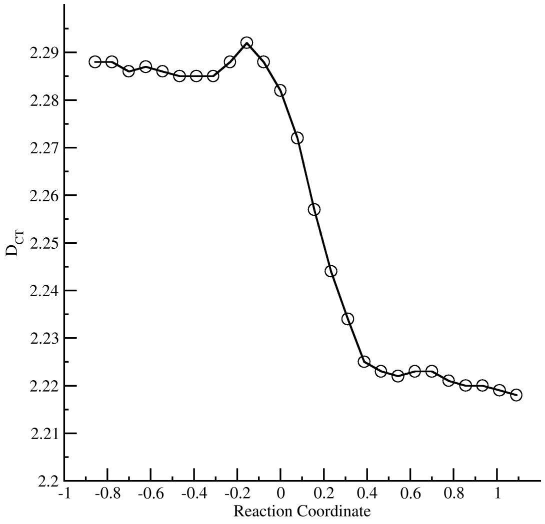

Fig. 3.6: Evolution of the D_{CT} (Å) associated to excited state IRC

energy gradient along the IRC path, namely the force, with the module of the D_{CT} derivatives with respect to the reaction coordinate (see Fig. 3.7). The former are calculated as Root Mean Square (RMS) values, while the latter with the finite differences method. Figure 3.7 shows that there is a well defined correlation between the forces driving the proton transfer and the variation of charge transfer extent represented by the D_{CT} index. The accordance is especially achieved in the transition state region, where both the forces and the D_{CT} derivatives show their maximum value. This in turn suggests that the principal driving force to the excited state proton transfer is the variation of charge transfer extent along the IRC path.

Interestingly, we recall that the time dependent part of TD-DFT excitation energy derivatives with respect to the nuclear coordinates, [35] depends on the change in the one particle density matrix between the ground and the excited state (P^{Δ}). [35,36] P^{Δ} in turn is strictly related to the difference between the excited and

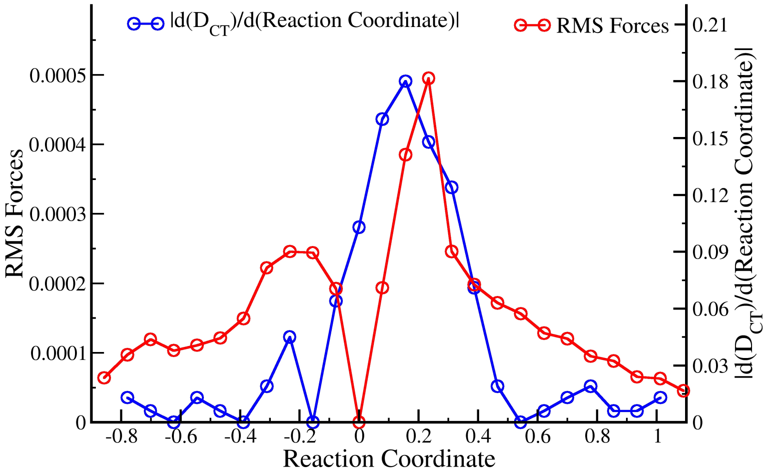

Fig. 3.7: Comparison of D$_{CT}$ and RMS forces evaluated along IRC

ground state dipole moments (Eq. 28 ref. [35]), namely to the charge rearrangement after the electronic excitation. At the same time the information on the charge rearrangement after the vertical excitation is innate in the D$_{CT}$ index, which is related to the dipole moments variation for construction. Thus we can conclude that for reactions driven by a strong variation of charge transfer extent the forces governing the movement along the ES PES (i.e. the energy gradient) can be nicely represented by the D$_{CT}$ derivatives with respect to the reaction coordinate.

3.1.3 Analysis of the ground state ADMP simulation

Before describing the excited state dynamics simulation, we spend few words on the ground state molecular dynamics. The ground state conformational space of the CouOH+1-MeId system in toluene was sampled by AIMD performed with the

	Optimizated value	$MeanValue \pm$ standard deviation
CO	1.34	1.34 ± 0.03
OH	1.01	1.01 ± 0.03
NH	1.67	1.74 ± 0.10
NO	2.69	2.72 ± 0.09

Table 3.2: Main structural parameters (Å) computed for CouOH+1MeId from ground state optimization and AIMD simulation.

Atom centered Density Matrix Propagation (ADMP) approach, [100–103] collecting a trajectory for 5 ps after an equilibration of 3 ps.

The mean value and standard deviation of some relevant structural parameters sampled by AIMD are compared with those obtained from the ground state optimization in Table 3.2. The distribution functions of CouOH+1-MeId main structural parameters are shown in the various panels of Fig. 3.8. From the inspection of Table 3.2 and Fig. 3.8 it is clear that the standard deviation evaluated from dynamics is generally small, indicating the sampling of fluctuations of the system in the Franck Condon region. Intermolecular degrees of freedom like the NO and NH distances show wider oscillations, more broadened distribution functions, and higher standard deviations (0.10 Å). The dynamics simulation confirms that at the ground state no spontaneous proton transfer occurs from CouOH to 1-MeId, in agreement with the experimentally known pK_a value of these species. Moreover a stable minimum corresponding to a hydrogen bonded neutral CouOH is formed.

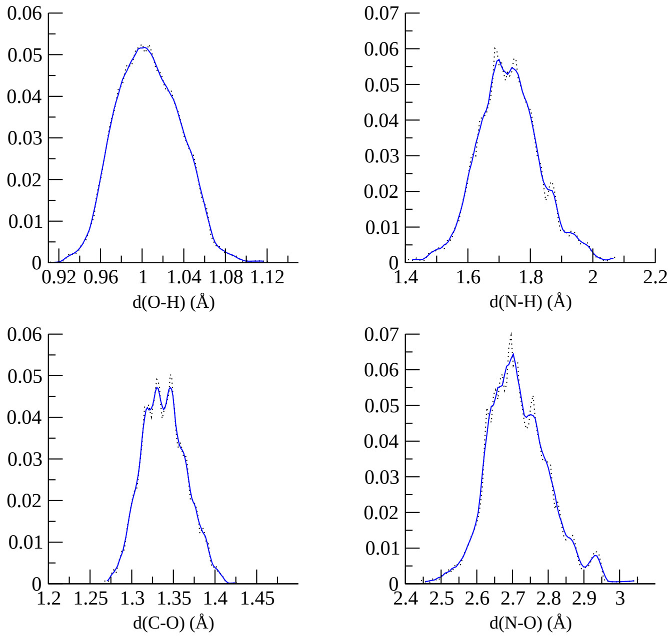

Fig. 3.8: Distribution functions of the CouOH+1-MeId main structural parameters obtained by ground state AIMD simulation.

3.1.4 Analysis of the excited state AIMD simulation

Starting from the ground state configurational space, five trajectories of excited state AIMD were collected. [16, 17] For all TD-DFT calculations performed on-the-fly during the dynamics, four excited states were kept, the first one being that of interest.

The different starting points for the excited state AIMD were chosen in order to represent, on average, the conformational space spanned by important degrees of freedom, such as the CO and NO distances. Starting values of CO and NO are given as fig. 3.9 .

In two cases, it was not possible to sample a well defined singlet state for more

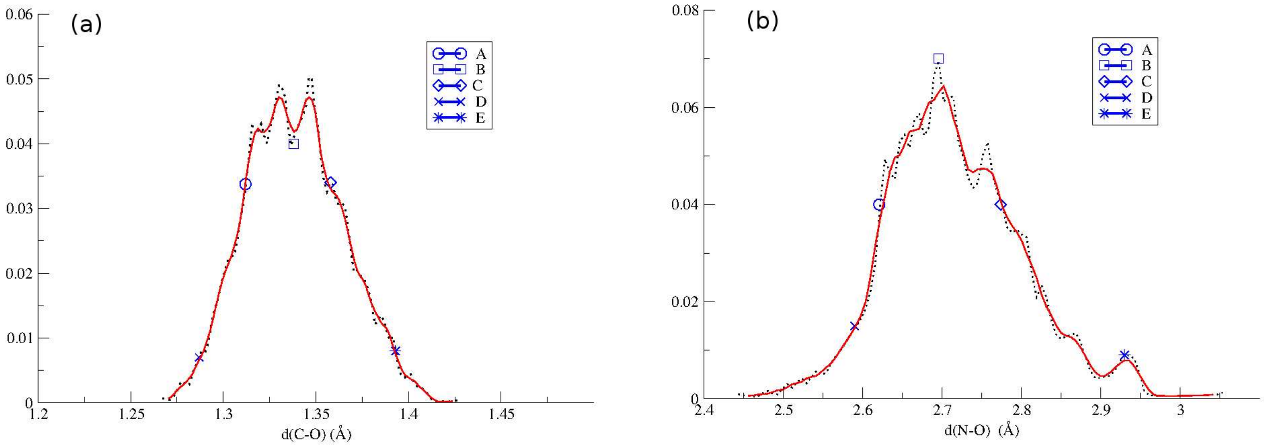

Fig. 3.9: Distribution function of CO (left panel (a)) and NO values (right panel (b)) sampled by ground state AIMD.

than few hundreds of femtoseconds. In the remaining cases, at least 1 ps has been collected for each trajectory, adopting a 0.2 fs value as time step.

Moreover the absorption values computed on these structures are on average 345 nm in accordance to the experimental value of 342 nm which Papanikolas and co-workers attribute to the CouOH hydrogen bonded to MeId. [95] The model chosen to represent the real system and the level of theory (see the text below) did not allow us to simulate a complete ESPT event in any of the sampled trajectories. Instead, several events of proton hopping between the donor and the acceptor were observed in all the cases, with a frequency depending on the proximity of the explored PES to a TS-like arrangement. In the following, we will discuss and analyze the trajectory showing the larger frequency of proton hopping events. It is important to underline here that a kinetic study, and therefore an adequate statistics of the ESPT is out of purpose of the present work, more focused on a detailed analysis of the ESPT mech

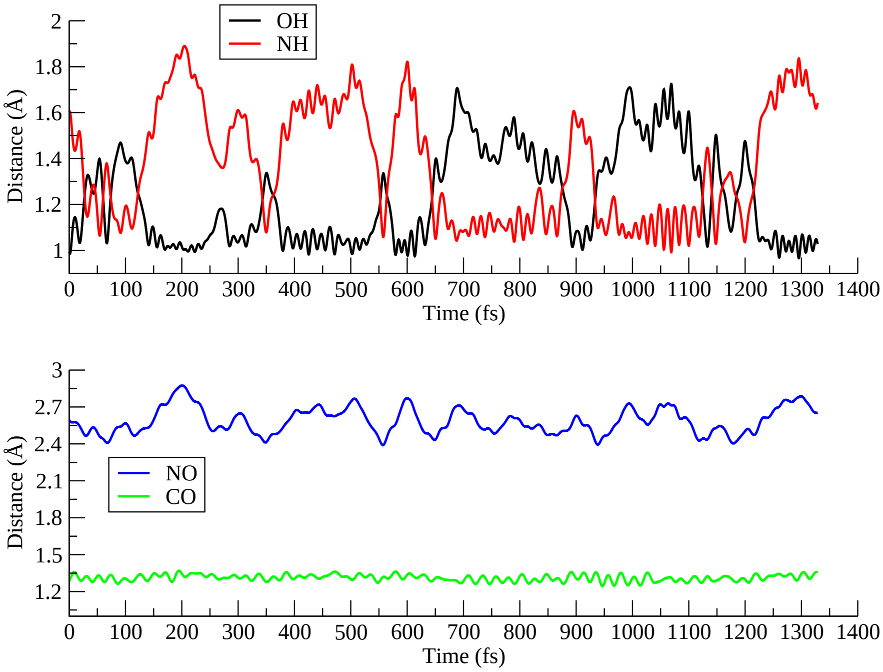

Fig. 3.10: Time evolution of important structural parameters of the CouOH+1-MeId sampled by the excited state AIMD.

The trajectory discussed here started from an initial configuration characterized by a CO and NO distance values falling in the ground state distribution tail (1.29 and 2.59 Å for CO and NO, respectively). The time evolution of the important structural parameters is shown in Fig. 3.10. By the comparison with the ground state data, it is clear that in the excited state the proton movement is more accentuated. As matter of fact, the electronic excitation leads to wider fluctuations of the OH and NH distances, resulting in the formation of a product-like arrangement ($CouO^{-}$+1-$MeIdH^{+}$) at about 0.7 ps after the excitation. This result is consistent with femtosecond transient stimulated emission data showing that a significant frac-tion of the stimulated emission appears within the instrumental resolution (800 fs). This early appearance is explainded by an ultrafast ESPT between CouOH and MeId. Thus upon a Franck-Condon excitation, the associated reaction dynamics spontaneously leads to the proton transfer. However, a complete PT event is not observed in 1.5 ps.

After this first hopping event, the proton goes back and forth between the coumarine and 1-MeId molecules during the sampled time. On the one hand this behavior is easily ascribable to the level of the electronic potential (DFT), which can slightly underestimate the energy barrier. As a consequence, there is an high probability by which the proton moves back along the reaction coordinate or, more in general, persists longer in the TS region. On the other hand the absence of the explicit solvent degrees of freedom implies the inability of the energy exchange among real degrees of freedom of the system. These two effects combine together leading to a continuous sampling of the transition state region and to the lack of a full exploration of the product region of the PES during the simulation. Finally, it is worth of note that coincidentally with each proton transfer the NO distance assumes minimum values of about 2.4 Å, while the CO distance oscillates around 1.3 Å. These values are in very good agreement with those adopted in the transition state structure (see Table 3.1).

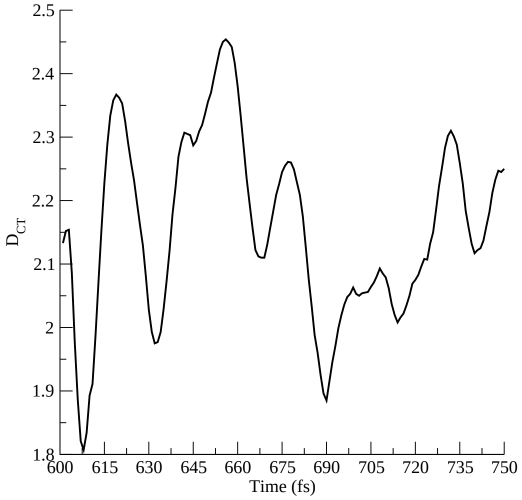

Fig. 3.11: Time evolution of D_{CT} in the 600-750 fs interval of the excited state AIMD.

3.1.5 Analysis of the excited state trajectory by D_{CT}

The possible use of a D_{CT} analysis to describe the ESPT reaction mechanism within AIMD has been also investigated. We considered a time interval $(600 - 750$ fs) of the ES AIMD simulation showing a PT event, extracting a configuration every 10 fs. Figure 3.11 shows the D_{CT} evaluated on these structures.

The dynamical picture gives a more complex representation of the reaction pathway with respect to the IRC, including fluctuations of molecular modes at finite temperature, and the D_{CT} evolution in time does not show a specific trend. Nonetheless we recognize that a configurational sampling more close to the TS region also corresponds to the highest charge transfer degree. In particular a transition state arrangement can be located around 660 fs: notably, in this region the D_{CT} parameter assumes its maximum values, confirming what was previously observed from the IRC analysis. We can also observe a correspondence between the CT extent (given by D$_{CT}$) and the time evolution of specific modes in different times of the trajectory. In particular Fig. 3.12, left panel, shows a correlation between the OH distance and the D$_{CT}$ values in the $610 - 660$ fs range. That means, in the time visiting a configurational space similar to the reactants evolving into the TS, the two parameters show a similar trend: the elongation of the OH distance, in this region, leads to an increase of the charge transfer degree, resulting in a D$_{CT}$ growth. Similarly, in the $660 - 750$ fs region, that is, when the transition state region evolves into the product-like PES, the D$_{CT}$ is more correlated to the NH distance fluctuations (see Figure 3.12, right panel). The D$_{CT}$ decreasing in this region is then related to the NH contraction leading to the formation of CouO^{-}+1-MeIdH^{+}. The product formation is thus accompanied by the lowering of the charge transfer extent and so by the D$_{CT}$ decreasing. Again, this trend mirrors what already is observed by the IRC analysis.

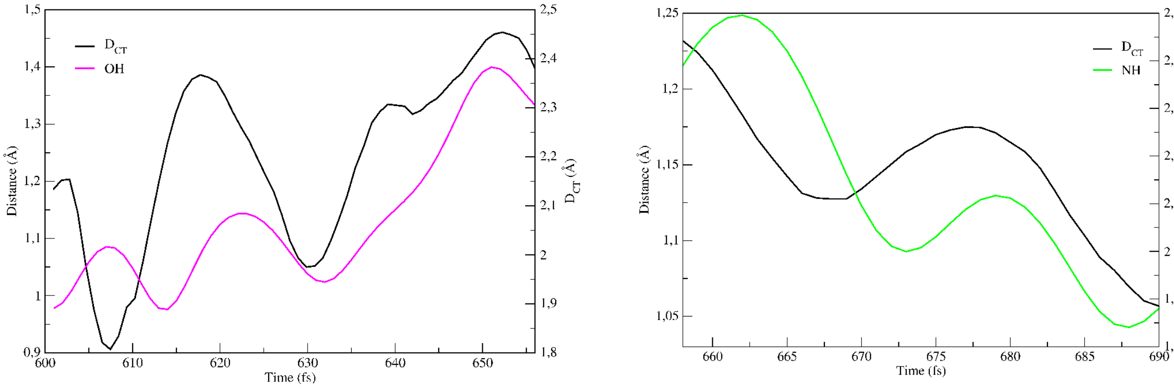

Fig. 3.12: Comparison of time evolution of some structural parameters and D$_{CT}$ values from the excited state AIMD.

The strictly accordance between the ES dynamics correlations and the ES IRC one, is a firts strong evidence to adopt AIMD based on TD-DFT potential as feasible, reliable and stable approach for the description of photo-triggered processes. Of course for a complete analysis including also the role of solvation dynamics, a more extensive sampling of excited state AIMD and the use of explicit solvation is desirable. This will be the main aim of the following section.

3.2 Modeling ESPT with explicit solvation model: the super photoacid case

In this section the solvent influence on both the kinetics and the mechanism of an ESPT reaction toward solvent molecules, has been deeply investigated. Excited state AIMD in conjunction with hybrid implicit/explicit model of the solvent were employed, to simulate the ESPT process with an explicit representation of the solvent coordinate.

As case of study the reaction taking place between the phenol-carboxyether dipicolinium cyanine dye (QCy9) (see Fig. 3.13 for its structure) and water solvent molecules was considered. Our interest in this system was motivated by the recent characterization of Huppert and co-workers (mentioned in section 1.2) [28], based on steady-state and time-resolved techniques, that classifies QCy9 as a super-photoacid. As matter of fact it exhibits a very large excited state proton transfer rate constant, $k_{PT} = 1 \times 10^{13} s^{-1}$, the largest k_{PT} value reported in the literature so far. This constant is the same independently on the nature of the solvent.

The QCy9 fluorochrome consists of a phenol to which three functional groups

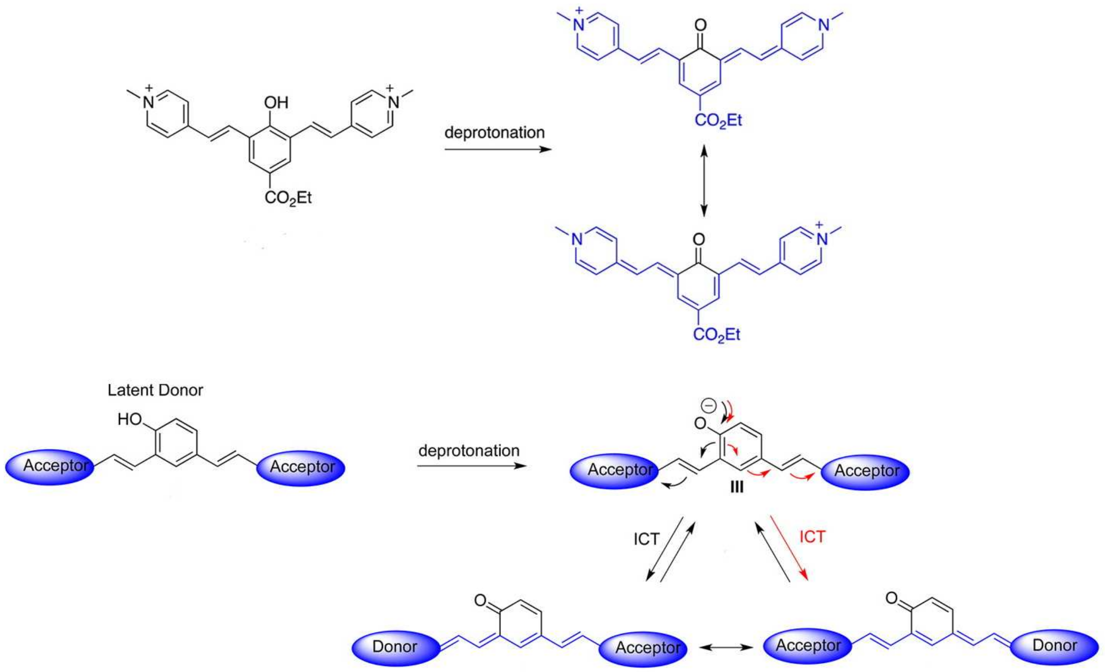

Fig. 3.13: Deprotonation of QCy9 to form an extended π-electron conjugation between the two picolinium acceptors.

are attached: two cyanine dipicolinium groups at the ortho position to the phenol, and a carboxy-ether group at the para position. All these substituents are strong electron-withdrawing groups, and thus significantly increase the photoacidity of the phenol, which is a rather weak photoacid. In practice, the phenol latent donor, in conjugation with two acceptors, can be turned on upon formation of a phenolate ion. As it is illustrated in Figure 3.13, the intramolecular charge transfer (ICT) from the phenolate donor to one of the two acceptor moieties forms a new push-pull conjugated chromophore between the former two acceptors. The newly formed push-pull structural element has a larger π-system than that of the original donor-acceptor π-system, leading to fluorescence in longer wavelengths, in the NIR region.

The QCy9 emission spectrum in aqueous solution shows a dual-band emission arising from the photoprotolytic reaction. A rather weak short-wavelength emission band, at about 480 nm is attributed to the protonated form, whereas a high intensity band peaked at about 680 nm is attributed to the RO^- form of QCy9. Moreover the fluorescence up-conversion signals, measured for QCy9 at 680 nm, shows two component: a fast rise time component, with large amplitude and a time constant of about 100 fs, and a second one with smaller amplitude and a time constant of 500 fs. [104] The former is attributed to ESPT toward the aqueous solvent, corresponding to a proton rate constant of $10^{13} s^{-1}$, whereas the latter to the subsequent hopping of the proton to the bulk water.

3.2.1 A preliminar statical description of the ground and excited state reactivity

In order to get a first flavor of the potential energy surface associated with the PT reactions, a constrained potential energy profile following an ad-hoc defined reaction coordinate was computed on the ground and the excited electronic state. More closely, in order to follow the proton transfer from QCy9 to the acceptor water molecule, PT and ESPT reactions were simulated by considering the O-H distance of the hydroxyl group as the reaction coordinate. This distance was scanned every 0.05 Å in the 1.00-1.60 Å range of values, while relaxing all the other degrees of freedom.

We modelled PT and ESPT reactions by considering a solvent molecule as the

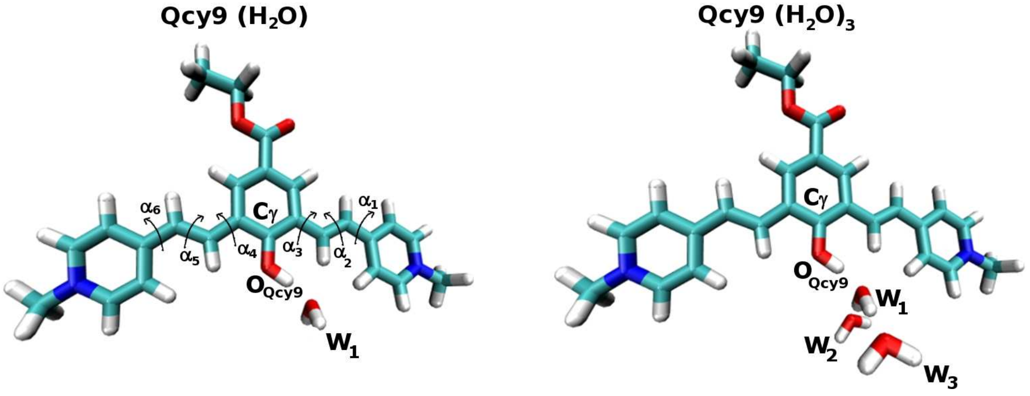

Fig. 3.14: QCy9(H_2O) and QCy9(H_2O)$_3$ clusters optimized in aqueous solution at the electronic ground state. Some useful labels are also provided.

proton acceptor. To investigate the effects of the solvent molecules belonging to the first solvation shell, two representations of the acceptor water microsolvation was evaluated, in which the explicit solvation of the proton accepting water molecule was (QCy9(H_2O)$_3$) or was not included (QCy9(H_2O)), respectively. See Figure 3.14 for the cluster representation.

In both the cases the bulk solvation effects were represented by a Polarizable Continuum Model (PCM). [99,105] Hence the simulated reactions can be generically represented as follows:

$$(Qcy9)_{aq} + H_2O_{aq} \longrightarrow (QCy9^{-})_{aq} + H_3O^{+}_{aq}$$

$$(Qcy9)_{aq} + 3(H_2O)_{aq} \longrightarrow (QCy9^{-})_{aq} + (H_3O^{+}(H_2O)_2)_{aq}$$

GS and the ES potential energy profiles are given in figure 3.15 for both the QCy9(H_2O) and the QCy9(H_2O)$_3$ cluster in aqueous solution. From figure 3.15 it is clear that the reaction does not occur when the QCy9(H_2O) cluster in aqueous

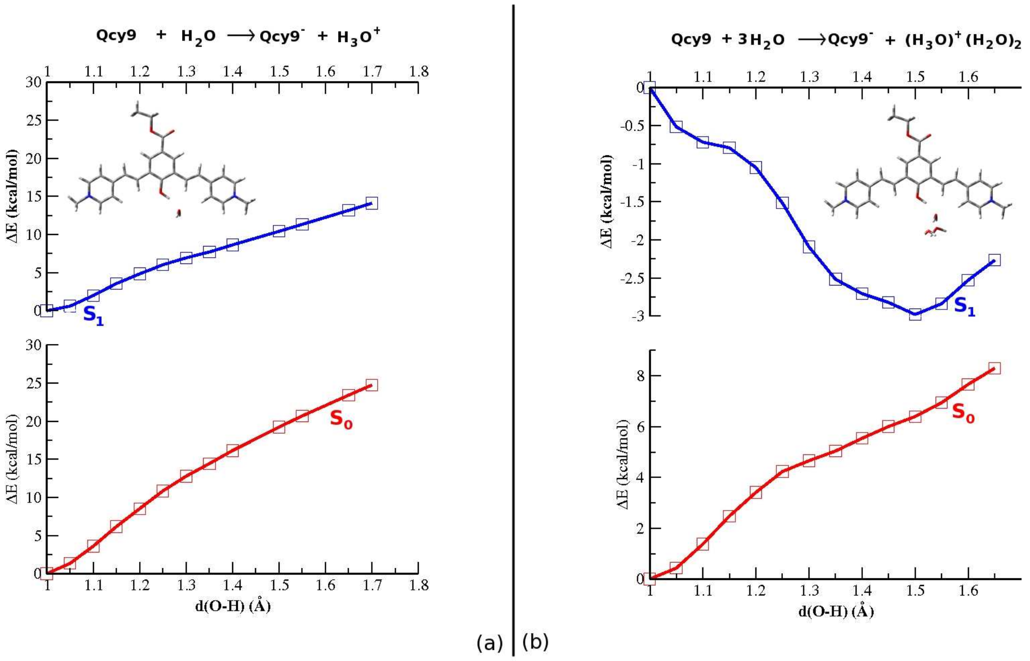

Fig. 3.15: (a) GS (red) and ES (blue) energy profiles calculated for the reaction QCy9 + H_2O $\longrightarrow$ QCy9$^-$ + H_3O^+ in aqueous solution; (b) GS (red) and ES (blue) energy profiles calculated for the reaction QCy9 + 3 H_2O $\longrightarrow$ QCy9$^-$ + $H_3O^+(H_2O)_2$ in aqueous solution.

solution is chosen to represent the reactans, in neither electronic state. The QCy9$^-$ + H_3O^+ adduct is not stabilized into a product, and it remains at about 10 and 20 kcal/mol higher in energy with respect to the reactants in the S_0 and S_1 state, respectively.

A completely different behaviour was obtained in the case of the QCy9$(H_2O)_3$ cluster, which includes an explicit solvation of the proton accepting molecule. In this case the reactive event does not spontaneously occur at S_0, with no stabilization of the ion pair, lying 8 kcal/mol above the reactants. On the contrary, at the excited state the reaction occurs barrierless, with the ESPT product stabilized of about 3 kcal/mol with respect to the reactants. Hence, the microsolvation of the proton

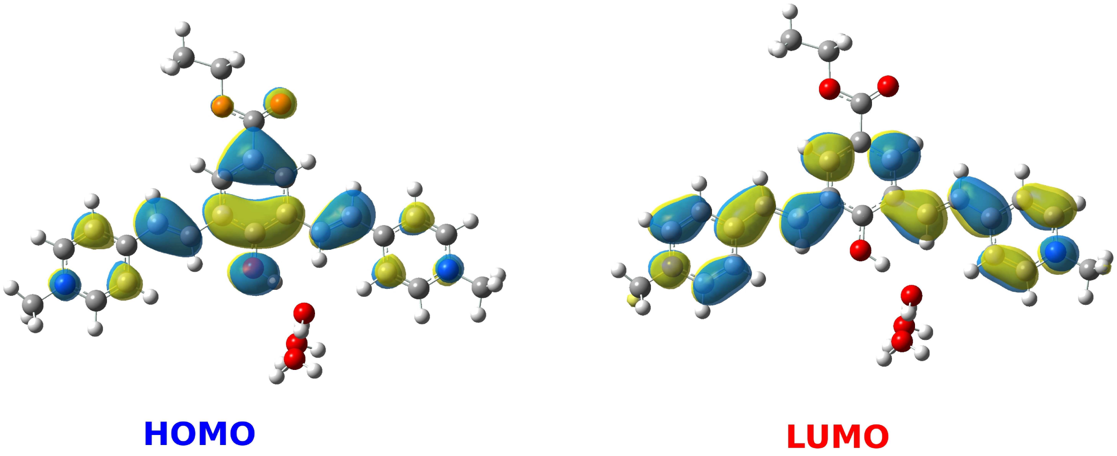

Fig. 3.16: HOMO and LUMO contour plots computed for QCy9 in the ground state minimum energy structures.

acceptor water molecule drastically affects the excited state reactivity.

The electronic excitation to the S_1 state of the QCy9 molecule is bright and shows a strong HOMO-LUMO character. In particular, as it can be also inferred by inspection of the molecular orbital contours (see figure 3.16), the excitation entails a marked CT from the phenol oxygen to the picolinium moiety which in turn drives the PT event on the ES PES.

Moreover the reaction proceeds decreasing the charge transfer extent of the vertical excitation along the reaction coordinate, being the D_{CT} value 1.65 Å and 0.5 Å respectively for $QCy9(H_2O)_3$ and $QCy9^-(H_3O^+)(H_2O)_2$. This feature was already noticed for the ultrafast ESPT involving the coumarin dye of the previous section. [20, 87]

The main structural parameters optimized along the PT profiles are reported as Table 3.3.

Table 3.3: Main structural parameters (Å) computed at S_1 for the ESPT reaction QCy9 + 3 H_2O $\longrightarrow$ $QCy9^-$ + $H_3O^+(H_2O)_2$.

O_{QCy9}-H	O_{QCy9}-O_{W1}	C_γ-O_{QCy9}	O_{W1}-O_{W2}	O_{W1}-O_{W3}
1.000	2.526	1.299	2.714	2.703
1.100	2.418	1.283	2.650	2.654
1.200	2.379	1.270	2.605	2.600
1.300	2.394	1.261	2.568	2.569
1.400	2.449	1.256	2.545	2.547
1.500	2.523	1.253	2.524	2.526
1.600	2.606	1.250	2.515	2.518

For the S_1 energy profile of the QCy9$(H_2O)_3$ system in aqueous solution, the acceptor water gradually approaches the O_{QCy9} atom with the increases of the O_{QCy9}-H distance, adopting an intermediate arrangement with the other two water molecules that is similar to a zundel-like cation. After binding the proton, the acceptor water (now hydronium) moves away from the $QCy9^-$ molecules, while its microsolvation evolves into an eigen-like configuration. The O_{QCy9}-O_{W1} distance decreases reaching a minimum value of 2.38 Å when the O_{QCy9}-H distance is 1.25 Å, in correspondence of the transition state region. After that, a release of the O_{QCy9}-O_{W1} distance is observed. During the protonation the other two water molecules approach progressively the new formed hydronium, decreasing the O_{W1}-O_{W2} and O_{W1}-O_{W3} distances, inducing in such a way a stabilizing effect. In Table 3.4 we report important structural parameters optimized in aqueous solution for the QCy9$(H_2O)_3$ cluster at both the S_0 and S_1 states, and for the $QCy9^-(H_3O^+)(H_2O)_2$ photoproduct at S_1. Labels are provided in figure 3.14. One of the main effects of the electronic excitation of the QCy9$(H_2O)_3$ system is the increasing of the hydrogen bond strength involving

Table 3.4: Main structural parameters (Å and degrees) optimized in aqueous solution for the QCy9(H_2O)$_3$ cluster at both the S_0 and S_1 states, and for the QCy9$^-$(H_3O^+)(H_2O)$_2$ photoproduct at S_1. See figure 3.14 for labels.

	QCy9(H_2O)$_3$ (S_0)	QCy9(H_2O)$_3$ (S_1)	QCy9$^-$(H_3O^+(H_2O)$_2$)(S_1)
O_{QCy9}-O_{W1}	2.631	2.526	2.523
C_γ-O_{QCy9}	1.336	1.299	1.253
α_1	0.73	-1.15	0.61
α_2	179.25	178.69	178.86
α_3	171.57	174.32	-178.44
α_4	-179.48	179.57	179.72
α_5	179.73	175.87	-178.68
α_6	-1.42	-0.91	1.16

the hydroxyl group and the acceptor water molecule. In fact, the O_{QCy9}-O_{W1} distance decreases of about 0.1 Å when comparing the S_0 and S_1 optimized structures, assuming a value of 2.53 Å at the excited state.

An interesting structural feature regards the relative orientation of the phenol with respect to the picolinium groups. The QCy9$^-$(H_3O^+(H_2O)$_2$) product of the ESPT reaction shows a structure more symmetric with respect to the QCy9(H_2O)$_3$ cluster, with both the picolinium moieties fully coplanar with the phenol group (see α values in Table 3.4). This rearrangement leads to a fully delocalization of the excess electron density on the O_{QCy9} atom. Another noticeable difference between the QCy9(H_2O)$_3$ and the QCy9$^-$(H_3O^+(H_2O)$_2$) forms is the C_γ-O_{QCy9} bond length, which decreases of about 0.05 Å in the proton transfer adduct.

This statical picture of the reaction shows that in the ground state the dominant specie present in water solution is the neutral QCy9, while in the excited state the concentration of the anionic form rises as a consequence of the ESPT reaction.

Moreover the ESPT energy profile of QCy9 accounts for a barrierless process once an explicit solvation is provided for the proton accepting water molecule. In absence of such an explicit representation, the energy values along the profile decrease with respect to the corresponding ones in the ground state, but no product stabilization is obtained.

To disantangle the response of the cybotactic region and its role in the ESPT process, a dinamycal picture is of course mandatory. This will be the aim of the following section.

3.2.2 Sampling of QCy9 in aqueous solution in the ground electronic state

As said, the ESPT is triggered by the excitation of the QCy9 in aqueous solution, when the system is at equilibrium in the ground electronic state. Therefore, the reactant of the phototriggered reaction is one of the possible configurations accessible to the QCy9 and the surrounding solvent on the ground state PES.

Thus, the simulation of the ESPT process from a dynamical point of view, starts with the exploratation of the GS PES through ab initio molecular dynamics simulations, performed with the ADMP approach, [100–103] considering explicitly the solvent coordinate, by embedding the QCy9 photoacid inside a solvent spherical box of 16.5 Å radius (see Figure 3.17) containing 608 water molecules.

The Our N-layered Integrated molecular Orbital + molecular Mechanics (ONIOM) extrapolative scheme [106] was adopted to define the potential energy surface, treating the QCy9 solute at quantum mechanical level (adopting the B3LYP density functional), and the solvent water molecules at molecular mechanics level (adopting the TIP3P water model [107]). In addition, non periodic boundary conditions have been employed using the General Liquid Optimized Boundary (GLOB) model, [92–94] a flexible and effective method to enforce nonperiodic boundary conditions in ab initio dynamics of solute-solvent system.

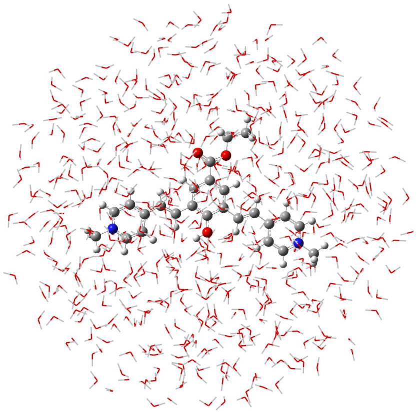

Fig. 3.17: Model of the QCy9 dye in solution.

We sampled the GS PES for a total period of 22 ps, of which the first two have been considered as the equilibration time.

The analysis of the trajectory showed that QCy9 dye acts as hydrogen bond donor for the 95% of the time with four water molecules alternating in the hydrogen bond with the phenolic OH. For about the 63% of the time the QCy9 does not form hydrogen bonds as acceptor. Instead, for about the 35% of time is an acceptor of one hydrogen bond, while for the remaining 2% of the time is acceptor of two hydrogen bonds. In Figure 4.7 we show the radial distribution functions (RDFs) calculated from the ADMP/ONIOM trajectory for the $O_{QCy9} - O_{water}$, the $O_{QCy9} - H_{water}$ and the $H_{QCy9} - O_{water}$ distances, respectively. The $O_{QCy9} - O_{water}$ RDF shows a peak centered at about 2.6 Å and its integral provides a coordination number of 1. This indicates, on average, only one water molecule in the solvation shell of the reactive site, well structured as shown by its representative high peak.

The $O_{QCy9} - H_{water}$ RDF shows a small maximum between about 1.5 Å and 2.7 Å, whose integral restitutes a value of 1, in agreement with the fact that QCy9 acts for the 35% of the time as acceptor of one hydrogen bond. The second peak, centered at about 3.25 Å, accounts for the hydrogen atoms of the proton acceptor water molecule and the second hydrogen of the water molecule involved in the hydrogen bond with the QCy9 oxygen as donor.

The $H_{QCy9} - O_{water}$ RDF is characterized by a first peak between 1.25 and 2.25 Å representing the proton accepting water molecule W_1. Within a distance of about 4.5 Å, we observe a second peak, corresponding to the two water molecules solvating W_1. We also calculated a RDF considering the oxygen of the acceptor water molecule as center, namely $O_{W_1} - O_{water}$, shown in Figure 3.19.

The graph shows a peak between about 2.5 and 3.5 Å, whose integral gives a value of 2. This corresponds to a solvation shell of the proton acceptor water

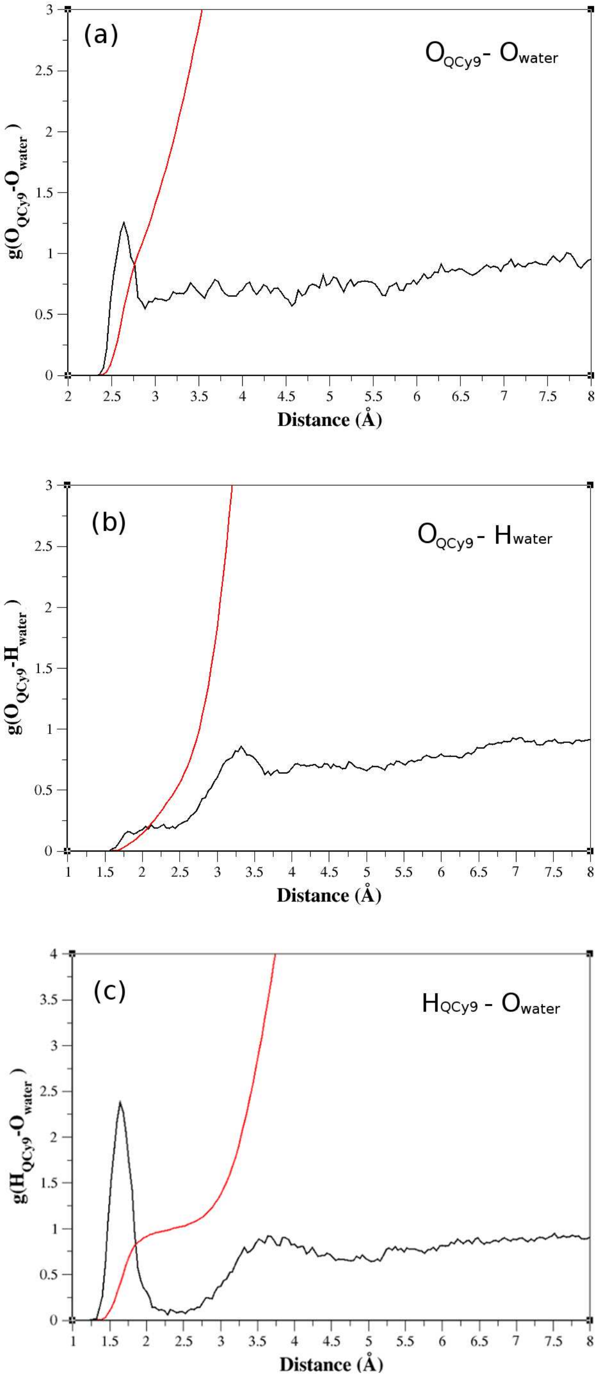

Fig. 3.18: RDFs of phenol oxygen with water oxygen atoms (a), water hydrogen atoms (b) and of phenol hydrogen with water oxygen atoms (c).

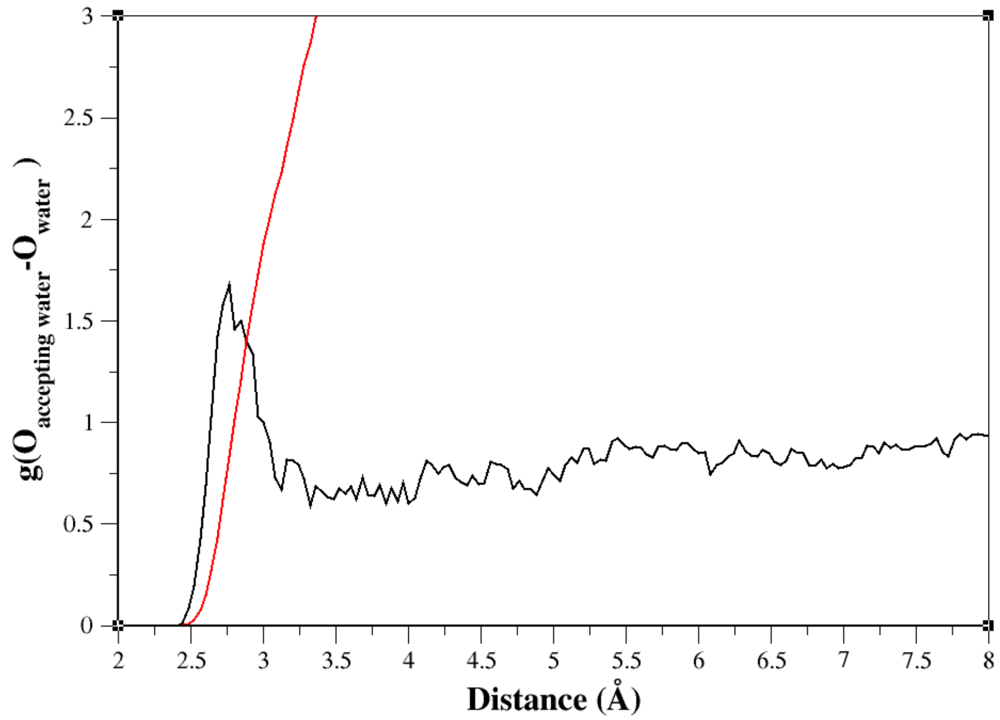

Fig. 3.19: RDF of the proton acceptor water oxygen with water oxygen atoms.

molecule constituted, on average, by two more molecules, confirming the fact that our static representation of the system, namely the $QCy9(H_2O)_3$ cluster, is a good approximation of the dynamical system.

In Figure 3.20 we show the evolution of the phenolic OH distance during the time. Along the trajectory four different water molecules alternate in the solvation of the reactive site, more precisely four different water molecules assume the role of the proton acceptor molecule W_1. In the next, we are going to describe the hydrogen bond interactions of each of such molecules with QCy9.

In the various panels of Figure 3.21 we show the variation in the time of the distance between the phenolic oxygen and the oxygen of the proton acceptor water molecule for the four different water molecules alternating in the solvation of the reactive site. In the same graph, the corresponding hydrogen bond angles are reported.

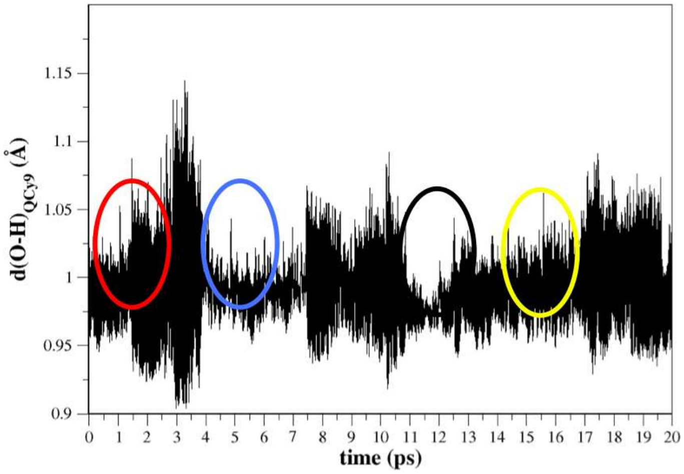

Fig. 3.20: Variation in time of the O-H distance in QCy9 at the ground state. The time intervals 0-2.25 ps (red circle), 4.45-6.45 ps (blue circle), 11-12 ps (black circle) and 15-17 ps (yellow circle) in which the Fourier Transform was performed, are also shown.

The first water molecule (see panel (I) and (II) of Fig. 3.21) persists in proximity of the phenol group for a brief period, of about 2.2 ps, during which the $O_{QCy9} - O_{W_1}$ distance has an average value of 2.68 Å and the corresponding hydrogen bond angle assumes an average value of 15.26°. During the same time the QCy9 O-H distance is characterized by an increase in amplitude that reaches its maximum at about 3 ps, when a second water molecule approaches the reactive site. If we analyze the QCy9 O-H distance in the frequency domain through a Fourier transform we notice that the stretching mode of the O-H group passes from 3424 cm^{-1} during the first 2.2 ps (the lifetime of the first hydrogen bond with W_1), to 3327 cm^{-1} during the water-water exchange period.

In panels (III) and (IV) of Fig. 3.21 we show the corresponding graphs for the water molecule that substitutes the first one in the solvation of the reactive site.

The second water approaches the reactive site with a better orientation with respect to the first one, giving a stronger interaction, characterized by a $O_{QCy9} - O_{W1}$ distance with an average value of 2.65 Å and an average hydrogen bond angle of 10.96°. In the frequency domain we can estimate that during the lifetime of this second hydrogen bond the O-H stretching is characterized by a frequency of 3417 cm^{-1}.

In the last 10 ps of the sampling two other water molecules alternate in establishing an interaction with the QCy9 OH group, the first one for a brief period, while the second one persists until the end of the sampling time, as shown in panels V and VII of Fig. 3.21, respectively. In the 10.6-12.5 ps period we have an average $O_{QCy9} - O_{W_1}$ distance of 3.02 Å, while the average value of the hydrogen bond angle is of 39.76°. The QCy9 O-H stretching frequency has a value of 3322 cm^{-1} during the second water-water exchange and then it is blue shifted to a value of 3620 cm^{-1}. In the remaining time period the $O_{QCy9} - O_{W_1}$ distance has an average value of 2.64 Å, while the average hydrogen bond angle is of 11.77°.

Also here, during the third water-water exchange, the OH stretching frequency is 3328 cm^{-1}, while a subsequent blue shift leads to 3353 cm^{-1}.

In Figure 3.22 we report the Fourier Trasforms of the $(O - H)_{QCy9}$ distance during the time intervals discussed above.

Observing the graph, we have a description of how the strength of the QCy9 O-H bond is influenced instantaneously by the hydrogen bond. Indeed a stronger interaction is characterized by a red shifted peak, because of the decreased stretching force constant of the phenolic OH involved in the hydrogen bond. Confirming the results about the calculated O-O average distances and the average hydrogen bond angles, the fourth W_1 forms the strongest interaction, described by a red shifted peak (yellow curve), while the weakest interaction involves the third W_1, as shown by the corresponding blue shifted band (black curve).

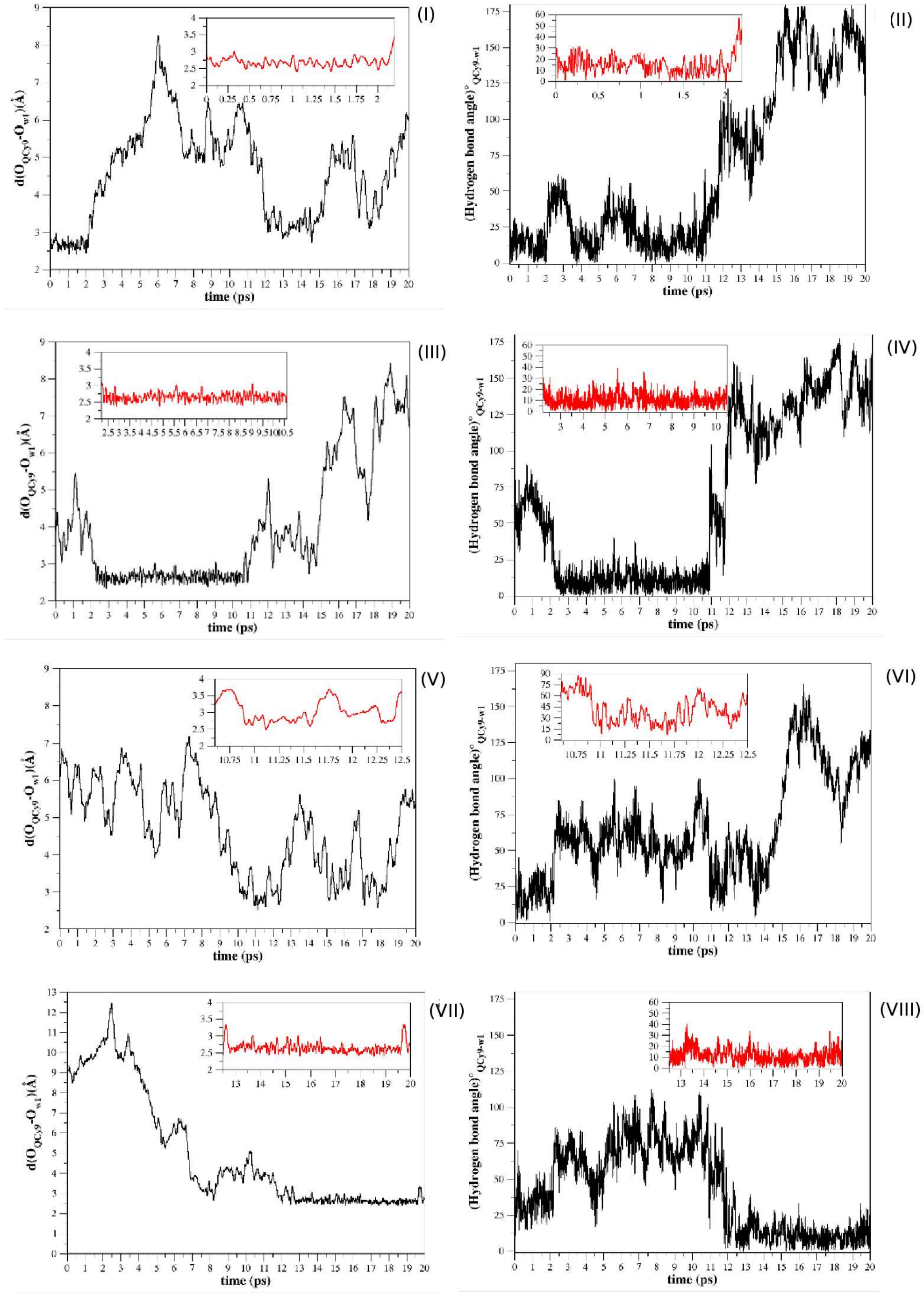

Fig. 3.21: $O_{QCy9} - O_{W_1}$ distance and QCy9-W$_1$ angles for the four water molecule assuming the role of proton accepting molecule W$_1$. Panels I and II refer to the water molecule solvating the QCy9 hydroxyl group in the 0-2.2 ps interval. Panels III and IV refer to the water molecule solvating the QCy9 hydroxyl group in the 2.2-10.6 ps interval. Panels V and VI refer to the water molecule solvating the QCy9 hydroxyl group in the 10.6-12.5 ps interval. Panels VII and VIII refer to the water molecule solvating the QCy9 hydroxyl group in the 12.5-20 ps interval.

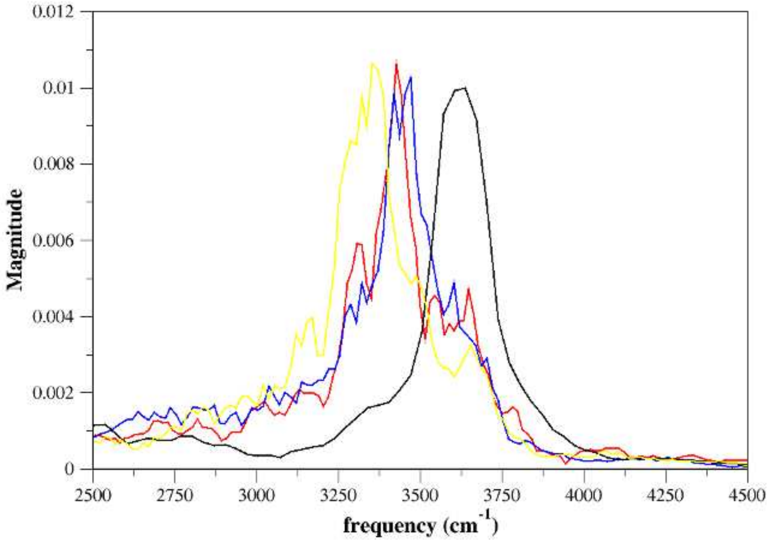

Fig. 3.22: Fourier Transform of the QCy9 O-H distance performed in the 0-2.25 ps (red curve), 4.45-6.45 ps (blue curve), 11-12 ps (black curve) and 15-17 ps (yellow curve) time intervals.

3.2.3 Sampling of QCy9 in aqueous solution in the electronic excited state

Starting from the ground state configurational space, an excited state trajectory was collected through a Born-Oppenheimer molecular dynamics simulation, in order to simulate the relaxation of the system after the photoexcitation. More closely, we extracted a point along the ground state trajectory as starting configuration for the excited state molecular dynamics. This point was chosen in order to be representative, on average, of the microsolvation of the OH group at the ground state, indeed it is characterized by a $(C-O)_{QCy9}$ distance of 1.36 Å, a $O_{QCy9} - O_{accepting-water}$ distance of 2.65 Å, while the QCy9 structure is sufficiently planar in order to allow a good delocalization of the electronic density over the entire molecule. From here, we collected an excited state trajectory for a total period of 500 fs using the TD-CAM-B3LYP/6-31+G(d,p)/AMBER level of theory, including three water molecules in the QM layer, in order to allow, and possibly follow, the proton transfer event. During the simulation, it was possible to sample a well-defined singlet excited state, even if the bright nature of this state is loosen during the sampling, because of a distortion of the QCy9 structure that prevents a full delocalization of the electronic density.

In Figure 3.23 we show the variation of the QCy9 O-H and $H_{QCy9} - O_{W1}$ distances. Between about 125 fs and 225 fs, the QCy9 O-H distance reaches a value of about

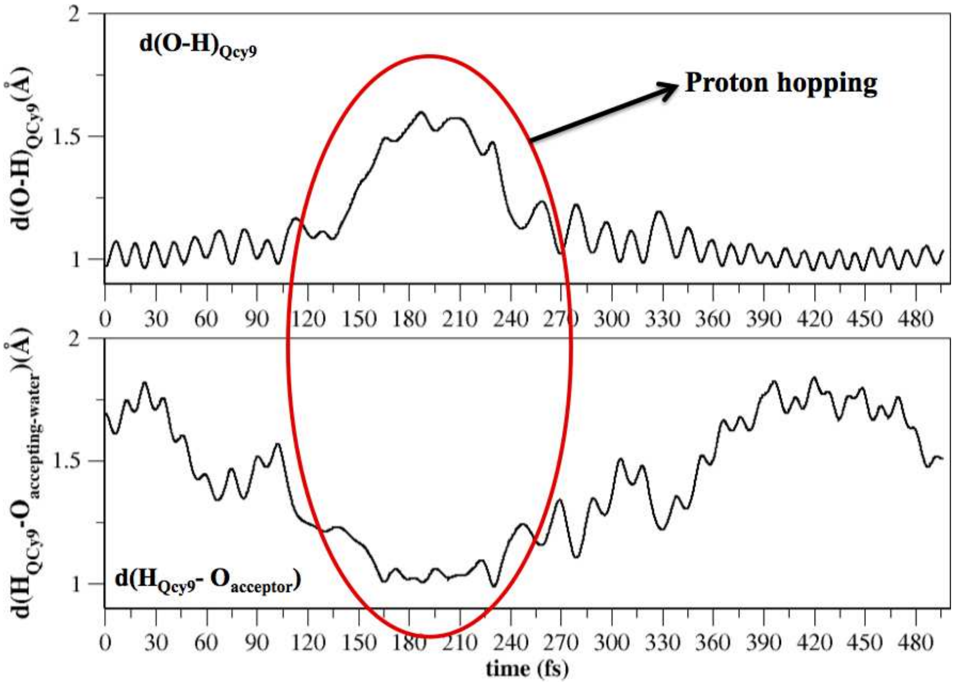

Fig. 3.23: $(O - H)_{QCy9}$ (a) and $H_{QCy9} - O_{W1}$ distances during the BOMD trajectory in the excited state.

1.6 Å, while the donor and the acceptor molecules approach each other up to a value of the $H_{QCy9} - O_{W1}$ distance of about 1 Å. This approaching allows for a proton hopping from one oxygen to the other. Figure 3.24 shows the corresponding variation of the hydrogen bond angle, demonstrating that during the 125-225 fs period the interaction is optimized, reaching a value of about 4°. To describe the role in the reactive event of the two additional water molecules solvating W_1 (labeled as W_2 and W_3, respectively), we show in Figure 3.25, the $H_{W1} - O_{W2/W3}$ and the $O_{W1} - O_{W2/W3}$ distances.

With respect to the reactive event, we can describe two different behaviors for the two water molecules of the cluster. The first one, namely W_2, approaches W_1 before the reactive event, so it accompanies the proton hopping through a partial sharing of a W_1 hydrogen. The second one, W_3, approaches the proton accepting water with some delay with respect to W_2, in order to stabilize the hydronium ion

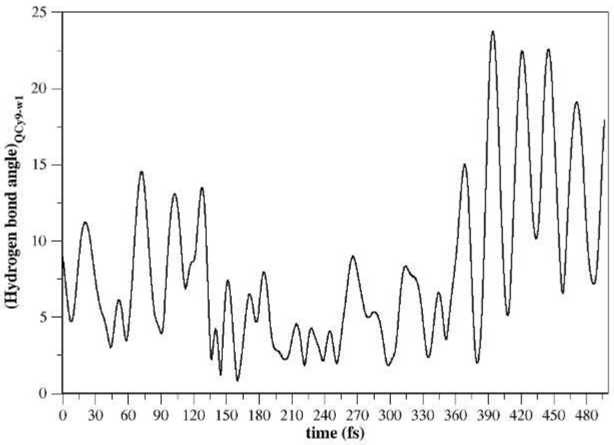

Fig. 3.24: Hydrogen bond angle between the donor and the acceptor molecules along the excited state trajectory.

produced by the proton hopping. Inspite of the poor statics, works are currently in progress in this direction, some important insights on the ESPT mechanism can be inferred from the behavior described above. Indeed, the analysis of correlation motions involving heavy atoms in proximity of the reaction site confirms that proton hoppings between the donor and the acceptor molecules are actually assisted by oscillations of solvent molecules belonging to the first and second solvation shell of the proton accepting water molecule. Some comments are in order when comparing these results to the experimental evidences. The PT time constant is estimated to be equal to 100 fs in the excited state, well shorter than the average solvation correlation function. This time is compatible with the time constant of the acceptor-donor oxygen intermolecular vibration (200 cm^{-1}). This datum suggested the hypothesis

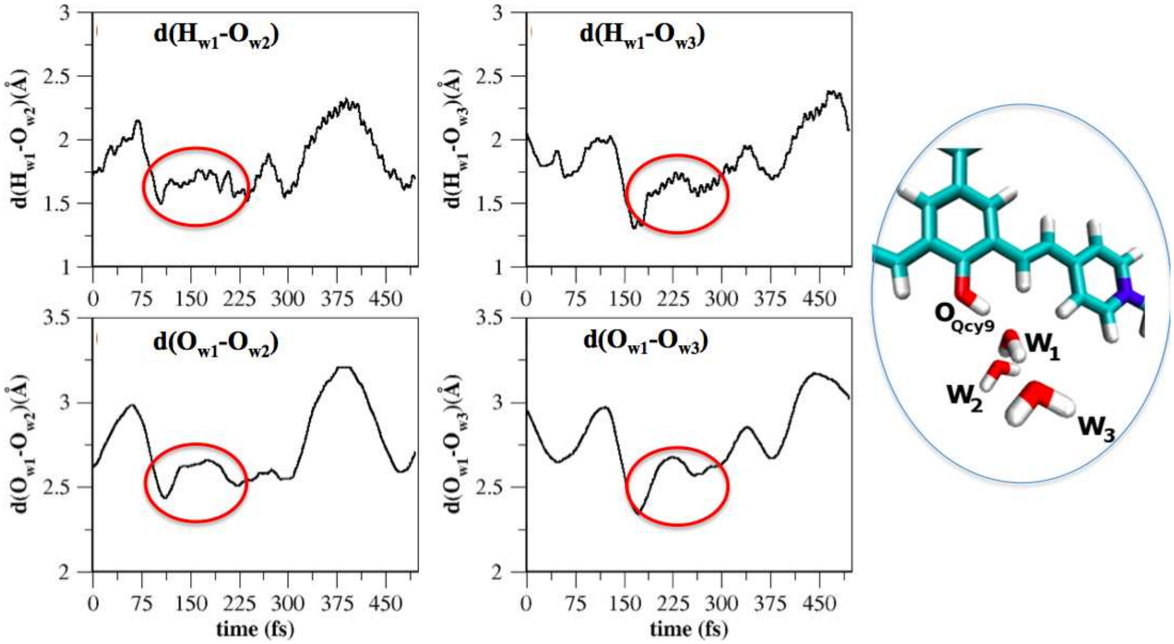

Fig. 3.25: Distances evolution during the excited state trajectory involving W$_1$, W$_2$ and W$_3$ water molecules: (a) $H_{W1} - O_{W2}$; (b) $H_{W1} - O_{W3}$; (c) $O_{W1} - O_{W2}$; (d) $O_{W1} - O_{W3}$.

that the rate determining step is given by the relative oscillations of the acid and the acceptor molecule. Our results are not in contrast with this assumption, rather they refine it by suggesting that hydrogen bonds collective stretching modes, in particular those involved in the first solvation shell of the accepting molecule, which occur on the same order of magnitude than the acceptor-donor intermolecular vibration (180 cm^{-1}), are actually responsible of the rate determining step in this superphotoacid. Therefore, even for strongest photoacids, with reaction rates as rapid as to circumvent the control of the whole solvation dynamics, the ESPT is assisted and modulated by low frequency modes of solvent molecules in proximity of the proton acceptor molecule.

In summary, these two pilot applications shown clearly demonstrated that AIMD based on TD-DFT and robust solvent models appears to be a feasible and reliable way to represent both the electronical, nuclear and solute/solvent rearrangement ruling phototriggered process in condensed phase.

Implicit solvent model allows to follow the formation of the proton transfer adduct catching the features of the electronic rearrangement which drives the reaction. Nevertheless to achieve the full exploration of the product region during the simulation an explicit solvent representation is mandatory. Hybrid implicit/explicit model of the solvent represents an appealing choice in this sense.

Chapter 4

Opening the Pandora's box of microsolvation effects on proton coupled electron transfer reactions: the case of oligo-peptides in water solution

In the last chapter surrounding medium effects and the response of the cybotatic region turned out to be critical parameters affecting the energetic and mechanism of excited state proton transfer reactions. Furthermore, solvent molecules (especially water) can also influence charge transfer processes by affecting the electron pathway or the electronic coupling between the electronic states involved in the reaction. [108,109] In the past decade, [108–111] several examples appeared in literature suggesting that water plays an important role mediating long range electron transfer (ET) as well as by controlling activation free energies. More closely the intervening water can link the electron donor and acceptor via hydrogen bonds which may eventually serve as the proton pathway and also enhance the overlap between the electron donor and acceptor orbitals acting as the electron pathway. [108] Furthermore the dynamical organization of the intervening solvent is critical to the formation of the most efficient ET configuration. [110] These effects are of paramount importance in proton coupled electron transfer processes where they can influence the degree of adiabaticity between electronic and nuclear configurations. As matter of fact PCET reactions may be electronically adiabatic or nonadiabatic, in the sense that the electrons can or cannot respond instantaneously to the nuclei, respectively. [45] The energy difference between the ground and excited adiabatic electronic states during the reaction controls the degree of electronic nonadiabaticity. [45] Indeed, if this energy difference is much larger than the thermal energy the reaction will be electronically adiabatic evolving on only the ground electronic state, since the excited electronic states are not thermally accessible. Vice versa when this energy difference is smaller than the thermal energy, the reaction is electronically nonadiabatic, involving the coupling with excited electronic states, since these states are now thermally accessible. According to the adiabaticity extent, the proper kinetic model must be applied. Understanding how and if the solvent can affect it, becomes, thus, extremely important. The theoretical investigation presented in this chapter aims to provide significant insights in this context. More closely we showed how the microsolvation structure affects the energy of electronic states involved in the PCET process, as well as the electronic coupling among them. Of course, to single out fine details or specific aspects tuning these coupled reactions, the use of simpler models provides a more convenient approach. For this reason we focused on a well defined model peptide, recently developed by Giese and coworkers [21,22,112,113] to measure the charge transfer efficiency in biological systems. In details, we considered, the PCET involving the radical cation $Tyrosine-Glycine-Glycine-Glycine-2,4,6-Trimethoxyphenylalanine$ ($YGGGF^{\bullet+}_{TRM}$), and one molecule of the aqueous solvent. $YGGGF^{\bullet+}_{TRM}$ is a radical cation formed by the loss of an electron from 2,4,6-trimethoxyphenylalanine of the parent molecule. On turn, this radical is the reactant for a PCET reaction by which an electron transfer takes place between tyrosine and trimethoxyphenylalanine, and a coupled proton transfer involves the tyrosine hydroxyl group (PT donor) and a solvent water molecule (PT acceptor). In summary, the simulated reaction can be represented as follow:

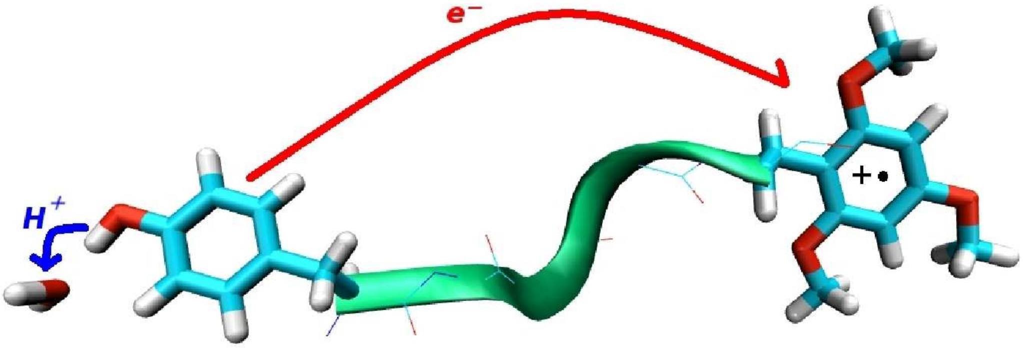

Fig. 4.1: Graphical sketch of the analysed PCET reaction.

$$\mathrm{YGGGF}^{\bullet+}_{TRM(aq)} + (\mathrm{H_2O})_{(aq)} \longrightarrow \mathrm{Y^{\bullet}GGGF}_{TRM(aq)} + \mathrm{H_3O^+}_{(aq)}$$

where aq indicates the study in the aqueous solvent represented by a polarizable continuum model. This reaction is well characterized from an experimental point of view, [21, 22, 112, 113] showing a kinetic constant for the ET reaction between tyrosine and 2,4,6-trimethoxyphenylalanine of about 3.0 x10^7 s^{-1}. [113]

In order to study the microsolvation effects of the tyrosine (PCET donor residue) on the PCET process, we considered several peptide - water clusters, including three (α cluster), four (β cluster), five (γ cluster) and six (δ cluster) water molecules, respectively. The four clusters build up to represent different tyrosine microsolvations are reported in Fig. 4.2. In the α cluster (fig. 4.2(a)) the tyrosine microsolvation is represented by three water molecules arranged in an *eigen*-like structure. By adding further water molecules to complete the first solvation sphere of the acceptor water,the β cluster is obtained while saturating the tyrosine solvation sites give us the δ and γ arrangements.

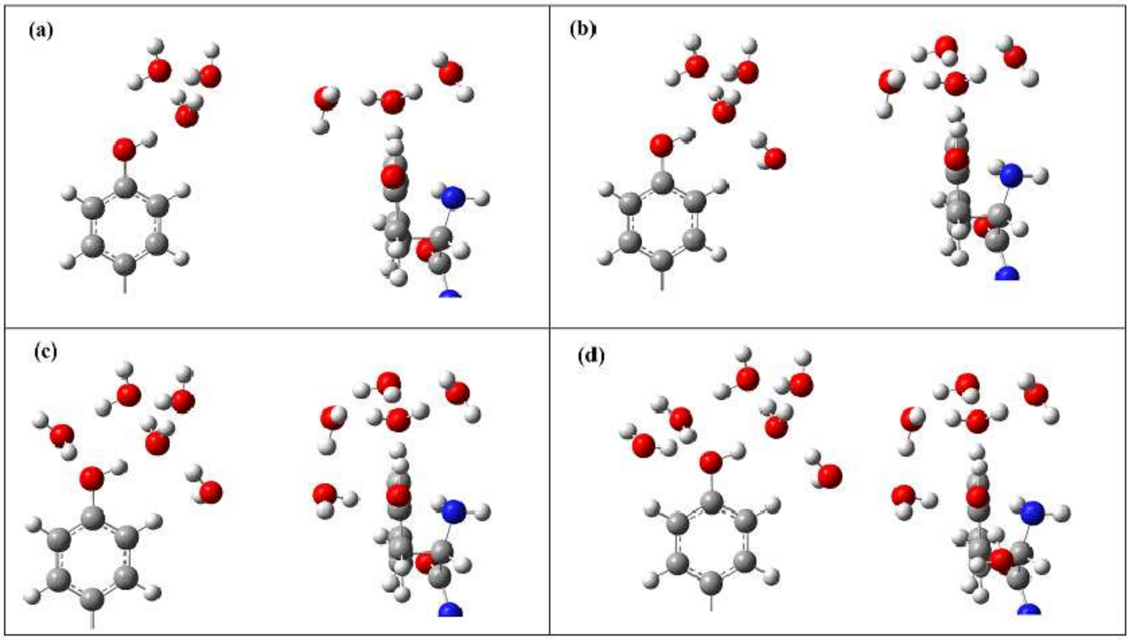

Fig. 4.2: $[YGGGF_{TRM}(H_2O)_n]^{\bullet+}$ clusters:(a) cluster α; (b) cluster β;(c) cluster γ; (d) cluster δ.

Note that, the tyrosine is solvated only by the proton acceptor water, in the α and β clusters, while one and two water molecules act as hydrogen bonds donor (HBD) in the γ and δ clusters, respectively. This allowed to effectively assess the impact of the microsolvation on the PCET reaction.

The statistic weight of these peptide-water clusters has been examined through an ONIOM/ADMP molecular dynamic simulation enforcing non periodic boundary condition. [114]

4.1 Modeling of the PCET reaction

A constrained potential energy profile following an *ad-hoc* defined reaction coordinate was computed on α, β, γ and δ clusters, in order to follow the proton transfer from tyrosine oxygen (O_{tyr}). Thus the distance between the tyrosine oxygen (O_{tyr}) and its proton ($O_{tyr} - H$ distance) represents the reaction coordinate of PCET reaction. The distance was scanned in the 1.00-1.60 Å range while relaxing all other degrees of freedom, and maintaining a constraint on the angles ϕ and ψ of the polypeptide backbone ($\phi = -75°$ and $\psi = 145°$) to preserve the Polyproline II (PPII) helix conformation, which has been experimentally observed. [115]

Former values of the $O_{tyr} - H$ distance correspond to the PT reactant state in which the proton is bound to the tyrosine oxygen, while the latter values correspond to the PT product state where the hydronium ion is formed. In order to follow the ET process, we monitored the Mulliken spin densities (SD) on each residue of the peptide along the PT coordinates. According to this assumption, the ET reactant state corresponds to a SD=1 on the trimethoxyphenylalanine residue (radical form) and SD=0 on the tyrosine (closed shell form). On the contrary, the ET product is characterized by a SD=0 on the trymethoxyphenylalanine residue (closed shell form) and SD=1 for the tyrosil radical.

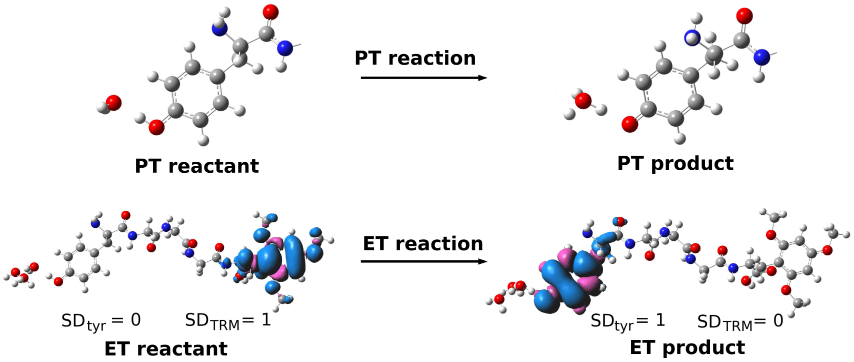

Fig. 4.3: Modeling of the PCET reaction. The O_{tyr}-H distance represents the nuclear coordinate of whole the PCET reaction. To follow the Electron Transfer(ET) event the Mulliken spin densities on each residue have been evaluated along the PT coordinate.

To correctly simulate the reactive event, the proper representation of the radical species involved is of course mandatory. Moreover the energetics and kinetics of proton coupled electron moving is strongly influenced by the way in which DFT features describe the evolving electronic density. Very recently, we analyzed in details the efficiency of the various density functionals in describing the PCET processes in terms of reliability and feasibility. [116] Our results showed that when the solvent is considered through implicit continuum models, i.e. the polarizable continuum method, the subtle balance between the Hartree Fock exchange percentage of the density functionals and the solvent field must be carefully taken into account. More closely considering an explicit solvation and post HF methods as reference for the condensed phase, Global Hybrid (i.e. B3LYP,PBE0) functionals in conjunction with PCM model are those with the better behavior. In order to achieve the correct localization of the unpaired electron along the reaction path, we modeled the PCET process in condensed phase by employing PBE0 [117] density functional combined with PCM for the solvent bulk effects.

4.2 The effects of solvation

4.2.1 A statical picture

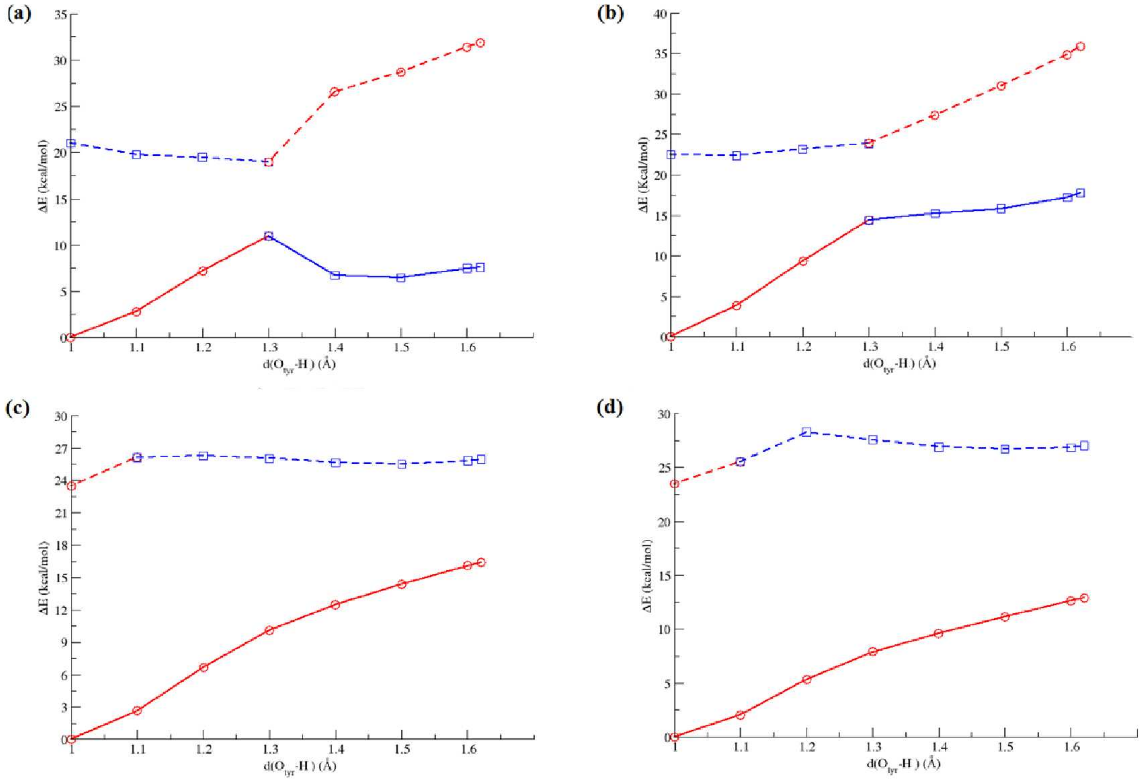

Fig. 4.4: Energetics profiles:(a)cluster α; (b)cluster β;(c) cluster γ; (d) cluster δ. Solid and dashed lines represent the ground state and first excited state adiabatic potential energy surface respectively. In the red and blue lines the radical is respectively localized on trimethoxyphenylalanine or tyosine residue.

In Figure 4.4 energy profiles along the PT coordinate are reported for clusters α, β, γ, and δ. In order to indicate the diabatic state of reference, red lines refer to a situation in which the unpaired electron can be localized on the trimethoxyphenylalanine residue, while blue ones refer to situations in which the radical can be attributed to the tyrosine residue. From inspection of structural parameters (see Table 4.1 and Figure 4.5 for labels) we note that in both the α and δ clusters the acceptor water (W_1) gradually approaches to O_{tyr} at increasing of the distance $O_{tyr} - H$, producing the formation of a zundel like cation as intermediate. After accepting the proton, W_1 moves away from the tyrosine returning again in an eigen like configuration.

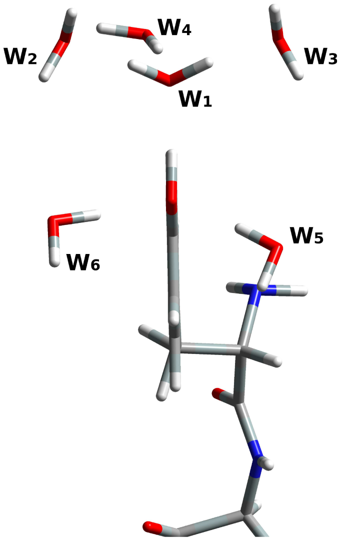

Fig. 4.5: Labels for the water molecules of the δ cluster. The same labels are also used for α, β and γ cluster.

Moreover, during the PT molecules W_2 and W_3 approach progressively W_1 of about 0.2 Å in both the α and δ cases, stabilizing the hydroinium ion. In the δ cluster case W_4 moves away from molecule W_1 of approximately 0.14 Å during the deprotonation, while molecules W_5 and W_6 approach closer to O_{tyr}, the former of about 0.18 Å and the latter of about 0.12 Å. These hydrogen bond donors stabilize the charge density developed on the tyrosine oxygen during the deprotonation process. Finally from the structures analysis we can observe an almost negligible variation of the side chain dihedral angles χ_1 and χ_2 of the tyrosine, in both the clusters α and δ.

α cluster

d($O_{tyr} - H$)	d($O_{W1} - O_{tyr}$)	d($O_{W1} - H$)	d($O_{W1} - O_{W2}$)	d($O_{W1} - O_{W3}$)
1.003	2.600	1.596	2.733	2.730
1.103	2.528	1.426	2.699	2.697
1.203	2.479	1.276	2.655	2.652
1.303	2.474	1.172	2.615	2.613
1.403	2.463	1.061	2.546	2.542
1.503	2.534	1.031	2.522	2.521
1.603	2.615	1.012	2.517	2.511
1.623	2.632	1.009	2.512	2.511

δ cluster

d($O_{tyr} - H$)	d($O_{W1} - O_{tyr}$)	d($O_{W1} - H$)	d($O_{W1} - O_{W2}$)	d($O_{W1} - O_{W3}$)	d($O_{tyr} - O_{W5}$)	d($O_{tyr} - O_{W6}$)
1.001	2.578	1.585	2.692	2.636	2.777	2.836
1.101	2.503	1.410	2.653	2.600	2.741	2.814
1.201	2.451	1.258	2.613	2.555	2.702	2.783
1.301	2.449	1.115	2.589	2.504	2.668	2.757
1.401	2.485	1.092	2.566	2.471	2.642	2.738
1.501	2.543	1.053	2.555	2.442	2.621	2.726
1.601	2.614	1.027	2.555	2.415	2.598	2.718
1.621	2.628	1.022	2.558	2.408	2.590	2.717

Table 4.1: Geometrical parameters optimized for α and δ peptide-water clusters at frozen $O_{tyr} - H$ distances and at the PBE0/6-31G(d,p) level of theory. Geometrical parameters of the δ cluster have been also adopted for the β and γ arrangements.

Analysis of the energetic profile of cluster α, reveals that the electron transfer occurs at the ground electronic state. The energy barrier for the process is about 10 kcal/mol, although it could be still lowered to a value of 7.5 kcal/mol including the Zero Point Vibrational Energy.

As it can be inferred from Figure 4.4(a) the two adiabatic PESs are quite separated with a minimum energy difference of 8 kcal/mol (0.347 eV) occurring at the maximum of the ground state PES.

Analysis of spin densities localization revealed that the two electronic states (adiabatic states) are well described in terms of two diabatic ones. One of these, that is to say the reactant one, corresponds to the situation in which the electron and proton are located on the tyrosine residue. The other one (product state), represents the situation where the electron is on the trimethoxy residue, and the proton is transferred on the acceptor water.

This picture remains unchanged in the case of the β cluster (see Figure 4.4(b)).

Regarding γ and δ clusters, it is worthy to note that within these microsolvation structures the ET event doesn't take place on the ground electronic state.

The analysis of the Mulliken charges integrated for fragments (Figure 4.6), revealed that, when the solvation of tyrosine is represented by the cluster δ, the formation of the phenolate resulted to be stabilized with respect to the phenoxide. As it can be inferred from analysis of Figure 4.6 this situation corresponds to stabilize a zwitterionic state with a net positive charge on trimethoxy residue, a net negative charge on tyrosine one and finally a net positive charge on the hydronium ion.

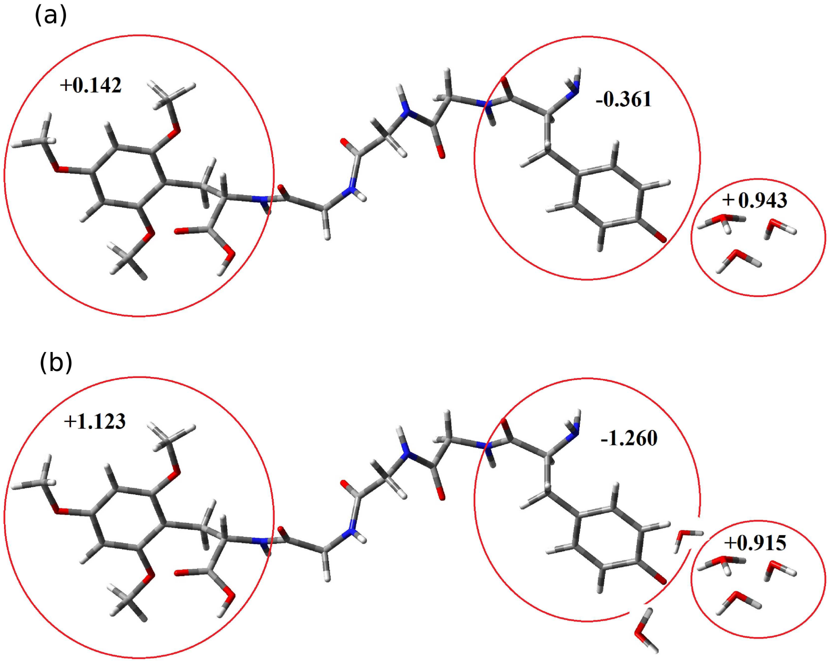

Fig. 4.6: Mulliken charges integrated for fragments for the α (panel (a)) and δ (panel (b)) cluster, in the last point of PCET profile when the hydronium ion is formed.

From this point of view the water molecules solvating as hydrogen bond donor the tyrosine oxygen energetically favor the formation of the ion pair between the tyrosile anion and the hydronium ion on the ground electronic state.

The same picture is achieved, in the case of the γ cluster when one single water molecule acts as HBD to the tyrosine oxygen.

The solvent fluctuations of the first solvation shell around the electron/proton donor can thus drastically influence the nature of the adiabatic state on which the reaction occurs. When the reaction site is not solvated by hydrogen bond donor (cluster α,β) the proton/electron moving occurs on the ground state potential energy surface. The presence at least of one water molecule as hydrogen bond donor (cluster γ,δ) requires the coupling with ES PES to allow the electron transfer event. Of course in condensed phase the solute microsolvation structure dynamically changes with the solvent fluctuations. This means that dynamics fluctuations of the solvation shells can influence the adiabaticy degree of the process. In turn this aspect has to be carefully take into account by kinetical models. In view of this, a dynamical vision of the solvation is mandatory in order to understand what situation among α, β, γ and δ clusters is more representative of the reality.

4.2.2 A dynamical picture

The potential energy surface of the peptide has been explored through ab initio molecular dynamics simulation in order to obtain informations on the tyrosine microsolvation.

Due to the high computational cost of the ONIOM/ADMP simulation [114] required for the target system a preliminary analysis has been conducted on the microsolvation of a phenol molecule. This can be considered representative of the reactant state solvation in which nor the electron nor the proton have been transferred yet. An ab-initio trajectory for a total period of 10 ps solvating the phenol ring inside a spherical box of 13 Å radius containing 304 water molecules. The full QM level (B3LYP/6-31G(d,p)) was adopted for the phenol molecule, whereas the remaining explicit solvent molecules have been described at MM level using the

TIP3P water model . [107] Furthermore, non periodic boundary condition has been employed using a nonperiodic ab initio dynamics model, namely, the general liquid optimized boundary (GLOB). [92–94]

In figure 4.7 $O_{phenol} - O_{water}$ and the $H_{phenol} - O_{water}$ (where O_{phenol} and H_{phenol} are those of phenol hydroxyl group) radial distribution functions (RDF) are shown as calculated from the ADMP/ONIOM trajectory. The $O_{phenol} - O_{water}$ RDF shows a maximum at about 2.5 Å, while the first two peaks of the $O_{phenol} - H_{water}$ RDF are located at about 2.0 Å and 3.3 Å respectively. The $H_{phenol} - O_{water}$ RDF shows a maximum at about 1.6 Å, after which RDF is lowered almost to zero. These results suggest that at standard condition, a proton acceptor water interacts with the proton of the phenol hydroxyl group. Analysis of the trajectory has also showed that for about 22% of the time O_{phenol} doesn't form any hydrogen bond (HB) as acceptor, for about 61% is acceptor of one HB, and for the remaining 17% of the time, it is acceptor of two HB. Instead, the time in which the hydroxyl group acts as HB donor of one water molecules is 99%.

This analysis can provide some indications about the statistical weight of the peptide-water clusters previously examinated. The microsolvation analyzed by MD indicates a distribution for which clusters α, γ and δ are representative of the 20%, 60%, 20%, of the time respectively. It turns, the most representative cluster is the γ one. At this point a specific detail of the experimental setup has to be considered: the reaction was conducted in a mixture acetonitrile-water 3:1. A molecular dynamic

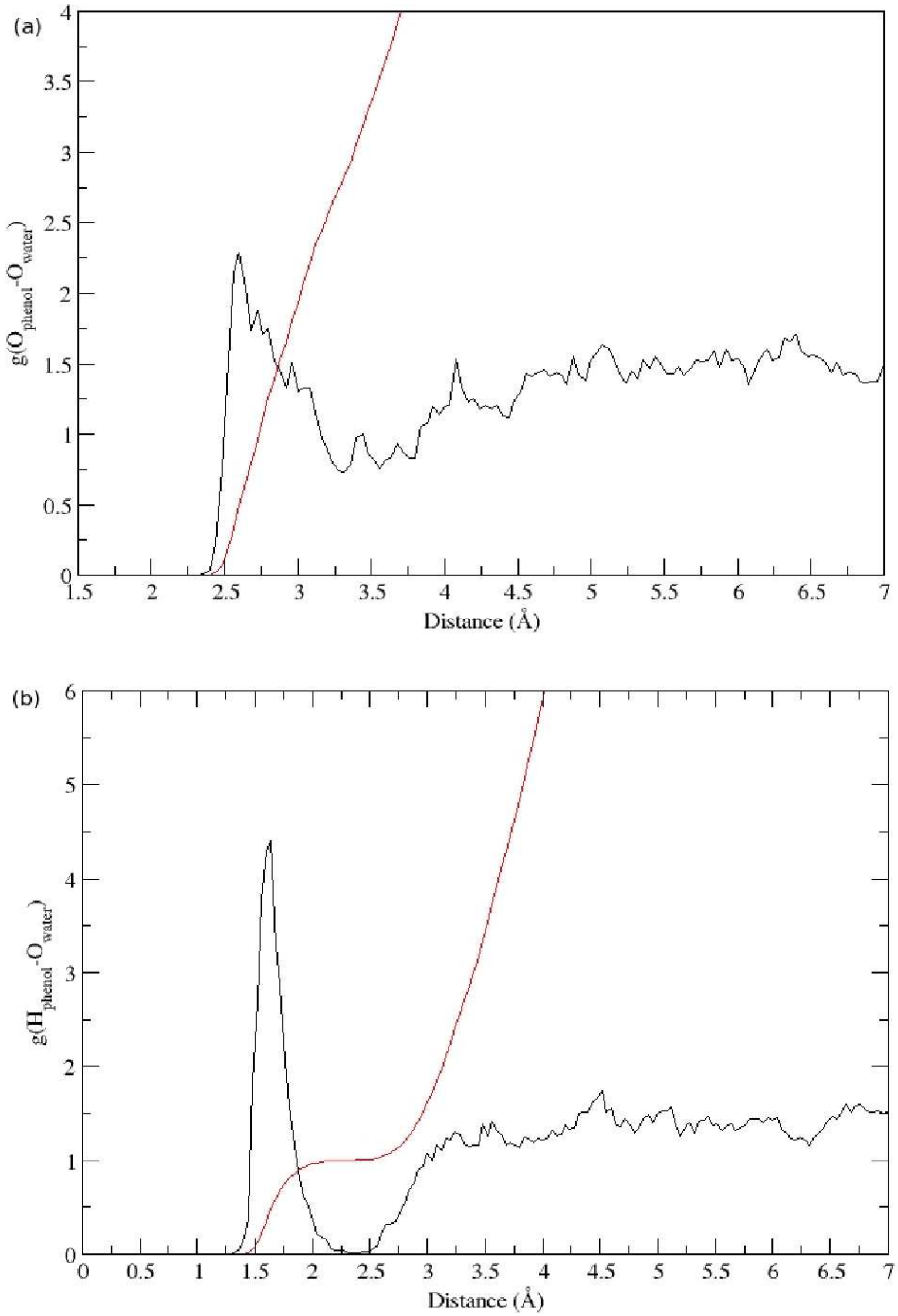

Fig. 4.7: Radial distribution functions of phenol oxygen (a) and hydrogen (b). All radial distribution functions (RDF) have been calculated in the following fashion. The number of events inside a certain bin-size has been calculated from the ADMP trajectory. This number has been then dived by the total number of configurations used, volume inside the spherical shell created by the chosen bin-size, and the number density of the system.

simulation mimicking the ACN-water mixture in the ONIOM/ADMP with non periodic boundary condition formalism is really a stiff task, because of the significant efforts required for the potential calibration. Here it is proposed an *a posteriori* discussion, based on trivial statistical considerations.

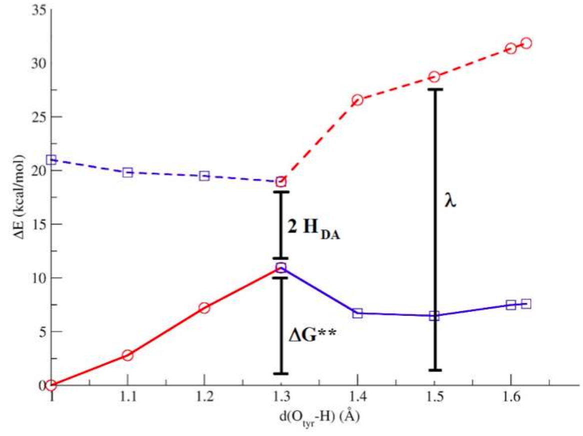

Fig. 4.8: Energy profile considering the tyrosine microsolvation represented by the α cluster. Parameters of the Murcus expression are also represented.

In a mixture 3:1 ACN-water the presence of a single water in a given volume is reduced to 1/4 with respect to the neat liquid. Therefore, the lifetime of clusters involving a large number of water molecules around the phenol can be expected to be quite reduced with respect to what inferred by MD in pure water. Hence, we can reasonably assume that the weight of α and β clusters is indeed more respect to the γ or δ. Doing so the statistic weight of α cluster rises becoming comparable to that of γ cluster.

The kinetic constant for the PCET reaction considering the tyrosine microsolvation represented by the α cluster, was evaluated by means of Marcus expression:

$$k = \frac{2\pi}{\hbar} \frac{H_{DA}^2}{\sqrt{4\pi\lambda k_B T}} exp \frac{\Delta G^\sharp}{k_B T} \tag{4.1}$$

where $\Delta G^\sharp$, H_{DA}^2 and λ represent the activation free energy, the electronic coupling and the reorganization energy, respectively (see fig. 4.8). We compute a k value of 7.55 x10^6 s^{-1} well in agreement with the experimental one of 3.0 x10^7 s^{-1}. More sophisticated model are required in the case of γ and δ clusters. Works are currently in progress in this direction. Moreover as future perspective we are trying to sample the ground state PES for the whole peptide inside a spherical box of 20.5 Å radius containing 1181 water molecules (see Fig.4.9).

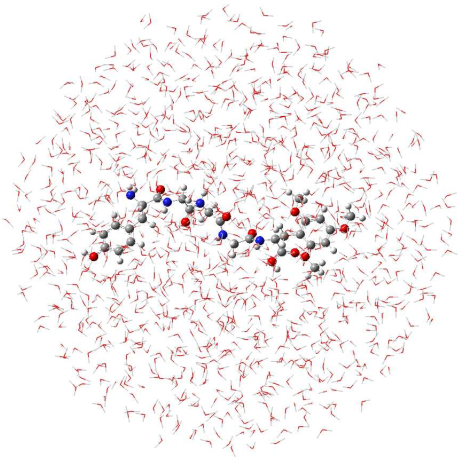

Fig. 4.9: Spherical box for $YGGGF_{TRM}$ dynamics.

Chapter 5

Modeling artificial leaf: electronical design of artificial molecular reaction center

Charge transfer elementary steps amply discussed in previous chapters are the cornerstone processes at the basis of natural and artificial photosynthesis.

As matter of fact the efficient combination of photoinduced electron transfer, excited state proton transfer and proton coupled electron transfer reactions by charge transfer molecular machines allow to harvest sunlight and convert it into useful electrochemical energy.

The award for the best efficient nanotechnology goes, of course, to Nature for the photosystem II. Indeed, it represents the best inspiration toward the developing of artificial leaves utilizing molecular assemblies for the light energy conversion. A large number of molecules that mimic one or more elements of PSII have evolved in order to build up a complex supramolecular architecture able to absorbing sunlight, converting light energy into electrochemical potential energy and finally transducing it into chemical accessible energy. In this chapter we will analyze the electronic properties of the artificial molecular reaction center performing the first two tasks, while molecular assays appealing as water oxidation catalysts will be the topic of the next chapter.

The main goal of the reaction center is to preserve some of the excitation energy as electrochemical potential creating a charge separation by photoinduced electron transfer. As explained in section nn in natural photosynthesis this process involves a cascade of electron transfers steps activated by the special chlorophyll P680. The presence of a miraculous tyrosine-hystidine pair leads, then, to electrons extraction from the WOC during the water oxidation process. Artificial reaction centers have to reproduce these features to be efficient and suitable for the application in photoelectrochemical cells.

At the state of the art the majority of these mimics use covalent bonds to join the molecular portion acting as electron donor/acceptor and ensure the necessary spatial proximity. Hence, the simplest artificial reaction center will consist of an electron donor (or acceptor) chromophore electronically coupled to an electron acceptor (or donor). The resulting assembly should display both absorption in the visible spectrum and a suitable oxidation potential to drive the consecutive redox processes on the WOC. This means that it is fundamental to calibrate at the same time the redox properties of the donor and acceptor moieties and their photophysical signatures. Theoretical modeling of these charge transfer molecular machine is, thus, crucial

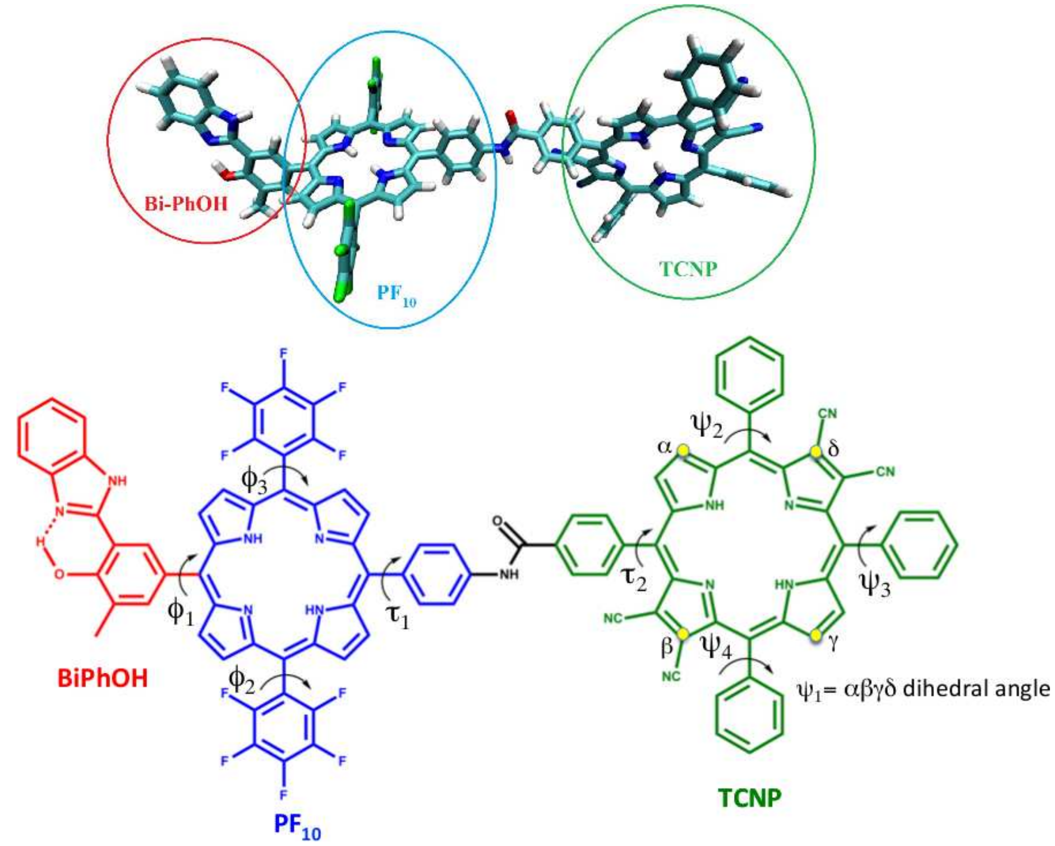

Fig. 5.1: Molecular structure of triad BiPhOH-PF$_{10}$-TCNP that is composed of three covalently linked subunits: BiPhOH, PF$_{10}$ and TCNP. Labelling of critical dihedral angles is also provided. ψ_1 is the α,β,γ and δ dihedral angle.

for their electronical design. A very promising artificial reaction center is a molecular triad, hereafter named BiPhOH-PF$_{10}$-TCNP, recently synthetized by Moore and co-workers to simulate the tyrosine-hystidine-P680 portion of the electron transfer chain in PSII. [23]

More closely it is composed (see fig. 5.1) by: i) a functionalized porphyrin moiety bearing two pentafluorophenyl groups (PF$_{10}$) which mimics the chlorophyll P680 exciton trap of PSII, and acts as primary electron donor; ii) a tetracyanoporphyrin (TCNP) ring which acts as electron acceptor thanks to the electron withdrawing effects of the cyano groups at the β positions of the tetrapyrrolic ring; and iii) a benzimidazole-phenol group (BiPhOH) which models the tyrosine hystidine pair of PSII thanks to the intramolecular hydrogen bond between the phenolic proton and the nitrogen atom of the benzimidazole group.

Moore and co-workers provided a detailed spectroscopic and electrochemical characterization of this molecular triad in benzonitrile explained by the complex decay pathways reported in Figure 5.2. [23] Based on their experimental data, their hypothesis is that the initial excitation of PF_{10} group is followed by singlet energy transfer to the TCNP moiety, whose excited state can relax by a photoinduced electron transfer toward a charge separated state giving rise to a Bi-PhOH-$PF_{10}^{\bullet+}$-$TCNP^{\bullet-}$ species. They proposed that this specie rapidly undergoes to a PCET reaction in which an electron is transferred from the phenol to the $PF_{10}^{\bullet+}$ group, while the phenolic proton is transferred towards the benzimidazole group giving rise to the final species postulated to be the BiH^{+}-$PhO^{\bullet}$-PF_{10}-$TCNP^{\bullet-}$ one.

Since time resolved spectra suggest that this charge separated state has a long lifetime and an high redox potential, this triad becomes particularly attractive for the possibility of coupling it to water oxidation catalysts for use in aritificial photosynthetic fuel production. Nonetheless for the time being the nature and the relative energies of all the electronic states involved in this complex mechanism after light excitations have been only experimentally indirectly estimated by combining the redox potential, absorption and emission data of the isolated form of three molecular frag-

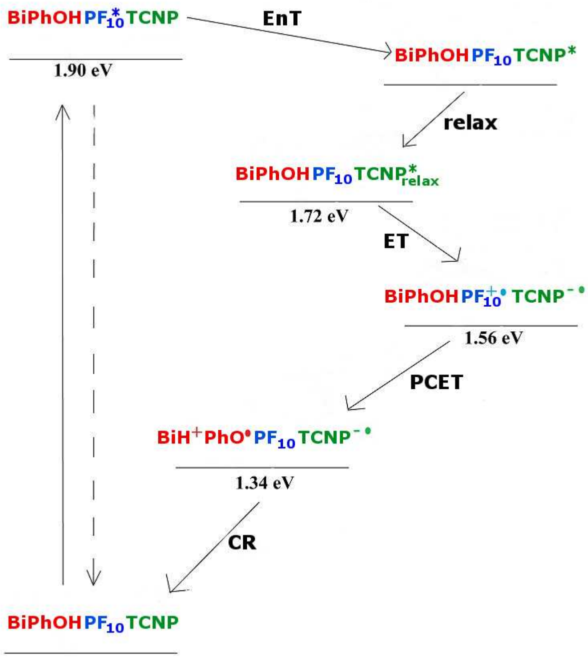

Fig. 5.2: Experimentally proposed energy level diagram of decay pathways for triad BiPhOH-PF_{10}-TCNP following excitation of the PF_{10} unit in benzonitrile. The energy levels were derived by Moore and co-workers from steady state absorption, fluorescence, and electrochemical data. EnT, PET, PCET and CR stay for energy transfer, photoinduced electron transfer, proton coupled electron transfer and charge ricombination, respectively. [23]

ments composing the triad. Moreover, at the present, no clear direct evidences for the formation of the final PCET product have been obtained from experiments. In a recent publication [4] Moore and co-worker stated that 'indirect evidence for PCET comes from reduction potentials of model compounds [118] which indicate that PF_{10} would not generate sufficient driving force for the formation of the Bi-$PhOH^{\bullet+}$-PF_{10}-$TCNP^{\bullet-}$ and thus implies the formation of the BiH^{+}-$PhO^{\bullet}$-PF_{10}-$TCNP^{\bullet-}$.'

In order to tune and control the properties of such triad a more detailed knowledge of the electronic structure of all the intermediate state involved in the excited state evolution is nonetheless mandatory. Here, for the first time, we provide a complete theoretical structural and energetic characterization of all the crucial species involved in the decay pathway (Bi-PhOH-$PF_{10}^{\bullet+}$-$TCNP^{\bullet-}$, Bi-$PhOH^{\bullet+}$-PF_{10}-$TCNP^{\bullet-}$ and BiH^{+}-$PhO^{\bullet}$-PF_{10}-$TCNP^{\bullet-}$) simulating the whole photocycle.

The whole theoretically simulated decay pathways is summarized in Figure 5.3 (for comparison the experimentally proposed decay pathways is shown as inset). All the involved steps are deeply investigated in the next sections starting from the absorption event.

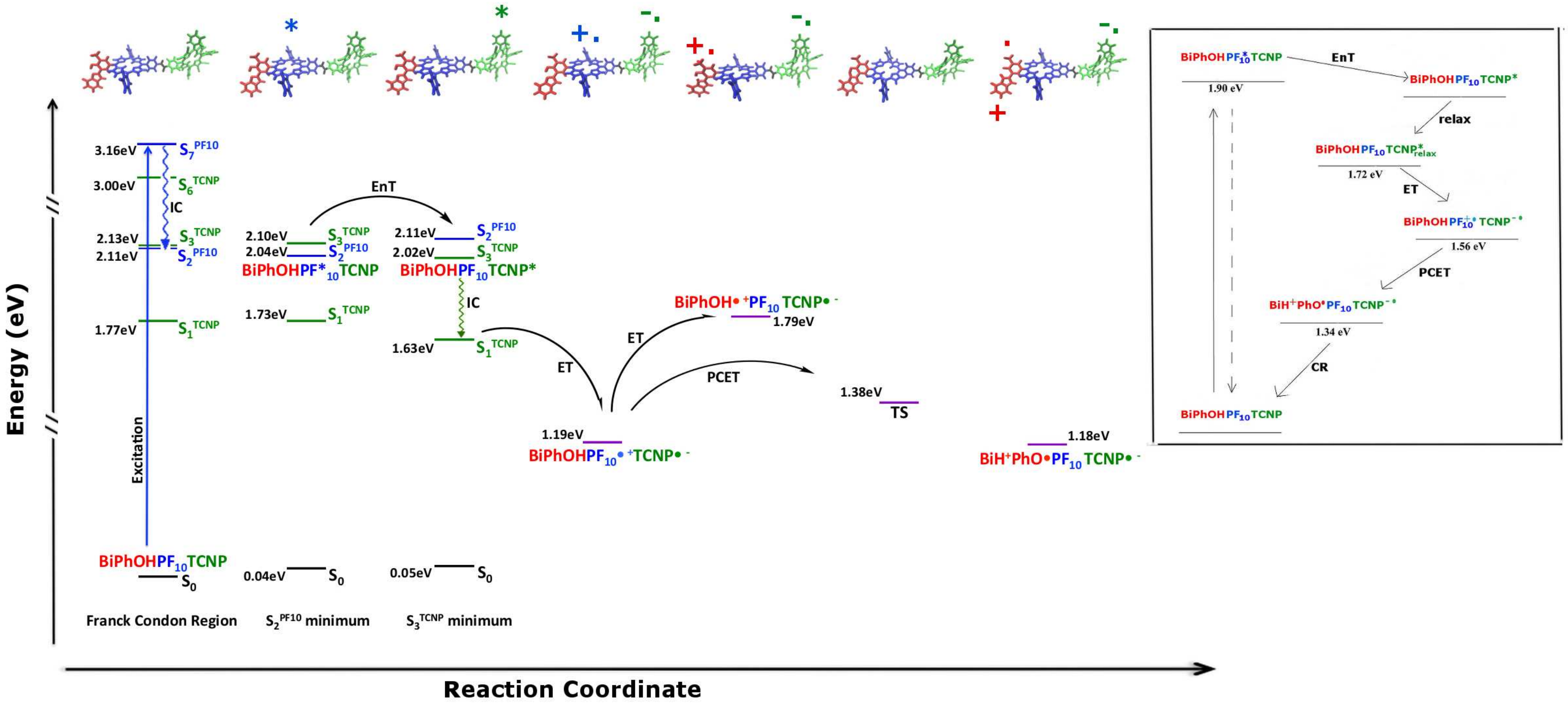

Fig. 5.3: Simulated decay pathway for the triad BiPhOH-PF$_{10}$-TCNP. Excitation, Internal conversion (IC), Energy Transfer (EnT), Electron Transfer (ET) and Proton Coupled Electron Transfer (PCET) steps are represented. Energy levels have been computed through TD-DFT and Broken Symmetry approaches. The vertically computed excited states are reported in the Franck Condon region, $S_2^{PF_{10}}$ and S_3^{TCNP} energy minimum. The S_0 values are reported respect the S_0 value at the Franck Condon region. The same holds also for the Broken Symmetry energy states. In the inset experimentally proposed energy level diagram of decay pathways for triad following excitation of the PF$_{10}$ unit in benzonitrile.

To simplify the notation in the following discussions each excited state of the triad will be labelled as S_n^X. The X superscript identifies the molecular moiety mostly involved in the excitation (i.e. X can be TCNP or PF_{10}) while the subscript n specifies the electronic state number according to its energy. S indicates that each excited state computed is a singlet.

5.1 Excitation in the Franck Condon region

Initially the triad is excited from its ground state S_0 minimal energy structure. At the S_0, the two subunits PF_{10} and TCNP of BiPhOH-PF_{10}-TCNP are almost perpendicular while the BiPhOH and PF_{10} rings are twisted by roughly 67° (ϕ_1=-67°, see table 5.1 for the principal structural parameters) suggesting a greater electronic coupling among them. The PF_{10} moiety is highly symmetric with the pentafluorephenyl groups similarly oriented with respect to the plane of the porphyrin ring. Instead the TCNP unit assumes a non planar structure due to steric interactions between the cyano and phenyl groups, respectively in the beta and meso positions of the tetrapyrrolic ring. These interactions also lead to an orientation for the phenyl groups far from the perpendicular one (see ψ_2, ψ_3, ψ_4 dihedral angles in table 5.1). The experimental absorption spectra for the triad in benzonitrile shows two intense broadened bands in the Soret regions centred at 2.76 and 2.92 eV, respectively. The excited state features have been evaluated using a range separated hybrid functional, i.e. the CAM-B3LYP one, [119] which gives a more reliable description of the various excited states compared to other density functionals. This is in agreement with

Table 5.1: Characteristic dihedral angles (in degree, refer to figure 5.1) computed for the triad in different electronic states.

Electronic state	ϕ_1	ϕ_2	ϕ_3	ψ_1	ψ_2	ψ_3	ψ_4
S_0	-67.05	-104.85	104.05	-18.72	-61.59	-119.82	-62.35
$S_2^{PF_{10}}$	-61.38	-113.29	112.12	-14.00	-67.74	-113.68	-67.96
S_3^{TCNP}	-68.13	-109.72	109.47	-18.16	-62.86	-117.68	-64.13
$(S_1^{TCNP})_{relaxed}$	-68.15	-109.58	109.02	-25.03	-52.79	-127.32	-53.64
Bi-PhOH-$PF_{10}^{\bullet+}$-$TCNP^{\bullet-}$	-54.28	-111.88	107.24	-17.61	-62.92	-117.88	-64.33
BiH^+-$PhO^{\bullet}$-PF_{10}-$TCNP^{\bullet-}$	-49.54	-109.92	105.38	-17.77	-63.03	-117.94	-64.09
Bi-$PhOH^{\bullet}$-PF_{10}-$TCNP^{\bullet-}$	-92.11	-109.33	108.68	-17.54	-63.49	-117.49	-64.21

Amos and co-workers [120] results showing that CAM-B3LYP predicts qualitatively reasonable spectra for porphyrin, in excellent agreement with complete-active-space plus second-order Moller-Plesset perturbation theory [121] and symmetry-adapted cluster configuration interaction calculations. [122]

Two intense electronic transitions have been computed at 3.00 eV (oscillator strength (f)=2.966, state S_6^{TCNP}) and 3.16 eV (f=2.157, state $S_7^{PF_{10}}$) localized respectively on the TCNP group and on the PF_{10} one (see the excitation in the Franck Condon region of figure 5.3). These electronic transitions match in terms of both energy and nature with those computed for the isolated BiPhOH-PF_{10} diad and TCNP showing that the absorption spectra of BiPhOH-PF_{10}-TCNP can be interpreted simply as the sum of those of its molecular components, in agreement with the experimental findings.

5.2 Energy Transfer modeling

After the excitation to the state $S_7^{PF_{10}}$ a fast internal conversion to a state still localized on PF_{10} but at lower energy (state $S_2^{PF_{10}}$) can take place. This is in line with the photochemistry of porphyrin molecules that, following the absorption to a S_2 state (corresponding to the Soret band), give a rapid internal conversion from S_2 to S_1, finally emitting from S_1. [123] The $S_2^{PF_{10}}$ state has been vertically computed at 2.11 eV (f=0.017) on the ground state optimized structure (the orbitals involved in the transition are reported as figure 5.4) while upon relaxation the final minimum energy for this state is computed at 2.04 eV (f=0.089).

This value can be compared with the 1.90 eV proposed by Moore and co-workers on the basis of fluorescence data of the isolated PF_{10} unit.8 Very close in energy to $S_2^{PF_{10}}$ we found another state characterized by an electronic excitation completely localized on the TCNP unit (S_3^{TCNP}) (see figure 5.4 for the orbitals involved). The S_3^{TCNP} state is computed at 2.13 eV (f=0.103) on the Franck Condon region and at 2.10 eV (f=0.215) on the $S_2^{PF_{10}}$ energy minimum. The energy transfer from PF_{10} to TCNP in the triad (first step in the figure 5.2) can take place and it corresponds to an exchange between the $S_2^{PF_{10}}$ and S_3^{TCNP} states occurring during the structural relaxation of the S_3^{TCNP} electronic state as reported in figure 5.3. In Figure 5.5 a linear sincronous path between the $S_2^{PF_{10}}$ and S_3^{TCNP} excited states minima is reported. It clearly shows the exchange of the two involved excited states during the relaxation of the S_3^{TCNP} state.

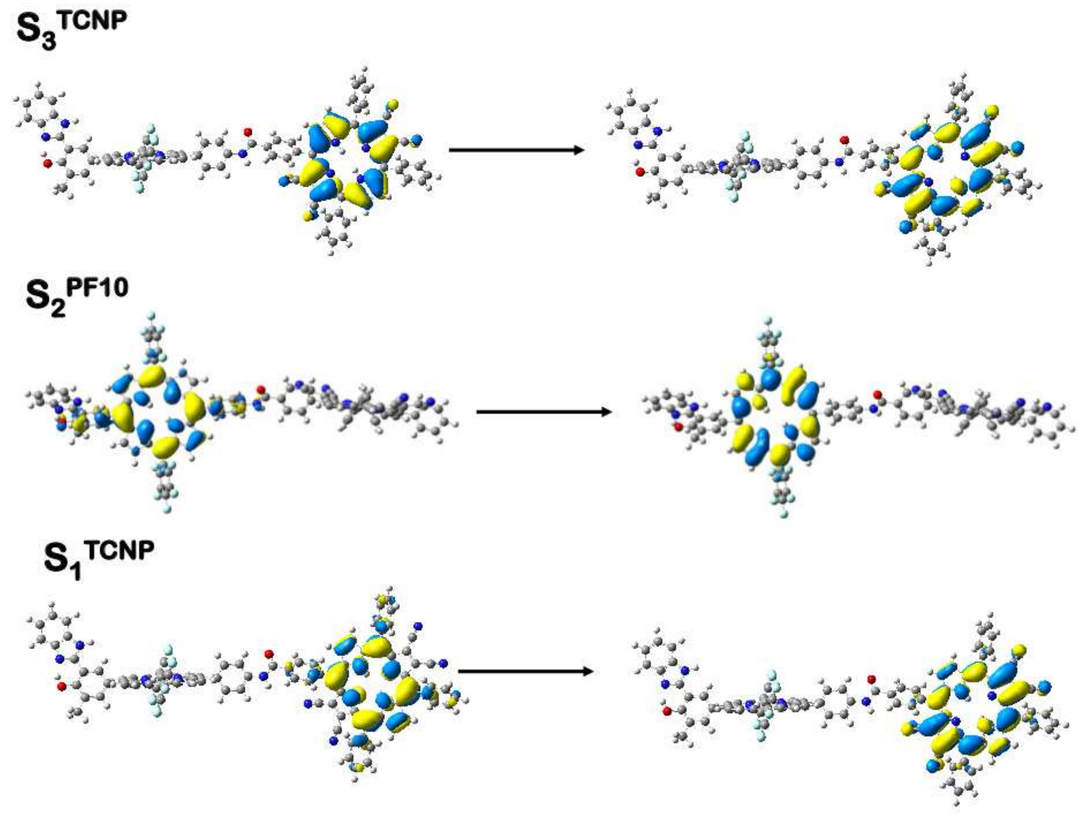

Fig. 5.4: Molecular orbitals involved in the transition leading to $S_2^{PF_{10}}$ (computed on the $S_2^{PF_{10}}$ state energy minimum), S_3^{TCNP} and S_1^{TCNP} (computed on the S_3^{TCNP} state energy minimum).

Many internal degrees of freedom are involved in this path. Starting from the Franck-Condon region, the TCNP tetrapyrrolic ring partially alleviates its distortion in the $S_2^{PF_{10}}$ minimum. Indeed the ψ_1 dihedral angle changes of about 5 degrees between the ground and the $S_2^{PF_{10}}$ excited state minima. The relative orientation of TCNP and PF_{10} molecular moieties slightly changes as well as that of BiPhOH and PF_{10} (see table 5.1). However, while experimentally the fluorescence from the TCNP is observed at 1.72 eV, further relaxation of the structure at S_3^{TCNP} does not lead to an energy value below 2.02 eV (f=0.409), corresponding to the excited state

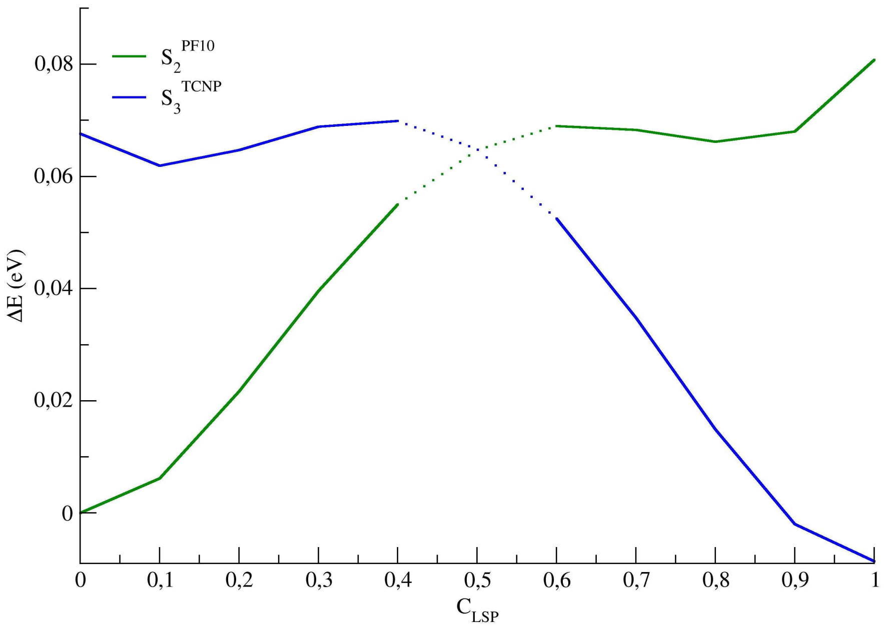

Fig. 5.5: Evolution of S_3^{TCNP} and $S_2^{PF_{10}}$ excited states along the Linear sincronous path connecting the $S_2^{PF_{10}}$ and S_3^{TCNP} energy minima.

energy minimum. More importantly, experimentalists hypothesize that this state corresponds to the reactant for an ET process (see figure 5.2). As matter of fact, it was no possible to individuate a CT configuration close to the S_3^{TCNP} minimum. As we will discuss shortly, an electron transfer is unfavorite for the S_3^{TCNP} also for the structural and electronic arrangement of the TCNP moiety (see table 5.1 and fig. 5.4 for the MOs involved in the electronic transition). Instead (at the S_3^{TCNP} minimum), an energy of 1.63 eV (f=0.473) has been calculated for another electronic state (S_1^{TCNP}) whose electronic excitation is completely localized on the TCNP group (see figure 5.4 to the MOs involved in the transition). The energy difference (0.39

eV) corresponds to about 3100 cm^{-1}. We can therefore reasonably propose an interconversion between the S$_3^{TCNP}$ and S$_1^{TCNP}$, and assume the S$_1^{TCNP}$ state as the electron transfer reactant (figure 5.3). This result leads to the involvement of a further state to the experimentally hypothesized cascade.

5.3 PhotoInduced Electron Transfer modeling

The main difference between the electronic arrangement of the S$_3^{TCNP}$ and S$_1^{TCNP}$ states is a depletion of the electronic density from the TCNP moiety near the cyano groups. This feature allows for a profound change of both the electronic and nuclear arrangements during the S$_1^{TCNP}$ relaxation. The state assumes a great charge transfer character from the PF$_{10}$ to the TCNP unit (see figure 5.6 for the MOs involved in the electronic excitation).

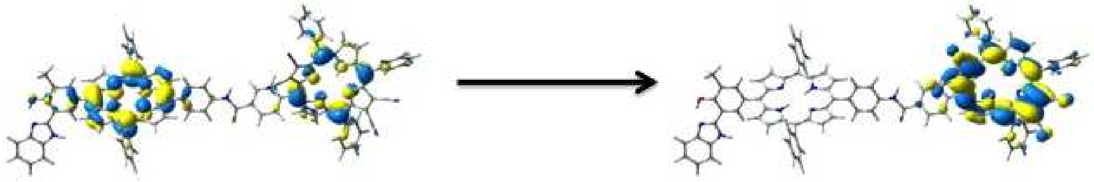

Fig. 5.6: Molecular orbitals involved in the transition leading to the relaxed S$_1^{TCNP}$.

We also observe the distortion of the TCNP tetrapyrrolic ring (see table 5.1). The ψ_1 dihedral angle, describing the distortion of the porphyrin ring, changes from about -14° to -25° during this relaxation, driving the variation in the nature of the MOs involved in the S$_1^{TCNP}$ electronic transition. Of course this deformation increases the steric repulsions between the cyano and phenyl groups which in turn assume a more planar orientation with respect to the porphyrin ring. The TCNP deformation is a key structural motif important for the charge transfer event. Interestingly, this change in the nature of the locally excited S_1^{TCNP} state was observed only for calculations performed in benzonitrile solution, while it was not reproduced in analogue S_1^{TCNP} optimization in cyclohexane. In this case, the excitation remains localized on the TCNP moiety. This clearly indicates that only polar solvents with high dielectric constant are able to stabilize the electron transfer product. This perfectly matches the fact that a high quantum yield for the PET reaction is experimentally detected only in polar medium (benzonitrile). The energy of the relaxed S_1^{TCNP} state is computed at 1.40 eV (f=0.565). Within the TD-DFT framework this is the best picture achievable for the electron transfer product. In order to describe the evolution of this charge separated state, the broken symmetry (BS) approach was, then, applied.

Within the broken symmetry formalism, developed by Noodleman and co-workers, [124–127] one tries to obtain a wavefunction that breaks spatial and spin symmetry. This allows to simulates a multideterminantal character within a single determinant framework. Until now this methods was successfully adopted especially to compute the magnetic properties of metal coordination compounds, but now we riproposed it to describe and characterize a full intramolecular charge transfer system.

In this way, a open shell BS singlet state characterized by a spin density localized

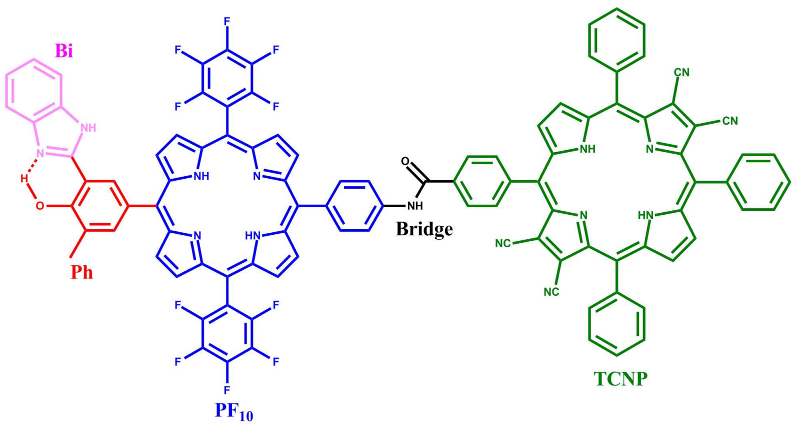

Fig. 5.7: Definition of the molecular fragments Bi,Ph,PF_{10}, TCNP. They have been used to analyse the Mulliken Spin density.

on the PF_{10} and the TCNP group has been obtained. The spin density plot and the Mulliken spin density integrated for fragments (for the fragments definition see figure 5.7) are reported for this structure in figure 5.8a.

Looking at the Mulliken spin density integrated for fragments its clear that this specie represents the PET product, namely the Bi-PhOH-$PF_{10}^{\bullet+}$-TCNP$^{\bullet-}$ specie. Indeed two unpaired electrons with opposite spin are localized on the PF_{10} and TCNP moieties, respectively, with negligible contribute on the BiPhOH group. The Mulliken charge analysis for fragments reveals a net positive charge of +1.10 on the PF_{10} unit and a net negative charge of -0.93 on the TCNP fragment. This is, of course, what expected following an electron transfer from the PF_{10} to the TCNP group. The Bi-PhOH-$PF_{10}^{\bullet+}$-TCNP$^{\bullet-}$ specie represents the reactant for the next PCET step.

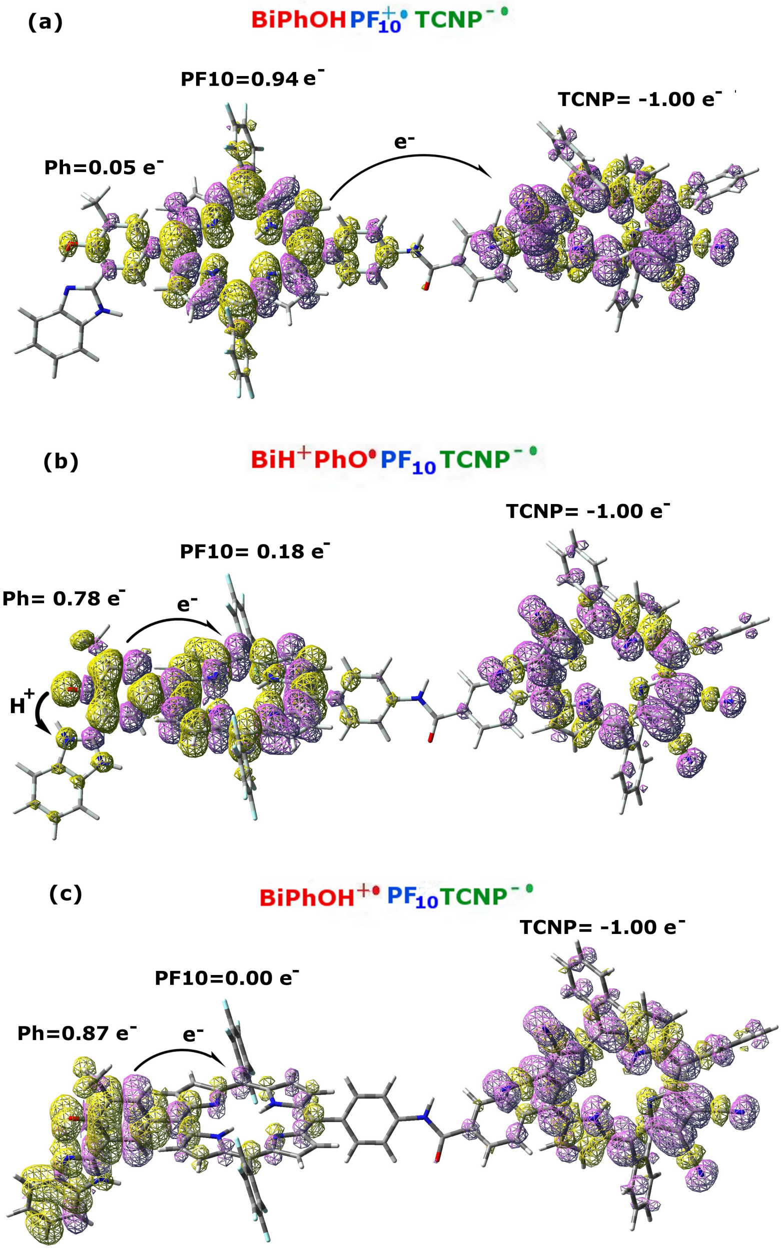

Fig. 5.8: a) Spin density plot for the electron transfer product (Bi-PhOH-PF$_{10}^{\bullet+}$-TCNP$^{\bullet-}$) in the broken symmetry approximation. b) Spin density for the proton coupled electron transfer product (BiH^{+}-PhO$^{\bullet}$-PF$_{10}$-TCNP$^{\bullet-}$). c) Spin density plot for the electron transfer product (Bi-PhOH$^{\bullet}$-PF$_{10}$-TCNP$^{\bullet-}$). Integration for fragments of the Mulliken spin density is also reported.

5.4 Proton Coupled Electron Transfer step

In order to characterize the PCET reaction, we chose the phenol oxygen-hydrogen ($O_{Ph}H$) distance as representative of the proton transfer coordinate. The energy profile obtained by a relaxed scan along this coordinate at TD-DFT level showed only a negligible variation of the nature in the S_1^{TCNP} electronic state, that means no ET accompanied the PT event. Hence, the BS approach was adopted to characterize the PCET reaction.

A broken symmetry solution corresponding to the BiH^+-$PhO^\bullet$-PF_{10}-$TCNP^{\bullet-}$ adduct was obtained. In figure 5.8b we showed the spin density plot and the Mulliken spin density integrated for fragments of this specie. The analysis of Mulliken spin density integrated for fragments shows the electronic holes localized on both the TCNP (-1.0e^-) and phenol (0.78e^-) units. The $O_{Ph}H$ distance is 1.863 Å in this structure, while the imidazole nitrogen-hydrogen (NIm-H) distance is 1.023 Å.

We observed also some spin polarization on the PF_{10} moiety. This is principally due to the strong electronic coupling between the BiPhOH and PF_{10}. The transition state (TS) for the PCET step has been also located, with an imaginary frequency at -1169cm^{-1}. The $O_{Ph}H$ and NIm-H distance are respectively of 1.272 and 1.205 Å in the transition state. The integration of the intrinsic reaction coordinate has been also carried out in order to follow the variation of the spin density along the reaction path (see figure 5.9). From figure 5.9 it is clear that starting from the Bi-PhOH-$PF_{10}^{\bullet+}$-$TCNP^{\bullet-}$ specie, an electron is transferred from the phenol toward the PF_{10} group saturating its electronic hole when the proton is bounded to the imidazole nitrogen.

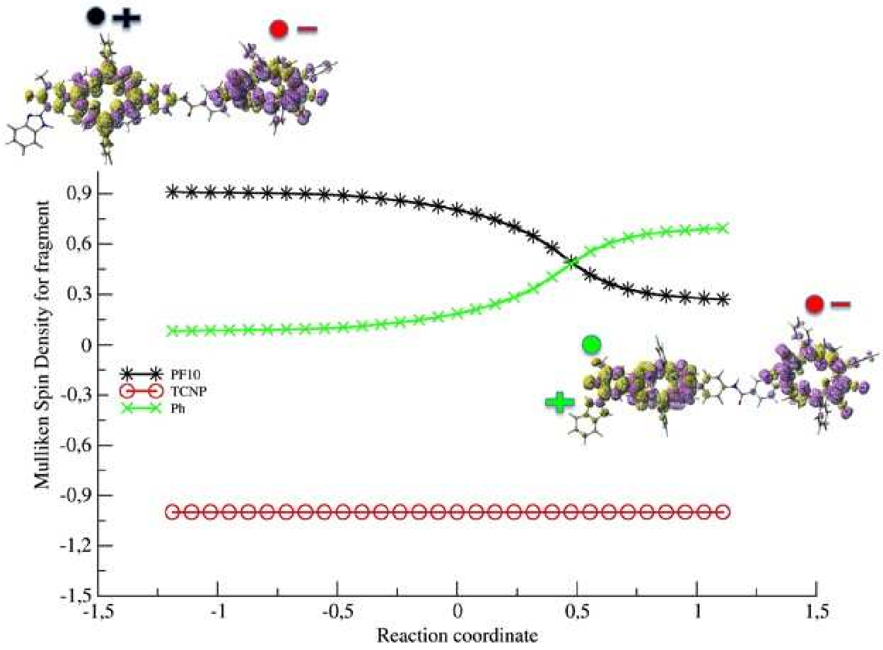

Fig. 5.9: Mulliken spin density integrated for fragment along the IRC for the PCET reaction.

The spin density on the TCNP fragment is constant revealing the formation of the BiH^+-$PhO^\bullet$-PF_{10}-$TCNP^{\bullet-}$. In spite of a barrier of 0.19 eV (4.44 kcal/mol), PCET product is slightly favoured of about 0.007 eV (0.16 kcal/mol).

For what regards the PCET mechanism, the ϕ_1 dihedral angle is the degree of freedom principally involved in the reaction. It defines the relative orientation between the BiPhOH and the PF_{10} units varying of about 5 degrees during the reaction. ϕ_1 dihedral angle is therefore a very important parameter because it controls the electronic coupling between the two units, thus modulating the electron transfer among them. Figure 5.10 shows how the Mulliken spin density on the PF_{10} and Ph fragments vary at the variation of the ϕ_1 dihedral angle from -45° to -90°, computed by single point calculations on the broken symmetry BiH^+-$PhO^\bullet$-PF_{10}-$TCNP^{\bullet -}$ state. Its clear that when the two rings are almost perpendicular (ϕ_1= -90°) the spin density on the PF_{10} fragment is zero and that on Ph is about one.

Varying the ϕ_1 angle the spin density on the PF_{10} moiety gradually increases reaching its maximum value (about 0.2) when the two rings become more planar. At the same time the spin density on the Ph fragment decreases reaching at least the value of about 0.8 . Of course this internal mode is crucial to drive the PCET event, and has to be considered as a critical motif for the future design of these charge transfer molecular machines. Instead the TCNP tetrapyrrolic ring deformation doesnt change during the reaction.

Within the broken symmetry framework, it has been also computed the solution corresponding to the transfer of an electron from the Ph group towards the PF_{10} one, without proton transfer between phenol and benzimidazole groups, namely the Bi-$PhOH^{\bullet +}$-PF_{10}-$TCNP^{\bullet -}$ specie, (see figure 5.8c for the spin density plot). This state is found to lie 0.60 eV (13.89 kcal/mol) higher in energy with respect to the Bi-PhOH-$PF_{10}^{\bullet +}$-$TCNP^{\bullet -}$ one (see figure 5.3). Its formation is, thus, energetically unfavourable. This in turn represents the first direct evidence for the for-mation of the PCET adduct. Once again Bi-$PhOH^{\bullet +}$-PF_{10}-$TCNP^{\bullet -}$ and Bi-PhOH-$PF_{10}^{\bullet +}$-

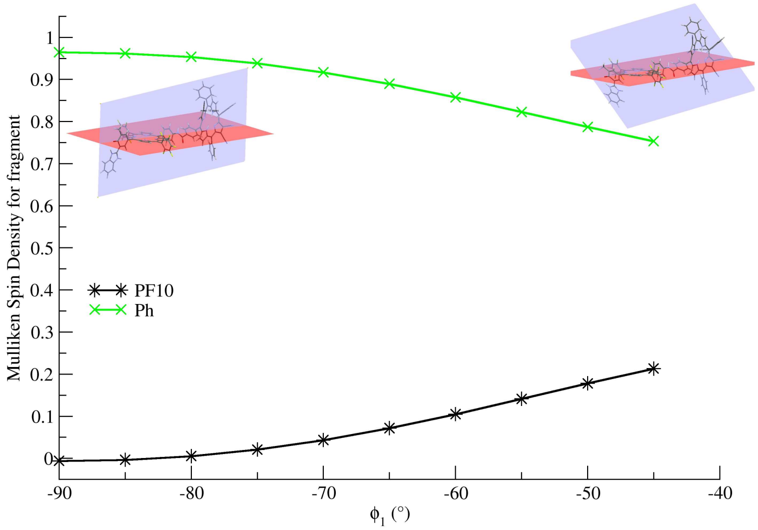

Fig. 5.10: Mulliken spin density integrated for fragment along the variation of the 1 dihedral angle on the BiH$^+$-PhO$^\bullet$-PF$_{10}$-TCNP$^{\bullet -}$ state.

TCNP$^{\bullet -}$ differ principally for the mutual orientation of the BiPh and PF$_{10}$ moiety, namely for the ϕ_1 dihedral angle (see table 5.1). More closely this degree of freedom changes of about 40° between the two structures, with the Bi-PhOH$^\bullet$-PF$_{10}$-TCNP$^{\bullet -}$ specie favoured by the perpendicular arrangement between the Ph and PF$_{10}$ rings.

5.5 Resume of whole simulated photocycle

The whole excited state cascade of triad BiPhOH-PF$_{10}$-TCNP is here resumed. The electronic excitation of the PF$_{10}$ group is the starting point for the process. A very intense electronic transition, which involved MOs are completely localized on the PF$_{10}$ moiety, has been computed at 3.16 eV on the ground state minimum. A fast internal conversion to the lower energy state still localized on this molecular portion, S$_2^{PF_{10}}$ (computed at 2.11 eV) has been hypothesized. Near to S$_2^{PF_{10}}$ another state

(S_3^{TCNP}) characterized by an electronic excitation completely localized on the TCNP unit, has been computed. The relaxation of S_3^{TCNP} leads to the crossing with $S_2^{PF_{10}}$. The energy transfer from the PF_{10} to the TCNP group corresponds to an exchange between these two electronic states $S_2^{PF_{10}}$ and S_3^{TCNP}, occurring during the S_3^{TCNP} relaxation. The interconversion between the S_3^{TCNP} and the state still localized on the TCNP group at lower energy (S_1^{TCNP}), is a crucial step in the excited state decay pathways to allow for the ET process. Bi-PhOH-$PF_{10}^{\bullet+}$-$TCNP^{\bullet-}$ and BiH^+-$PhO^\bullet$-PF_{10}-$TCNP^{\bullet-}$ are almost degenerate and the PCET reaction proceeds through a barrier of 4.44 kcal/mol. The formation of Bi-$PhOH^{\bullet+}$-PF_{10}-$TCNP^{\bullet-}$ specie it is not favoured compared to BiH^+-$PhO^\bullet$-PF_{10}-$TCNP^{\bullet-}$ one of about 14 kcal/mol.

The driving force of the various charge transfer steps have been successfully catched providing very important insights to support the future electronical design strategies of such molecular assays.

Finally the combination of TD-DFT and broken symmetry approach is a powerfull tool to describe accurately the complexity of the structural and electronic evolution of the cascade of a PSII mimic.

Chapter 6

Modeling artificial leaf: electronical design of water oxidation catalyst

The development of successful photoelectrochemical cells able to convert solar into chemical energy relies on the possibility to catalyze one of the most thermodynamically demanding reactions in biology: the water oxidation.

$$2\ \mathrm{H_2O}_{(l)} \longrightarrow \mathrm{O}_{2(g)} + 4\ \mathrm{H}^+_{(aq)} + 4\ \mathrm{e}^-_{(g)}$$

Indeed a standard reduction potential of 1.23 V versus the standard hydrogen electrode (SHE) is associated to this reaction, which involves the removal of four protons and four electrons together with the formation of an oxygen-oxygen (O-O) bond. Artificial reaction centers, analyzed in the last chapter, participate in the electrons/protons extraction, while the O-O bond formation occurs thanks water oxidation catalysts. In spite the huge efforts devoted in the last years to provide efficient and stable WOCs, the four electrons water oxidation reaction is the principal bottlenecks toward the development of winning water splitting cells. [128, 129]

Currently both heterogeneous and homogeneous molecular metal oxide WOCs have been reported. [129] On the one hand metal oxide nanoparticles WOCs are in general orders of magnitude slower than their molecular counterpart although they are synthetically easy to obtain and generally stable. Iridium oxide based WOCs are the most promising heterogeneous catalysts from this point of view. On the other hand homogeneous molecular WOCs often display a limited stabilty and durability, but at the same time offer all the benefits of molecular rational design. [2]

As matter of fact the performances of molecular WOCs can be tuned through choice of transition metal, oxidation state and geometry and most of all through structural modifications of the ligands in order to increase the solubility of the molecular complex and to enable its anchoring to the electrode. Moreover their kinetic and mechanistic characterization is easier to achieve compared to the heterogeneous ones.

For all these reasons many researchers are working to develop molecular WOCs operating in homogeneous solution. [129]

Among all elements, transition-metals of Groups 7, 8, and 9, i.e. Mn, Ru, Ir, occupy a privileged position for water oxidation having easy access to high oxidation states. [129] At the state of the art ruthenium and iridium based molecular complexes exhibited very good catalytic properties. A special ruthenium-based complex, the so-called Meyers blue dimer requires particular attention thanks to its robustness and well-characterized activity. [130]

Nonetheless these metals are rare and thus expensive elements, so much attention continues to be focused on the design of catalysts based on earth-abundant metals, i.e. Fe,Co and Mn. Of course manganese, represents the archetypal element for water-oxidizing chemistry considering its foundamental role in PSII (see section 1.4). Several manganese-based complexes have been proposed in the last decade, but only a few are effectively capable of catalyzing water oxidation. [131] Moreover the active manganese complexes usually have very small turnover number. Taking inspiration from PSII oxygen evolving complex can be the turning point for the design and synthesis of succesful WOCs.

In this respect, very recently Zhang and co-workers proposed a calcium tetramanganese complex $[Mn_4CaO_4(Bu^tCO_2)_8(Bu^tCO_2H)_2(py)]$ (Bu^t, tert-butyl; py, pyridine), hereafter named complex A (see figure 6.1), strongly related to the native OEC in PSII. [24]

Electronical, structural and functional features of natural OEC are all well reproduced by complex A. Indeed by means of cyclic voltammetry it was shown that this mimic can undergo a sequential one electron oxidation mimicking the electronic features of the OEC. [24] As matter of fact the structure of the $[Mn_4CaO_4]$ core as well as the oxidation states of the four manganese ions undergoes changes during the water oxidation reaction cycle, which comprises several distinct redox intermediates, the S_n states, where the subscript n indicates the number of stored oxidizing equivalents required to split two water molecules.

Experimental data [24] suggest for the as-synthesized complex, oxidation states of Mn_1^{3+}, Mn_2^{4+}, Mn_3^{4+}, Mn_4^{3+} (see figure 6.1 for labels) in complete analogy to the S_1 state of the natural OEC. Thus, starting from the S_1 state we carried out in the next section a complete theoretical structural and electronical characterization of complex A for the S_1, S_2 and S_3 states, both in the gas and in solvent phase.

Regarding the structural properties, crystallographic data of complex A in the S_1 state, reveals that it presents a $[Mn_4CaO_4]$ core in which a dangling Mn ion is attached to a $[Mn_3CaO_4]$ cubane as in the native OEC (figure 6.1).

Moreover the integration of the Ca ion into the $[Mn_3CaO_4]$ cubane as well as its anchoring by three carboxylates bridging to Mn ions is identical in the two cases. However some differences with the OEC appear: first of all the μ_2 oxo bridge linking Mn_3 and Mn_4 in the native OEC is replaced by a bridging carboxylate group in complex A and most importantly the coordinated water molecules to Mn_4 and Ca ions are lost replaced by more complex ligands (figure 6.1).

This is a very critical point because it has been experimentally observed that the addiction of trace amount of water modifies the complex structure through ligand exchange leading to obscured oxidation and reduction waves in the cyclic voltammogram. [24] Few insights are, in turn, available on its reactivity and the theoretical support became crucial to investigate the performances of complex A in the O-O bond formation.

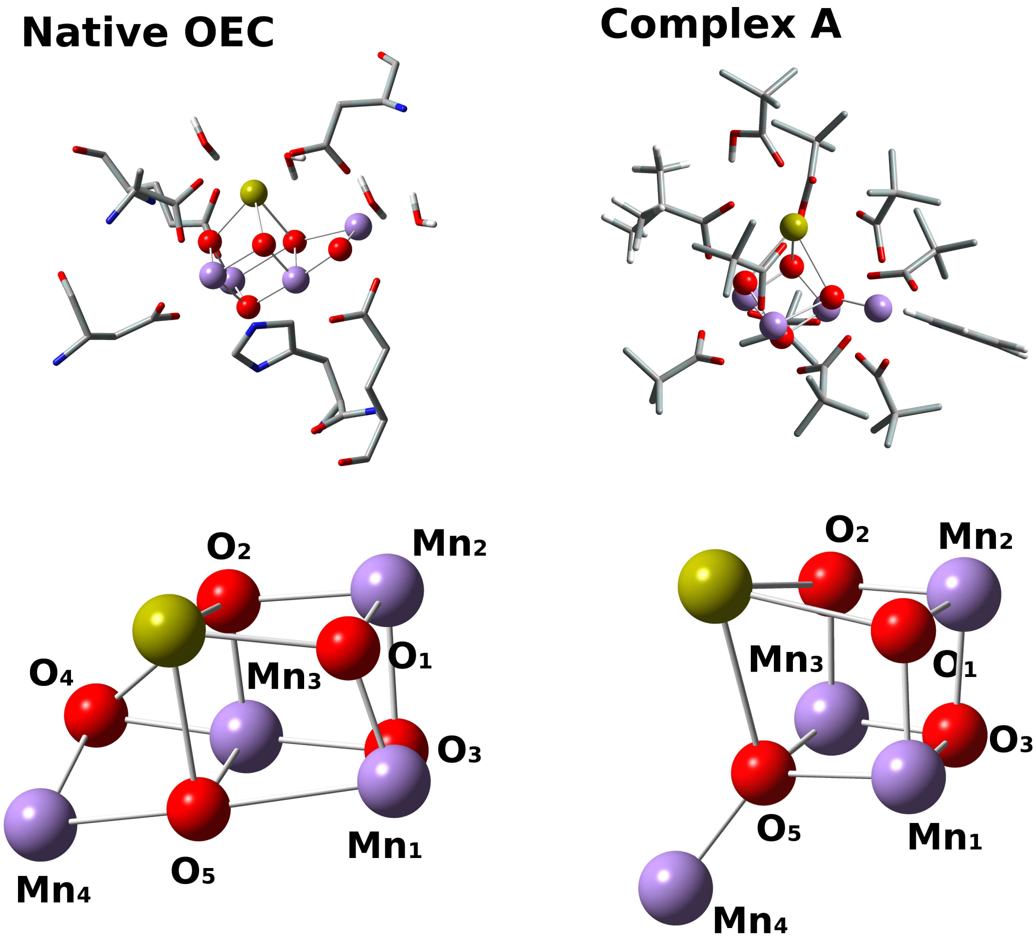

Fig. 6.1: Crystal structure of the native OEC and the synthetic complex A. The $CaMn_4$ core is also represented. OEC structure from 3ARC pdb.

Thus, after a complete analysis of the structural and electronical features of the complex A, we simulated its catalytic cycle exchanging some ligands with water molecules in such a way to reproduce the position of the OEC crystallographic water.

6.1 Complex A: structural and electronical features

A complete structural and electronical characterization of complex A for the S_1, S_2 and S_3 states, has been performed both in the gas and in condensed phase, considering acetonitrile as solvent. The polarizable continuum model in its conductor like version was adopted to represent the bulk solvation effects. For each S_n state several electronic configurations as well as spin states have been considered. Full geometry optimizations were performed at UB3LYP level of theory adopting LANL-2DZ basis set for Mn and Ca, 6-31G(d) for N and O, and 6-31G for C and H. Oxidation states for each Mn ion were determined by examination of the Mulliken spin population, such that Mn^{IV} and Mn^{III} have calculated spin population of approximately 3 and 4, respectively. In the following we adopted upward and downward arrows to indicate electrons in different spin state on each metal center.

6.1.1 The S_1 state

The S_1 state of complex A was first optimized in the assumption of the highest spin (HS, S_z=7) (↑↑↑↑) configuration in order to elucidate the charge distributions on the Mn ions. The ground electronical configuration corresponds to Mn_1^{3+}, Mn_2^{4+}, Mn_3^{4+}, Mn_4^{3+}, hereafter abbreviated as [3443] configuration. This is in full agreement with the experimentally assignment for complex A. Starting from the HS solution other spin configurations have been obtained. More in details spin solutions corresponding to S_z=0 (↑↑↓↓), 1 (↑↓↓↑), 3 (↓↑↑↑), 4 (↑↑↓↑) have been fully optimized.

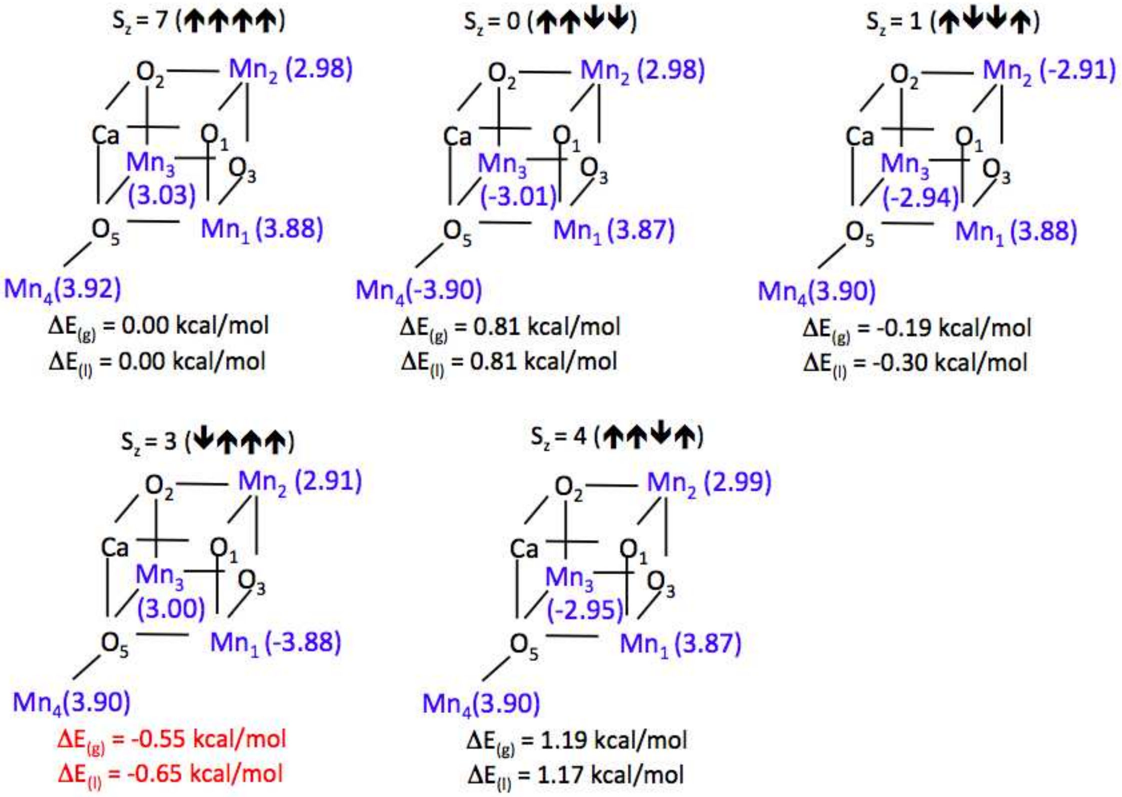

Fig. 6.2: Mulliken spin densities computed in gas phase for Mn ions of the $CaMn_4O_4$ core in the S_1 state. Several spin states have been considered. Energy differences in gas (g) and condensed phase (l) are reffered to the highest spin solution.

Figure 6.2 shows the Mulliken spin density on Mn ions in each spin solution and the stability in both the gas (g) and condesed (l) phase of the various spin configurations relatively to the HS one. These results indicate the spin configuration (↓↑↑↑) with S_z=3 as the lowest in energy although there exist many spin states very close in energy in the S_1 state. The presence of the solvent only slightly affects the various energetic levels.

Table 6.1 summarizes the optimized Mn-Mn, Ca-Mn and Mn-O distances in each spin states for the synthetic complex. For comparison x-rays values of complex A and

Table 6.1: Optimized Mn-Mn, Ca-Mn and Mn-O distances (Å) for the S_1 structure of the $[Mn_4CaO_4]$ core computed in different spin states. For comparison x-rays values of complex A and those recently obtained on the native OEC by XFEL method are also reported.^{a} **??**;^{b} **??**

Distance	S_z=7	S_z=0	S_z=1	S_z=3	S_z=4	XRD^a	natural OEC^b
	↑↑↑↑	↑↑↓↓	↑↓↓↑	↓↑↑↑	↑↑↓↑		
Mn_1-Mn_2	2.80	2.79	2.78	2.78	2.79	2.77	2.68
Mn_1-Mn_3	3.16	3.17	3.16	3.15	3.17	3.09	3.20
Mn_1-Mn_4	3.61	3.61	3.64	3.61	3.64	3.59	4.95
Mn_2-Mn_3	2.74	2.74	2.75	2.75	2.74	2.74	2.70
Mn_2-Mn_4	5.22	5.21	5.23	5.22	5.23	5.24	5.21
Mn_3-Mn_4	3.24	3.23	3.23	3.23	3.23	3.24	2.87
Ca-Mn_1	3.57	3.58	3.58	3.57	3.58	3.46	3.47
Ca-Mn_2	3.40	3.41	3.40	3.40	3.40	3.36	3.32
Ca-Mn_3	3.56	3.55	3.55	3.55	3.56	3.44	3.40
Ca-Mn_1	4.21	4.21	4.24	4.20	4.24	4.06	3.77
Mn_1-O_1	1.83	1.83	1.84	1.84	1.83	1.87	1.80
Mn_1-O_3	2.08	2.07	2.03	2.03	2.07	2.01	1.87
Mn_1-O_5	2.34	2.37	2.39	2.36	2.38	2.28	2.70
Mn_2-O_1	1.79	1.79	1.78	1.78	1.79	1.78	1.82
Mn_2-O_2	1.88	1.89	1.89	1.89	1.89	1.88	1.83
Mn_2-O_3	1.85	1.85	1.84	1.85	1.85	1.86	2.02
Mn_3-O_2	1.82	1.82	1.82	1.82	1.82	1.84	1.90
Mn_3-O_3	1.85	1.85	1.87	1.86	1.85	1.86	2.06
Mn_3-O_5	1.87	1.86	1.83	1.86	1.84	1.86	2.20
Mn_4-O_5	1.82	1.82	1.82	1.82	1.82	1.85	2.33

those recently obtained on the native OEC by XFEL method are also reported. [132] The computed values for the mimic are in good agreement with the experimental ones (the root mean square deviation is about 0.07 Å), underlining the accuracy of the electronic potential employed for the calculation. The optimized distances indicate no significant difference by changing the spin state or including the solvent effects. In table 6.1 bond lengths that are significantly different between complex A and the OEC are marked in red.

It is clear that the principal difference between complex A and the native OEC is the coordination of O_5 atom bridging three Mn and the Ca ion. Indeed in the synthetic model the distances involving the O_5 (see figure 6.1) atom are shorter respect to those of the OEC. The Mn_3-O_5 and Mn_4-O_5 distances change of 0.34 Å and 0.48 Å, respectively.

This effect is very important for Mn_1 ion which in the complex A has a Mn_1-O_5 distance of about 2.3 Å while in the native OEC a value of about 2.7 Å leading to an effectively five coordinated Mn_1, with an open coordination site that may be eventually essential for coordination of a water molecule upon Mn_4 oxidation. Moreover in the synthetic complex the Mn_1-Mn_4 distance is about 1 Å shorter than that in the native OEC. The origin of these structural differences relies in the coordination of Mn_1 and Mn_4 by a single bridging carboxylate whereas in the OEC they are spaced by ligation of two neighboring protein residues.

Table 6.2: Energy difference (kcal/mol) in gas (g) and condensed phase (l) for the same spin states of the [4443] and [3444] electronic configurations.

	S_z=13/2	S_z=1/2	S_z=5/2	S_z=7/2
ΔE (g)	-2.55	-1.45	-1.79	-1.62
ΔE (l)	-0.37	0.56	0.33	0.66

6.1.2 The S_2 state

Starting from the S_1 state, the oxidation of both the Mn_1 and Mn_4 atom has been considered leading respectively to the [4443] and [3444] electronic configurations for the S_2 state. Several spin states have been considered as reported in figure 6.3.

The state with S_z=5/2 is the most stable one for both the [4443] and [3444] electronic configuration.

In table 6.2 the energy difference for the same spin states of the [4443] and [3444] electronical configurations are collected. Very interesting in gas phase the [4443] electromer is more stable compared to the [3444] one in each spin state, while in acetonitrile solution the relative stability is inverted and the Mn_4 oxidation is more favorable.

Moreover when the Mn_1 ion is oxidized ([4443] configuration) a 'closed' structure is reached, characterized by shorten bond between the atoms composing the cubane core (see table 6.3 for bond length and figure 6.4). On the contrary in the [3444] electromer, a more 'open' cubane structure is obtained characterized by longer bonds around the Mn_1 ion (see figure 6.4).

Indeed the optimized Mn_1-O_3, Mn_1-O_5 and Mn_4-O_5 distances of the [4443] elec-

Table 6.3: Optimized Mn-Mn, Ca-Mn and Mn-O distances (Å) for the S_1, S_2 and S_3 structure of the $[Mn_4CaO_4]$ core computed in the most stable spin state spin states.

Distance	S_1 [3443]	S_2 [4443]	S_2 [3444]	S_3 [4444]
Mn_1-Mn_2	2.78	2.75	2.78	2.75
Mn_1-Mn_3	3.15	2.92	3.13	2.94
Mn_1-Mn_4	3.61	3.41	3.62	3.43
Mn_2-Mn_3	2.75	2.75	2.74	2.74
Mn_2-Mn_4	5.22	5.28	5.25	5.26
Mn_3-Mn_4	3.23	3.33	3.25	3.29
Ca-Mn_1	3.57	3.61	3.67	3.72
Ca-Mn_2	3.40	3.43	3.44	3.48
Ca-Mn_3	3.55	3.64	3.73	3.80
Ca-Mn_1	4.20	4.41	4.49	4.56
Mn_1-O_1	1.84	1.82	1.83	1.79
Mn_1-O_3	2.03	1.92	2.03	1.94
Mn_1-O_5	2.36	1.93	2.34	1.99
Mn_2-O_1	1.78	1.80	1.78	1.82
Mn_2-O_2	1.89	1.86	1.92	1.86
Mn_2-O_3	1.85	1.89	1.87	1.91
Mn_3-O_2	1.82	1.82	1.80	1.81
Mn_3-O_3	1.86	1.88	1.82	1.84
Mn_3-O_5	1.86	1.91	1.91	1.94
Mn_4-O_5	1.82	1.94	1.75	1.83

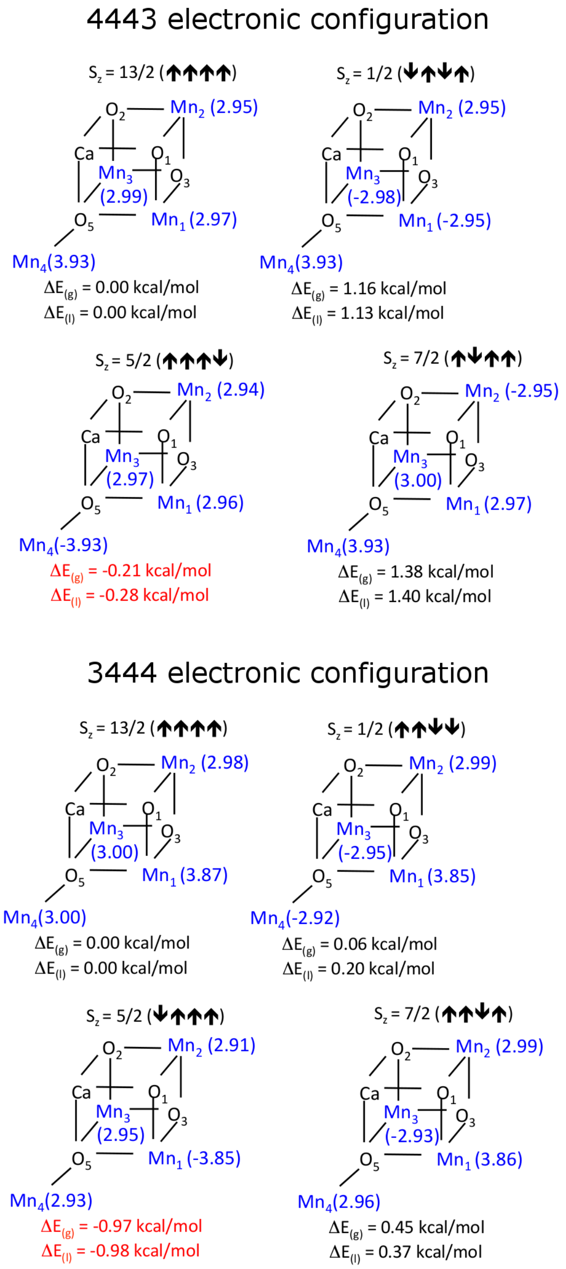

Fig. 6.3: Mulliken spin densities computed in gas phase for Mn ions of the $CaMn_4O_4$ core in the S_2 state. Several spin states have been considered. Energy differences in gas (g) and condensed phase (l) are reffered to the highest spin solution.

tromer ([3444] is shown in parentheses) were 1.92 Å (2.03), 1.93 Å (2.34) and 1.94 Å (1.75) respectively, indicating a shortening of the Mn_1-O_3 and Mn_1-O_5 lengths in the [4443] structure. Table 6.3 shows also the bond lengths for the S_1 state. It is clear that the [3444] electromer, which involves the oxidation of the dangling Mn ion, presents the cubane core structure quite similar to that of the S_1 state. In turn only a slight shortening of the bond lengths is observed in the [3443] ⟶ [3444] oxidation.

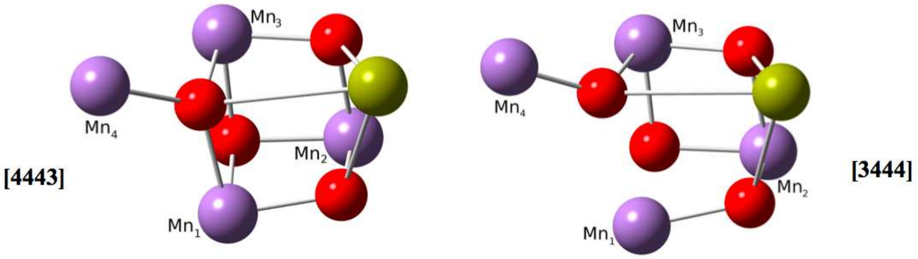

Fig. 6.4: Structure of the 'closed' and 'open' cubane core reached in the [4443] and [3444] electronic configuration, respectively.

6.1.3 The S_3 state

The full geometry optimization of the S_3 state was also perfomed leading to the [4444] electronic configuration, in which all the Mn atom have been oxidized respect to the S_1 state. The most stable spin state is the (↑↑↑↓) characterized by S_z=3 both in gas than in solvent phase (see figure 6.5). Inspection of table 6.3 reveals that the S_3 structure is very similar to the closed cubane of the S_2 [4443] electronic configuration. Indeed upon the eventually one electron oxidation from the [4443] state, no characteristic structural deformations were observed in the S_3 state, except a shortening of the Mn_4-O_5 distance. However in the S_3 state all the bond lengths are shorter respect to the S_1 due to the oxidation of both Mn_1 and Mn_4 ions.

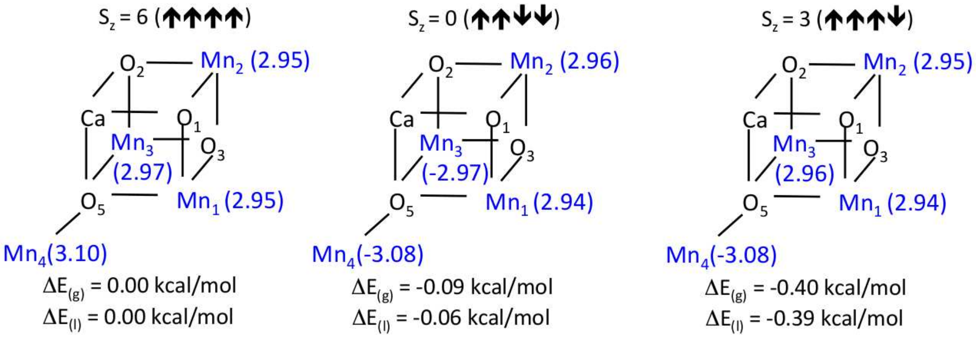

Fig. 6.5: Mulliken spin densities computed in gas phase for Mn ions of the $CaMn_4O_4$ core in the S_3 state. Several spin states have been considered. Energy differences in gas (g) and condensed phase (l) are reffered to the highest spin solution.

6.2 Complex A: exploring the O-O bond formation

As explained before the addiction of trace amount of water leads to obscured oxidation and reduction waves in the cyclic voltammogromam.

Thus to disentangle the performances of complex A in the O-O bond formation some ligands have been selectively exchanged with water molecules in such a way to reproduce the position of the native OEC crystallographic water. Indeed crystallographic data of the natural OEC reveals the presence of four water molecules bound to the $[Mn_4CaO_4]$ core (figure 6.1). Two water molecules are bound to the Ca and the other two to the dangling Mn_4. Hence, starting from the as-synthetized complex A, Bu^tCO_2H acid, $Bu^tCO_2^-$ and pyridine ligands were exchanged with five water molecules to simulate the O-O bond formation (figure 6.6).

More closely the pyridine ligand bound to Mn_4 and $Bu^tCO_2{}^-$ anion bridging Mn_4 and Ca were substituted with three water molecules, of which two directly coordinate the Mn_4 while the last one is bound to the Calcium. The coordination sphere on the Ca atom was completed exchanging the Bu^tCO_2H acid ligand bridging Ca and oxigen atom labeled as O_2 (figure 6.1) with two further water molecules in such a way to preserve the hydrogen bond between the acid and the O_2 center. After each ligand substitution the structure was fully optimized in the S_1 state considering the highest spin solution.

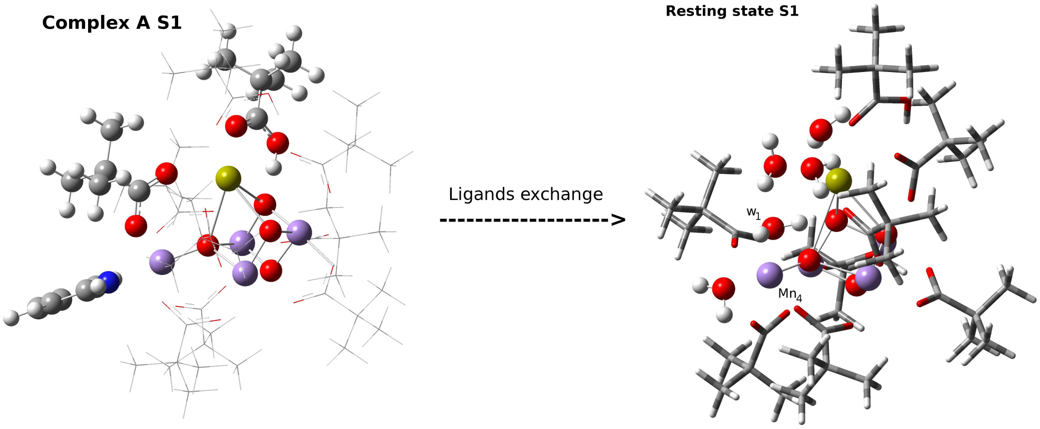

Fig. 6.6: Structure of the complex A before and after the ligands exchange.

Full geometry optimizations were performed at UB3LYP level of theory adopting LANL-2DZ basis set for Mn and Ca, 6-31G(d) for N and O, and 6-31G for C and H. The polarizable continuum model in its conductor like version was adopted to represent the acetonitrile bulk solvation effects.

The S_1 state was considered as resting state (see figure 6.6). S_2 and S_3 states were obtained by the sequentially oxidation of the Mn^{III} ions coupled with the deprotonation of the water directly bound to the Mn_4, namely the water molecule labelled as W_1 in figure 6.6. For the S_1, S_2 and S_3 states only the highest spin solution was considered while several spin states were investigated for the S_4 state. The structures of S_1,S_2,S_3 and S_4 states are represented in the various panels of figure 6.7, while the Mulliken spin densities on each atom are reported in figure 6.8.

The $S_1 \longrightarrow S_2$ transition leads to the preferential oxidation of the Mn_4 ion stabilized by the hydroxo ligand obtained by the first deprotonation of W_1. Moreover the oxidation of Mn_4 is favored of about 3 kcal/mol compared to that of Mn_1 center. The oxidation of Mn_1 and the deprotonation of the hydroxo ligand occur in the $S_2 \longrightarrow S_3$ transition (see figure 6.8).

The S_3 state is thus characterized by all the Mn ions in the IV oxidation state with an oxo ligand bound to Mn_4, which is successively oxidized in the $S_3 \longrightarrow S_4$ transition.

This transition leads to the formation of an oxyl radical directly bound to the Mn_4 ion (see figure 6.7d for the S_4 structure).

Two spin configurations were investigated for the S_4 state as shown in figure 6.9. In the highest spin (HS) solution Mn ions and the oxyl radical are locally at high spin, while the lowest spin (LS) configuration is characterized by an antiferromagnetic coupling among the Mn atoms of the cubane core. The LS solution is more stable

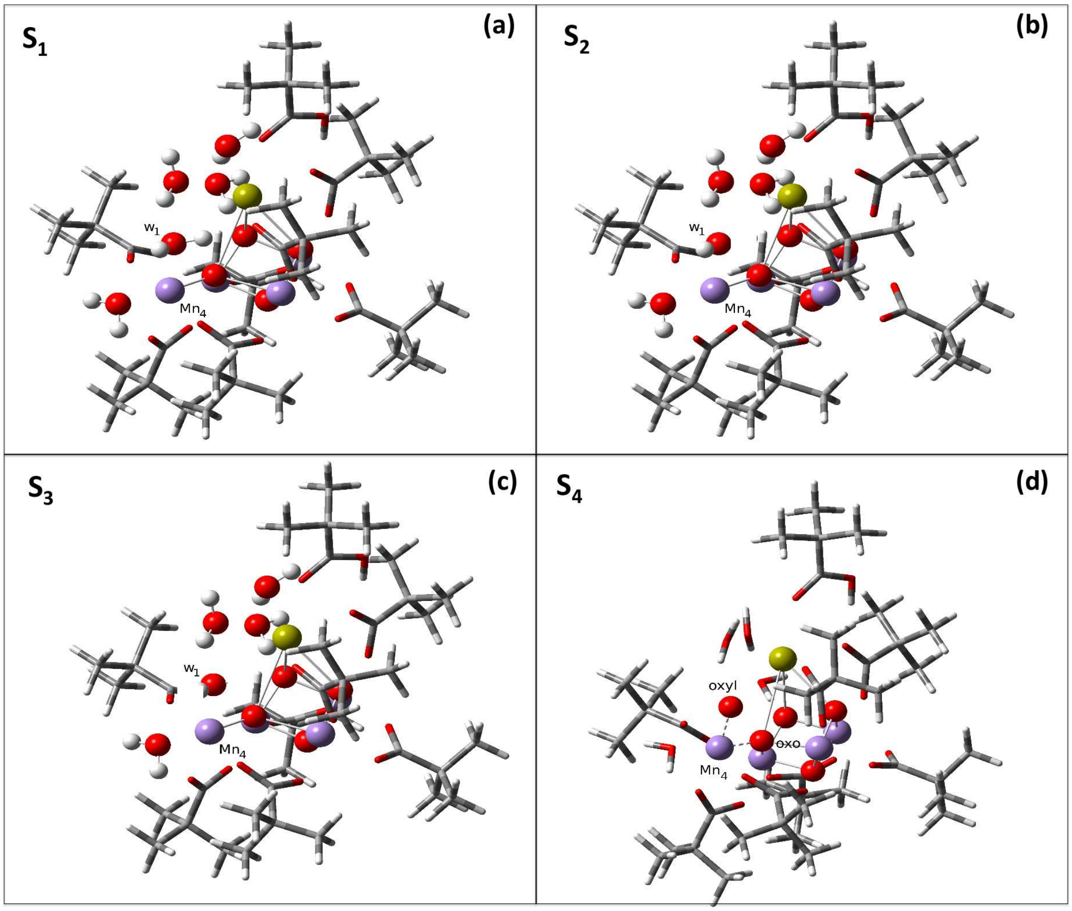

Fig. 6.7: Structure of the complex A in the S_1, S_2, S_3 and S_4 states during the catalytic cycle.

of about 6.70 kcal/mol respect to the HS one.

At this point the oxygen-oxygen bond formation can be investigated. There are two O-O bond formation processes that are frequently discussed in the photocycle of the OEC: water nucleophilic attack and oxyl-oxo coupling processes. The water nucleophilic attack generally occurs between water molecules between Ca and Mn_4 in the OEC. Very important is the presence of electron withdrawing residues near the oxyl oxygen in order to reduce its electron density promoting the attack by the nucleophilic water bound to the Ca atom. This role is achieved by an arginine

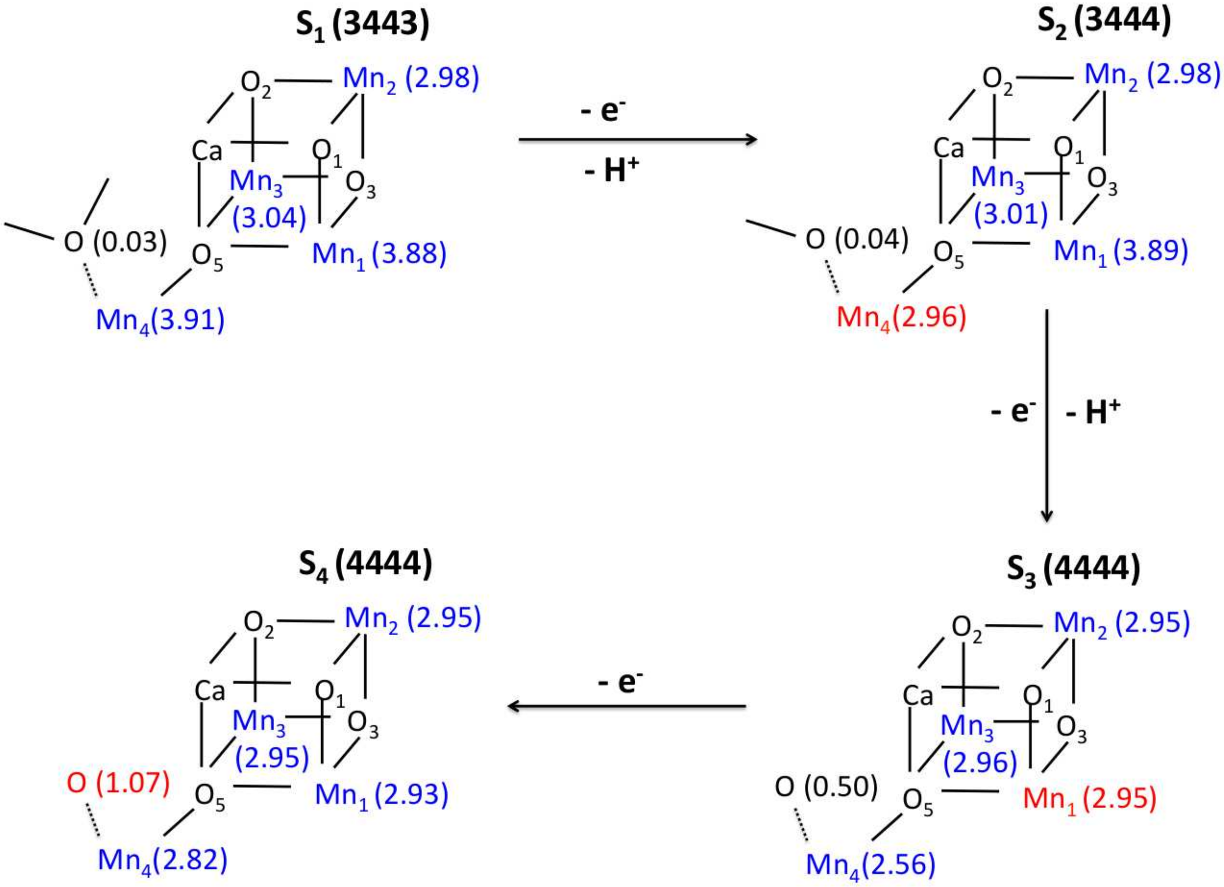

Fig. 6.8: Mulliken spin densities computed in gas phase for Mn ions of the $CaMn_4O_4$ core in the S_1, S_2, S_3 and S_4 states during the catalytic cycle.

residue in the PSII. Instead the oxyl-oxo coupling process in the OEC generally happens between an oxyl-oxygen at the danglin Mn and an oxo-oxygen at the corner of the cubane core. The model structure of complex A does not involve electron withdrawing residue, thus we choose to investigate the oxo-oxyl coupling between the oxyl radical and the O_5 atom of the cubane core.

Transition state have been located for both the HS and LS spin configurations, confirmed also by imaginary frequency at $-858cm^{-1}$ and $-736cm^{-1}$ respectively.

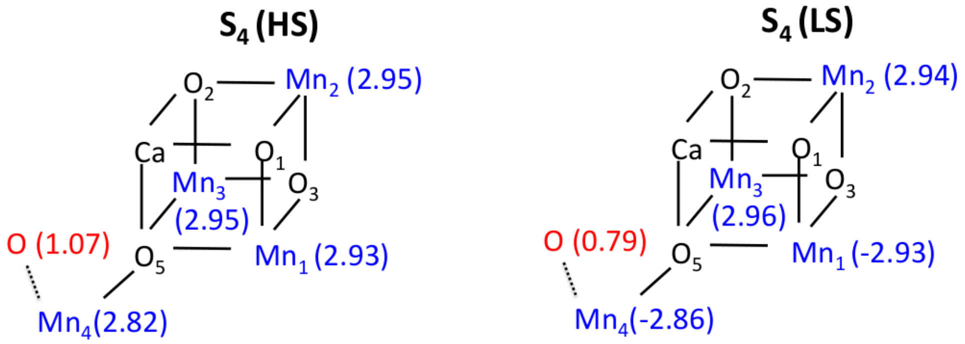

Fig. 6.9: Mulliken spin densities computed in gas phase for Mn ions of the $CaMn_4O_4$ core in the S_4 state.

The computed barrier are 18.79 and 23.40 kcal/mol respectively for the HS and LS solutions.

These values can be compared with those computed by Siegbahn on the native OEC through QM/MM calculations. More closely barrier of about 19 kcal/mol are reported by Siegbahn for the oxyl-oxo coupling process.

The computed barriers for complex A are in very good agreement with that of the native OEC. This is a very important point suggesting crucial insights on the potentiality of complex A as water oxidation catalyst. Moreover it suggests that the key electronical features of the OEC are well reproduced in this synthetic complex encouraging the synthesis of further variants of the complex in which the water ligation can be better controlled. The theoretical support based on well calibrated electronical potential can be the key tool for the future electronical design of these molecular machines.

Final remarks

The development of efficient artificial leaves relies on the subtle combination of the electronic structure of molecular assemblies able to absorbing sunlight, converting light energy into electrochemical potential energy and finally transducing it into chemical accessible energy. As matter of fact the effective combination of photoinduced electron transfer, excited state proton transfer and proton coupled electron transfer reactions by charge transfer molecular machines allow to harvest sunlight and convert it into useful electrochemical energy.

The electronical design of these charge transfer molecular machine is crucial to build up a complex supramolecular architecture for the light energy conversion. Safely the theoretical computational approach represents the third millennium instrument to disentangle complex electronic structure and single out structural and environmental factors affecting these molecular systems.

In the present Ph.D. project, we have amply shown how the combination of methods based on denisty functional theory and its time dependent version, robust solvent models and ab initio molecular dynamics allow to catch the fine interplay of electronic, nuclear and solute solvent interactions crucially governing the charge transfer reactivity. More closely, studying well characterized oligo-peptides in water solution, we showed how solvation effects and dynamic fluctuations in the cybotatic region crucially affect the degree of adiabaticy in proton coupled electron transfer reactions in such a way that the process can occur on the ground state potential energy surface or requiring the coupling with excited state. The role of the solvent have been also investigated in excited state proton transfer process adopting different solvation model to represent th environmental effects. Implicit solvent model, employed to simulated the ESPT between a coumarine and an imidazole molecule in toluene solution, allows to follow the formation of the proton transfer adduct catching the features of the electronic rearrangement which drives the reaction. Nevertheless to achieve the full exploration of the product region during the simulation an explicit solvent representation is mandatory. Hybrid implicit/explicit model of the solvent represents an appealing choice in this sense. This latter was adopted to consider in an explicit way the solvent coordinate in the ESPT from a dipicolinium cyanine dye towards water solvent molecules, revealing that the ESPT is assisted and modulated by low frequency modes of solvent molecules in proximity of the proton acceptor molecule. In general we demonstrated that AIMD based on TD-DFT and robust solvent models appears to be a feasible and reliable way to represent both the electronical, nuclear and solute/solvent rearrangement ruling phototriggered process in condensed phase. Moreover we have underlined the possibility to handle molecules in multiple, and sometimes unusual, charge separated states or metals in different spin states difficult to identify by experiments. We have been able to simulate the whole excited state cascade of an artificial molecular reaction center characterizing intramolecular charge separated states only inderctly postulated from an experimentally point of view. Indeed a complete structural and energetical characterization has been carried out providing significant insights on the formation of a crucial reactive state, fundamental for the application of this molecule in photoelectrochemical cells.

Moreover the driving force of the various charge transfer steps have been successfully catched giving very important insights to support the future design strategies of such molecular assays.

Finally the characterization of the catalytic water splitting cycle of a new proposed water oxidation catalyst, strongly mimic the native oxygen evolving complex of PSII, was taken under study.

A complete structural and electronical characterization of the synthetic complex was performed in different oxidation states considering also variuos spin configurations.

Furthermore we integrated the few experimental insights available about its reactivity, simulating the overall catalytic cycle and showing its great potentiality and efficiency in the oxygen-oxygen bond formation. As matter of fact the computed barriers for the mimic are in very good agreement with that of the native OEC, suggesting its great potentiality as water oxidation catalyst. Moreover it suggests that the key electronical features of the native oxygen evolving complex are well reproduced in the synthetic complex encouraging the synthesis of further variants starting directly from it.

In conclusion, we have illustrated that the theoretical chemistry thanks to new developed tools, offers, nowadays, a strong opportunity to elucidate mechanisms in order to facilitate next-generation design efforts by highlighting those factors that contribute to catalytic activity and efficiency.

Appendix A

The D$_{CT}$ density based index

The formulation of the original CT index (D$_{CT}$), recently developed by Ciofini and co-workers [19] to quantify the spatial extent of a charge-transfer event associated to a vertical excitation, will be here summarized. Having defined $\rho_{GS}(r)$ and $\rho_{EX}(r)$ as the ground and excited state density, respectively, the variation in electronic density associated to an electronic transition is given by:

$$\Delta\rho(r) = \rho_{EX}(r) - \rho_{GS}(r) \tag{A.1}$$

Two functions, $\rho_{+}(r)$ and $\rho_{-}(r)$, can be defined collecting, respectively, the points in the space where an increment or a decrease of the electronic density upon transition is produced and corresponding to positive and negative values of $\Delta\rho(r)$, respectively:

$$\rho_{+}(r) = \begin{cases} \Delta\rho(r) & if \Delta\rho(r) > 0 \\ 0 & if \Delta\rho(r) < 0 \end{cases} \tag{A.2}$$

$$\rho_{-}(r) = \begin{cases} \Delta\rho(r) & if \Delta\rho(r) < 0 \\ 0 & if \Delta\rho(r) > 0 \end{cases} \tag{A.3}$$

Defining R_+ and R_- the barycenters of the spatial regions associated to $\rho_+(r)$ and $\rho_-(r)$, respectively, the D$_{CT}$ can be simply defined as the distance between R_+ and R_- :

$$D_{CT} = |R_+ - R_-| \tag{A.4}$$

This index has been used to quantify the spatial extent of CT excitation in different families of push-pull dyes [19, 83–85] as well as diagnostic index for erratic behavior of standard DFT approaches in the description of through space CT excitations. [19]

Bibliography

[1] M. Grätzel, Accounts of chemical research **42** (11), 1788 (2009).

[2] S. Berardi, S. Drouet, L. Francàs, C. Gimbert-Suriñach, M. Guttentag, C. Richmond, T. Stoll, and A. Llobet, Chemical Society Reviews **43** (22), 7501 (2014).

[3] D. Gust, T. A. Moore, and A. L. Moore, Faraday discussions **155**, 9 (2012).

[4] M. J. Llansola-Portoles, R. E. Palacios, D. Gust, T. A. Moore, and A. L. Moore, in *From Molecules to Materials* (Springer, 2015), pp. 71–98.

[5] E. Amouyal, Solar Energy Materials and Solar Cells **38** (1), 249 (1995).

[6] R. L. House, N. Y. M. Iha, R. L. Coppo, L. Alibabaei, B. D. Sherman, P. Kang, M. K. Brennaman, P. G. Hoertz, and T. J. Meyer, Journal of Photochemistry and Photobiology C: Photochemistry Reviews (2015).

[7] N. Cox, D. A. Pantazis, F. Neese, and W. Lubitz, Interface focus **5** (3), 20150009 (2015).

[8] A. Fujishima and K. Honda, Nature **238** (5385), 37 (1972).

[9] J. Barber, Quat. Rev. Biophys **36**, 71 (2003).

[10] R. G. Parr and W. Yang, *Density-functional theory of atoms and molecules*, vol. 16 (Oxford university press, 1989).

[11] R. E. Stratmann, G. E. Scuseria, and M. J. Frisch, The Journal of chemical physics **109** (19), 8218 (1998).

[12] E. Runge and E. K. U. Gross, Physical Review Letters **52** (12), 997 (1984).

[13] D. J. Tozer, R. D. Amos, N. C. Handy, B. O. Roos, and L. Serrano-Andres, Molecular physics **97** (7), 859 (1999).

[14] A. Dreuw and M. Head-Gordon, Journal of the American Chemical Society **126** (12), 4007 (2004).

[15] D. L. Thompson, *Modern methods for multidimensional dynamics computations in chemistry* (World Scientific, 1998).

[16] T. Helgaker, E. Uggerud, and H. J. A. Jensen, Chemical Physics Letters **173** (2), 145 (1990).

[17] J. M. Millam, W. Chen, W. L. Hase, H. B. Schlegel *et al.*, The Journal of chemical physics **111** (9), 3800 (1999).

[18] M. Savarese, U. Raucci, C. Adamo, P. A. Netti, I. Ciofini, and N. Rega, Physical Chemistry Chemical Physics **16** (38), 20681 (2014).

[19] T. Le Bahers, C. Adamo, and I. Ciofini, J. Chem. Theory Comput. **7** (8), 2498 (2011).

[20] U. Raucci, M. Savarese, C. Adamo, I. Ciofini, and N. Rega, The Journal of Physical Chemistry B **119** (6), 2650 (2015).

[21] B. Giese, M. Wang, J. Gao, M. Stoltz, P. Muller, and M. Graber, The Journal of organic chemistry **74** (10), 3621 (2009).

[22] M. Cordes, A. Köttgen, C. Jasper, O. Jacques, H. Boudebous, and B. Giese, Angewandte Chemie International Edition **47** (18), 3461 (2008).

[23] J. D. Megiatto, A. Antoniuk-Pablant, B. D. Sherman, G. Kodis, M. Gervaldo, T. A. Moore, A. L. Moore, and D. Gust, Proceedings of the National Academy of Sciences **109** (39), 15578 (2012).

[24] C. Zhang, C. Chen, H. Dong, J.-R. Shen, H. Dau, and J. Zhao, Science **348** (6235), 690 (2015).

[25] R. G. Pearson, *Symmetry rules for chemical reactions: orbital topology and elementary processes* (Wiley New York, 1976).

[26] D. Jacquemin, E. A. Perpete, G. E. Scuseria, I. Ciofini, and C. Adamo, Journal of chemical theory and computation **4** (1), 123 (2008).

[27] P. Leiderman, L. Genosar, and D. Huppert, J. Phys. Chem. A **109** (27), 5965 (2005).

[28] R. Simkovitch, S. Shomer, R. Gepshtein, and D. Huppert, The Journal of Physical Chemistry B **119** (6), 2253 (2014).

[29] J. L. Pérez-Lustres, F. Rodriguez-Prieto, M. Mosquera, T. A. Senyushkina, N. P. Ernsting, and S. A. Kovalenko, J. Am. Chem. Soc. **129**, 5408 (2007).

[30] K. Fukui, Accounts of chemical research **14** (12), 363 (1981).

[31] C. Gonzalez and H. B. Schlegel, The Journal of Chemical Physics **90** (4), 2154 (1989).

[32] H. BernhardáSchlegel, Journal of the Chemical Society, Faraday Transactions **90** (12), 1569 (1994).

[33] H. P. Hratchian, M. J. Frisch, and H. B. Schlegel, The Journal of chemical physics **133** (22), 224101 (2010).

[34] H. P. Hratchian and H. B. Schlegel, Theory and applications of computational chemistry: the first forty years **4**, 195 (2005).

[35] F. Furche and R. Ahlrichs, The Journal of chemical physics **117** (16), 7433 (2002).

[36] G. Scalmani, M. J. Frisch, B. Mennucci, J. Tomasi, R. Cammi, and V. Barone, The Journal of chemical physics **124** (9), 094107 (2006).

[37] I. Tavernelli*, U. F. Röhrig, and U. Rothlisberger, Molecular Physics **103** (6-8), 963 (2005).

[38] M. Guglielmi, I. Tavernelli, and U. Rothlisberger, Physical Chemistry Chemical Physics **11** (22), 4549 (2009).

[39] A. D. Becke, The Journal of chemical physics **98** (7), 5648 (1993).

[40] S. Nachimuthu, J. Gao, and D. G. Truhlar, Chemical physics **400**, 8 (2012).

[41] S. Sadhukhan, D. Muñoz, C. Adamo, and G. Scuseria, Chemical physics letters **306** (1), 83 (1999).

[42] G. F. Mangiatordi, E. Bremond, and C. Adamo, Journal of chemical theory and computation **8** (9), 3082 (2012).

[43] L. B. Harding, S. J. Klippenstein, and A. W. Jasper, Physical Chemistry Chemical Physics **9** (31), 4055 (2007).

[44] R. Cukier and D. Nocera, Annual review of physical chemistry **49** (1), 337 (1998).

[45] S. Hammes-Schiffer, ChemPhysChem **3** (1), 33 (2002).

[46] S. Hammes-Schiffer, Accounts of chemical research **34** (4), 273 (2001).

[47] J. M. Mayer and I. J. Rhile, Biochimica et Biophysica Acta (BBA)-Bioenergetics **1655**, 51 (2004).

[48] J. B. Issa, K. Krogh-Jespersen, and S. S. Isied, The Journal of Physical Chemistry C **114** (48), 20809 (2010).

[49] S. Hammes-Schiffer, Energy & Environmental Science **5** (7), 7696 (2012).

[50] S. Hammes-Schiffer and A. A. Stuchebrukhov, Chemical reviews **110** (12), 6939 (2010).

[51] S. Hammes-Schiffer, Journal of the American Chemical Society **137** (28), 8860 (2015).

[52] S. Chakrabarti, M. F. Parker, C. W. Morgan, C. E. Schafmeister, and D. H. Waldeck, Journal of the American Chemical Society **131** (6), 2044 (2009).

[53] J. Barber, Biochemistry (Moscow) **79** (3), 185 (2014).

[54] Y. Umena, K. Kawakami, J.-R. Shen, and N. Kamiya, Nature **473** (7345), 55 (2011).

[55] N. Yapici, S. Jockusch, A. Moscatelli, S. Mandalapu, Y. Itagaki, D. Bates, S. Wiseman, K. Gibson, N. Turro, and L. Bi, Org. Lett. **14** (1), 50 (2012).

[56] M. Kumar, N. Kumar, V. Bhalla, P. Sharma, and T. Kaur, Org. Lett. **14** (1), 406 (2012).

[57] Z. Yang, M. She, B. Yin, J. Cui, Y. Zhang, W. Sun, J. Li, and Z. Shi, J. Org. Chem. **77** (2), 1143 (2012).

[58] Y. Koide, Y. Urano, K. Hanaoka, W. Piao, M. Kusakabe, N. Saito, T. Terai, T. Okabe, and T. Nagano, J. Am. Chem. Soc. **134** (11), 5029 (2012).

[59] M. Beija, C. Afonso, and J. Martinho, Chem. Soc. Rev. **38**, 2410 (2009).

[60] Y. Koide, Y. Urano, K. Hanaoka, T. Terai, and T. Nagano, ACS Chem. Biol. **6**, 600 (2011).

[61] D. R. Larson, H. Ow, H. D. Vishwasrao, A. A. Heikal, U. Wiesner, and W. W. Webb, Chem. Mat. **20**, 2677 (2008).

[62] K. Chingin, R. M. Balabin, V. Frankevich, H. Chen, K. Barylyuk, R. Nieckarz, A. Fedorov, and R. Zenobi, Phys. Chem. Chem. Phys. **12**, 14121 (2010).

[63] K. Chingin, R. M. Balabin, K. Barylyuk, H. Chen, V. Frankevich, and R. Zenobi, Phys. Chem. Chem. Phys. **12**, 11710 (2010).

[64] E. Kato and T. Murakami, Polymer Gels and Networks **6** (3-4), 179 (1998).

[65] F. L. Arbeloa and K. K. Rohatgi-Mukherjee, Chem. Phys. Lett. **129**, 607 (1986).

[66] F. L. Arbeloa and I. U. Aguirresacona, Chem. Phys. **130**, 371 (1989).

[67] A. Penzkofer and M. Falkenstein, Opt. Quant. Electron **10**, 399 (1978).

[68] M. Snare, F. Treloar, K. Ghiggino, and P. Thistlethwaite, J. Photochem. **18** (4), 335 (1982).

[69] T. Karstens and K. Kobs, J. Phys. Chem. **84**, 1871 (1980).

[70] K. H. Drexhage, Top. Appl. Phys. **1**, 144 (1973).

[71] K. Drexhage, J. Res. Natl. Bur. Stand **80**, 421 (1976).

[72] K. Drexhage, Dye lasers pp. 155–200 (1973).

[73] M. W. Vogel, W. Rettig, R. Sens, and K. H. Drexhage, Chem. Phys. Lett. **147**, 452 (1988).

[74] Z. Grabowski, K. Rotkiewicz, A. Siemiarczuk, D. J. Cowley, and W. Baumann, Nouv. J. Chim. **3**, 443 (1979).

[75] Z. R. Grabowski, K. Rotkiewicz, and W. Rettig, Chem. Rev. **103**, 3899 (2003).

[76] K. A. Zachariasse, T. von der Haar, A. Hebecker, U. Leinhos, and W. KUhnle, Pure Appl. Chem. **65**, 1745 (1993).

[77] T. von der Haar, A. Hebecker, Y. Il'ichev, Y. B. Jiang, W. Ktihnle, and K. A. Zachariasse, Recl. Trav. Chim. Pays-Bas **114**, 430 (1995).

[78] Y. Koide, Y. Urano, K. Hanaoka, T. Terai, and T. Nagano, J. Am. Chem. Soc. **133** (15), 5680 (2011).

[79] X.-F. Zhang, Y. Zhang, and L. Liu, J. Lumin. **145**, 448 (2014).

[80] L.-l. Jiang, W.-l. Liu, Y.-f. Song, X. He, Y. Wang, C. Wang, H.-l. Wu, F. Yang, and Y.-q. Yang, Chemical Physics **429**, 12 (2014).

[81] A. Pedone, G. Prampolini, S. Monti, and V. Barone, Chemistry of Materials **23**, 5016 (2011).

[82] V. Barone, J. Bloino, S. Monti, A. Pedone, and G. Prampolini, Phys. Chem. Chem. Phys. **13**, 2160 (2011).

[83] I. Ciofini, T. Le Bahers, C. Adamo, F. Odobel, and D. Jacquemin, J. Phys. Chem. C **116** (22), 11946 (2012).

[84] D. Jacquemin, T. Le Bahers, C. Adamo, and I. Ciofini, Phys. Chem. Chem. Phys. **14** (16), 5383 (2012).

[85] F. Labat, I. Ciofini, and C. Adamo, J. Mater. Chem. **22** (24), 12205 (2012).

[86] G. García, C. Adamo, and I. Ciofini, Phys. Chem. Chem. Phys. **15** (46), 20210 (2013).

[87] M. Savarese, P. A. Netti, C. Adamo, N. Rega, and I. Ciofini, J. Phys. Chem. B **117** (50), 16165 (2013).

[88] G. Vàmosi, C. Gohlke, and R. M. Clegg, Biophys. J. **71**, 972 (1996).

[89] M. Savarese, A. Aliberti, I. De Santo, E. Battista, F. Causa, P. A. Netti, and N. Rega, J. Phys. Chem. A **116** (28), 7491 (2012).

[90] R. Kubin and A. Fletcher, J. Lumin. **27** (4), 455 (1983).

[91] R. Long, N. J. English, and O. V. Prezhdo, J. Am. Chem. Soc. **135** (50), 18892 (2013).

[92] G. Brancato, N. Rega, and V. Barone, The Journal of chemical physics **128**, 144501 (2008).

[93] G. Brancato, N. Rega, and V. Barone, The Journal of chemical physics **125**, 164515 (2006).

[94] G. Brancato, V. Barone, and N. Rega, Theoretical Chemistry Accounts: Theory, Computation, and Modeling (Theoretica Chimica Acta) **117** (5), 1001 (2007).

[95] B. C. Westlake, J. J. Paul, S. E. Bettis, S. D. Hampton, B. P. Mehl, T. J. Meyer, and J. M. Papanikolas, The Journal of Physical Chemistry B **116** (51), 14886 (2012).

[96] B. C. Westlake, M. K. Brennaman, J. J. Concepcion, J. J. Paul, S. E. Bettis, S. D. Hampton, S. A. Miller, N. V. Lebedeva, M. D. Forbes, A. M. Moran *et al.*, Proceedings of the National Academy of Sciences **108** (21), 8554 (2011).

[97] M. Savarese, P. A. Netti, N. Rega, C. Adamo, and I. Ciofini, Physical Chemistry Chemical Physics **16** (18), 8661 (2014).

[98] M. Cossi, N. Rega, G. Scalmani, and V. Barone, J. Comp. Chem. **24**, 669 (2003).

[99] V. Barone and M. Cossi, The Journal of Physical Chemistry A **102** (11), 1995 (1998).

[100] H. Schlegel, J. Millam, S. Iyengar, G. Voth, A. Daniels, G. Scuseria, and M. Frisch, The Journal of Chemical Physics **114**, 9758 (2001).

[101] S. Iyengar, H. Schlegel, J. Millam, G. Voth, G. Scuseria, and M. Frisch, The Journal of Chemical Physics **115**, 10291 (2001).

[102] H. Schlegel, S. Iyengar, X. Li, J. Millam, G. Voth, G. Scuseria, and M. Frisch, The Journal of chemical physics **117**, 8694 (2002).

[103] S. Iyengar, H. Schlegel, G. Voth, J. Millam, G. Scuseria, and M. Frisch, Israel journal of chemistry **42** (2-3), 191 (2002).

[104] R. Simkovitch, N. Karton-Lifshin, S. Shomer, D. Shabat, and D. Huppert, The Journal of Physical Chemistry A **117** (16), 3405 (2013).

[105] M. Cossi, N. Rega, G. Scalmani, and V. Barone, J. Comput. Chem. **24** (6), 669 (2003).

[106] T. Vreven, K. S. Byun, I. Komáromi, S. Dapprich, J. A. Montgomery, K. Morokuma, and M. J. Frisch, Journal of Chemical Theory and Computation **2** (3), 815 (2006).

[107] W. Jorgensen, J. Chandrasekhar, J. Madura, R. Impey, and M. Klein, The Journal of chemical physics **79**, 926 (1983).

[108] X. Chen, G. Ma, W. Sun, H. Dai, D. Xiao, Y. Zhang, X. Qin, Y. Liu, and Y. Bu, Journal of the American Chemical Society **136** (12), 4515 (2014).

[109] J. Lin, I. A. Balabin, and D. N. Beratan, Science **310** (5752), 1311 (2005).

[110] A. De la Lande, N. S. Babcock, J. Řezáč, B. C. Sanders, and D. R. Salahub, Proceedings of the National Academy of Sciences **107** (26), 11799 (2010).

[111] A. Migliore, S. Corni, R. Di Felice, and E. Molinari, The Journal of Physical Chemistry B **110** (47), 23796 (2006).

[112] M. Cordes, O. Jacques, A. Köttgen, C. Jasper, H. Boudebous, and B. Giese, Advanced Synthesis & Catalysis **350** (7-8), 1053 (2008).

[113] J. Gao, P. Müller, M. Wang, S. Eckhardt, M. Lauz, K. M. Fromm, and B. Giese, Angewandte Chemie International Edition **50** (8), 1926 (2011).

[114] N. Rega, S. S. Iyengar, G. A. Voth, H. B. Schlegel, T. Vreven, and M. J. Frisch, The Journal of Physical Chemistry B **108** (13), 4210 (2004).

[115] H. Zhong and H. A. Carlson, Journal of Chemical Theory and Computation **2** (2), 342 (2006).

[116] U. Raucci, M. Savarese, A. Petrone, and R. Nadia, Manuscript in preparation .

[117] C. Adamo and V. Barone, The Journal of chemical physics **110** (13), 6158 (1999).

[118] G. F. Moore, M. Hambourger, G. Kodis, W. Michl, D. Gust, T. A. Moore, and A. L. Moore, The Journal of Physical Chemistry B **114** (45), 14450 (2010).

[119] T. Yanai, D. P. Tew, and N. C. Handy, Chemical Physics Letters **393** (1), 51 (2004).

[120] Z.-L. Cai, M. J. Crossley, J. R. Reimers, R. Kobayashi, and R. D. Amos, The Journal of Physical Chemistry B **110** (31), 15624 (2006).

[121] J. Finley, P.-Å. Malmqvist, B. O. Roos, and L. Serrano-Andrés, Chemical physics letters **288** (2), 299 (1998).

[122] H. Nakatsuji, Chemical Physics Letters **67** (2), 329 (1979).

[123] N. Mataga, Y. Shibata, H. Chosrowjan, N. Yoshida, and A. Osuka, The Journal of Physical Chemistry B **104** (17), 4001 (2000).

[124] L. Noodleman and J. G. Norman Jr, The Journal of Chemical Physics **70** (11), 4903 (1979).

[125] L. Noodleman, The Journal of Chemical Physics **74** (10), 5737 (1981).

[126] J. G. Norman Jr, P. B. Ryan, and L. Noodleman, Journal of the American Chemical Society **102** (12), 4279 (1980).

[127] A. A. Ovchinnikov and J. K. Labanowski, Physical Review A **53** (6), 3946 (1996).

[128] M. Yagi and M. Kaneko, Chemical Reviews **101** (1), 21 (2001).

[129] J. D. Blakemore, R. H. Crabtree, and G. W. Brudvig, Chemical Reviews **115** (23), 12974 (2015).

[130] S. W. Gersten, G. J. Samuels, and T. J. Meyer, Journal of the American Chemical Society **104** (14), 4029 (1982).

[131] C. S. Mullins and V. L. Pecoraro, Coordination chemistry reviews **252** (3), 416 (2008).

[132] M. Suga, F. Akita, K. Hirata, G. Ueno, H. Murakami, Y. Nakajima, T. Shimizu, K. Yamashita, M. Yamamoto, H. Ago *et al.*, Nature **517** (7532), 99 (2015).